Loss of STIM2 in colorectal cancer drives growth and metastasis through metabolic reprogramming and PERK-ATF4 endoplasmic reticulum stress pathway

Trayambak Pathak[1, 2], J. Cory Benson[1, 2, 3], Martin T. Johnson[4], Ping Xin[1, 2], Ahmed Emam Abdelnaby[1, 2], Vonn Walter[5, 6], Walter A. Koltun[8], Gregory S. Yochum[7, 8], Nadine Hempel[3], Mohamed Trebak[1,2,3,9]

[1]Department of Pharmacology and Chemical Biology, [2]Vascular Medicine Institute, and [3]UPMC Hillman Cancer Center. University of Pittsburgh School of Medicine, Pittsburgh, Pennsylvania, United States

[4]Department of Medicine, Emory University School of Medicine, Atlanta, Georgia, United States

[5]Department of Public Health Sciences, The Pennsylvania State University College of Medicine, Hershey, Pennsylvania, United States

[6]Penn State Cancer Institute. The Pennsylvania State University College of Medicine, Hershey, United States

[7]Department of Biochemistry and Molecular Biology, The Pennsylvania State University College of Medicine, Hershey, United States

[8]Department of Surgery, Division of Colon and Rectal Surgery, The Pennsylvania State University College of Medicine, Hershey, United States

[9]To whom correspondence should be addressed at trebakm@pitt.edu

Highlights

- STIM2 regulates ER Ca^{2+} homeostasis independently of Orai and SOCE.
- STIM2 downregulation in colorectal cancer cells causes enhanced ER Ca^{2+} and is associated with poor patient prognosis.
- STIM2 downregulation induces PERK/ATF4 dependent ER stress in colorectal cancer.
- Increased ER stress drives colorectal cancer metabolic reprogramming, growth, and metastasis.

Key Words

STIM2, colorectal cancer, ER stress, ER Ca^{2+}, SERCA2, PERK, ATF4, cMyc**,** mitochondria, metabolism

Abstract

The endoplasmic reticulum (ER) stores large amounts of calcium (Ca^{2+}), and the controlled release of ER Ca^{2+} regulates a myriad of cellular functions. Although altered ER Ca^{2+} homeostasis is known to induce ER stress, the mechanisms by which ER Ca^{2+} imbalance activate ER stress pathways are poorly understood. Stromal-interacting molecules STIM1 and STIM2 are two structurally homologous ER-resident Ca^{2+} sensors that synergistically regulate Ca^{2+} influx into the cytosol through Orai Ca^{2+} channels for subsequent signaling to transcription and ER Ca^{2+} refilling. Here, we demonstrate that reduced STIM2, but not STIM1, in colorectal cancer (CRC) is associated with poor patient prognosis. Loss of STIM2 causes SERCA2-dependent increase in ER Ca^{2+}, increased protein translation and transcriptional and metabolic rewiring supporting increased tumor size, invasion, and metastasis. Mechanistically, STIM2 loss activates cMyc and the PERK/ATF4 branch of ER stress in an Orai-independent manner. Therefore, STIM2 and PERK/ATF4 could be exploited for prognosis or in targeted therapies to inhibit CRC tumor growth and metastasis.

Introduction

Colorectal cancer (CRC) is one of the leading causes of death in the United States, with an estimated 53,000 deaths per year (Siegel *et al*, 2020). A recent report showed an alarming annual increase in CRC incidence by 2.2 % in individuals younger than 50 years (Siegel *et al*, 2023). Despite recent advancements in detection and treatment, patients diagnosed with metastatic CRC have poor prognoses. Recent studies identified five CRC intrinsic subtypes (CRIS) based on their molecular and transcriptional signatures (Dunne *et al*, 2017; Guinney *et al*, 2015; Isella *et al*, 2017). Transcriptional reprogramming is required for cancer cells to overcome and adapt to environmental and physiological stressors and to evade death and undergo clonal selection and metastasis (Blancafort *et al*, 2005; Teng *et al*, 2020).

In healthy cells, altered function of the endoplasmic reticulum (ER) through exposure to stressors generally leads to increased accumulation of misfolded or unfolded proteins (Hetz, 2012). The increased unfolded protein burden in the ER triggers an adaptive response termed the unfolded protein response (UPR), which includes several homeostatic signaling pathways aimed at reducing unfolded proteins, recovering proper ER function, and sustaining cell survival. When cells fail to adapt during conditions of chronic ER stress, apoptotic cell death is triggered (Hetz, 2012). In cancer cells however, chronic UPR supports cancer cell adaptation and survival in response to various stress responses, including proteostasis defects, nutrient deprivation, and hypoxia. Once activated, the UPR promotes the generation of multiple transcription factors to support the transcriptional reprogramming of cancer cells (Corazzari *et al*, 2017; Costa-Mattioli & Walter, 2020; Hart *et al*, 2012; Tameire *et al*, 2019). There are three known branches of the UPR with unique signal transduction mechanisms that function in parallel to one another. Each branch is divided based on the presence of a specific endoplasmic reticulum (ER)-resident transmembrane protein: i) IRE1α (inositol requiring enzyme 1α), ii) PERK (double-stranded RNA-activated protein kinase (PKR)–like ER kinase), and iii) ATF6 (activating transcription factor 6) (Hetz, 2012; Walter & Ron, 2011). These three ER proteins bind the ER chaperone BiP from the ER luminal side, keeping them inactive under physiological conditions. Altered ER Ca^{2+} homeostasis has a direct effect on the ATP-ase cycle of the ER chaperone BiP and on BiP-substrate interactions, subsequently triggering the proteostatic effects of UPR (Preissler *et al*, 2020). Furthermore, activation of oncogenes such as cMyc also triggers bioenergetic processes such as protein synthesis and metabolic rewiring to support cancer cell growth and proliferation (Destefanis *et al*, 2020; Hart *et al.*, 2012; Li *et al*, 2005; Morrish & Hockenbery, 2014; Pakos-Zebrucka *et al*, 2016; Satoh *et al*, 2017). Multiple studies showed that cMyc-induced transcriptional reprogramming activates the PERK/eIF2α/ATF4 branch of the UPR (Hart *et al.*, 2012; Tameire *et al.*, 2019).

Cytosolic, ER and mitochondrial Ca^{2+} are interconnected and are fueled and regulated through Ca^{2+} influx across the plasma membrane (PM) (Ben-Kasus Nissim *et al*, 2017; Emrich *et al*, 2021; Pathak *et al*, 2020; Pathak & Trebak, 2018; Trebak & Putney, 2017). In non-excitable cells, the major route of regulated Ca^{2+} influx into cells is the store-operated calcium entry (SOCE) mediated by PM-resident Orai channels (Emrich *et al*, 2022; Prakriya & Lewis, 2015; Trebak & Kinet, 2019; Trebak & Putney, 2017; Yoast *et al*, 2020a). SOCE is regulated by ER-resident Ca^{2+} sensing stromal-interacting molecules (STIM1 and STIM2), which are encoded by two distinct genes.

Stimulation of G protein-coupled receptors (GPCR) or receptor tyrosine kinase (RTK) that couple to isoforms of phospholipase C (PLC) leads to production of inositol-1,4,5-trsiphosphate (IP_3). IP_3 binds to IP_3 receptor channels in the surface of the ER to cause Ca^{2+} release from the ER and subsequent ER Ca^{2+} store depletion. Upon ER Ca^{2+} depletion, STIM proteins aggregate and move into ER-PM junctions where they physically trap and activate Orai Ca^{2+} channels to trigger Ca^{2+} influx into the cytosol (Emrich *et al.*, 2021; Yoast *et al*, 2020c). The N-terminal Ca^{2+}-binding EF-hands of STIM1 and STIM2 have different affinities for Ca^{2+}; STIM2 Kd for Ca^{2+} is ~400 μM while STIM1 Kd for Ca^{2+} is ~200 μM. As such, STIM2 activation is triggered by subtle depletion of ER Ca^{2+} stores while STIM1 requires substantial store depletion to be activated (Brandman *et al*, 2007b; Trebak & Kinet, 2019). Further, the C-terminal domains of STIM1 and STIM2 that interact with Orai are also distinct with STIM1 being a strong activator of SOCE while STIM2 is a weak activator (Emrich *et al*, 2019). While both STIM1 and STIM2 are concomitantly involved in SOCE across the range of agonist concentrations (Emrich *et al.*, 2021), STIM2 function is mostly prominent under resting conditions and under moderate levels of receptor stimulation while STIM1 is the primary driver of receptor-activated SOCE during robust receptor activation (Brandman *et al.*, 2007b; Emrich *et al.*, 2021; Liou *et al*, 2005; Roos *et al*, 2005; Wedel *et al*, 2007). In summary, STIM2 and STIM1 are *bona fide* ER Ca^{2+} sensors and activators of SOCE, but they differ in their strength of activation of SOCE and operate at different ranges of ER Ca^{2+} store depletion and agonist concentrations.

Through the course of eukaryotic evolution, STIM appeared long after Orai, suggesting that STIM proteins likely functioned independently of Orai channels and only later did they co-opt an existing Orai for regulating SOCE (Collins & Meyer, 2011). Indeed, in addition to the established synergistic function of STIM1 and STIM2 proteins in regulating SOCE, several studies have reported on additional functions of STIM1 that are independent of SOCE. STIM1 was shown to regulate endothelial permeability by coupling to RhoA activation in a SOCE- and Orai1-independent manner(Shinde *et al*, 2013). In cardiomyocytes, STIM1 binds to phospholamban in the ER to indirectly activate SERCA2 and enhance sarcoplasmic reticulum (SR) Ca^{2+} levels (Zhao *et al*, 2015). STIM1 also supports the SR-PM functional coupling in contractile smooth muscle of Ca^{2+} release channels in the SR and ion channels on the PM (Krishnan *et al*, 2022). Furthermore, STIM1 was reported to regulate adenylyl cyclases (Motiani *et al*, 2018) and a number of PM ion channels and transporters, including transient receptor potential canonical (TRPC) channels, arachidonate-regulated Ca^{2+} (ARC) channels and PM Ca^{2+} ATPase (PMCA) (Gonzalez-Cobos *et al*, 2013; Ritchie *et al*, 2012; Shuttleworth *et al*, 2007; Worley *et al*, 2007; Zhang *et al*, 2013). However, SOCE-independent functions of STIM2 remain elusive, and the molecular mechanisms of STIM2-mediated activation of ER specific signaling pathways in either normal or cancer cells is unknown.

Here, we discovered that the loss of STIM2 expression is associated with poor colorectal cancer patient survival. we show a novel SOCE- and Orai-independent function of STIM2 in regulating ER Ca^{2+} homeostasis and UPR-dependent ER stress response in colorectal cancer. We demonstrate that loss of STIM2 in CRC alters ER Ca^{2+} levels and activates cMyc and the PERK/ATF4 branch of ER stress pathway to cause transcriptional reprogramming and metabolic rewiring of colorectal cancer cells. These changes in transcription and metabolism support the growth and metastasis of

CRC cells in animal xenograft models. Therefore, we have discovered a previously unknown SOCE-independent function of STIM2 as a molecular switch regulating ER stress to control CRC survival and progression suggesting that STIM2 could be a therapeutic target of ER stress-induced CRC progression.

Results

Reduced STIM2 levels are associated with poor prognosis of colorectal cancer patients

We analyzed mRNA levels of STIM1 and STIM2 using publicly available data from The Cancer Genome Atlas (TCGA). STIM1 mRNA levels were significantly reduced, and STIM2 mRNA levels were unaltered in both colon and rectal adenocarcinoma (COAD-READ/COREAD) compared to unmatched normal tissue controls (**Figure 1A, B**). However, when we analyzed 20 colorectal tumor samples compared to their paired normal adjacent tissue obtained from patients at the Pennsylvania State University Hershey Medical Center, we observed a significant reduction in both STIM1 and STIM2 mRNA levels in the colorectal tumor samples compared to paired normal adjacent tissues (**Figure 1C**). Accessing TCGA data through UALCAN analysis portal (Chandrashekar *et al*, 2017) showed that Orai1, Orai2, and Orai3 mRNA levels were significantly upregulated in COAD patients (**Supplementary Figure 1I-K**). High STIM1 and low STIM2 expression were associated with TP53 mutation (**Supplementary Figure 1A, B**). However, we did not observe an association between STIM1 or STIM2 mRNA levels with mutations in phosphoinositide 3-kinases (PI3K), KRAS, or NRAS (**Supplementary Figure 1C-H**). Interestingly STIM2 mRNA, but not STIM1 mRNA levels correlated with high BRAF mutation (**Supplementary Figure 1G-H**). Further analysis revealed a significant reduction in STIM1 mRNA levels at all stages and slight upregulation of STIM2 at early (stage I/II) and no changes at later stages (stage III/IV) of COAD-READ patient samples (**Figure 1D, E**). Subsequently, Kaplan-Meier analysis showed a strong correlation between reduced STIM2 expression and poor prognosis in COAD or READ patients (**Figure 1F, G**). However, STIM1 expression did not correlate with the survival of COAD or READ patients (**Figure 1H, I**). Contrary to this, higher expression of Orai3 but not Orai1/2 was associated with poor prognosis in COAD patients (**Supplementary Figure 1L-N**). These data raise a very important question: how can two ER Ca^{2+} sensors, STIM1 and STIM2 that are established as synergistic activators of SOCE in healthy mammalian cell types, have differences in expression in colorectal cancer tissues and be associated with different outcomes of colorectal cancer patients? This suggests that the functions of STIM1 and STIM2 in colorectal cancer are quite unique, prompting us to explore the functions of STIM1 and STIM2 in colorectal cancer progression and whether their effects are mediated by SOCE.

Loss of STIM2 promotes tumor growth and metastasis

Given that STIM1 and STIM2 are differentially expressed and that their expression levels show differences in association with CRC patient outcome, we investigated their functions in CRC. Thus, we focused our efforts on a comparative analysis of STIM1 and STIM2 in CRC progression and metastasis. We generated STIM1 knockout (STIM1 KO), STIM2 knockout (STIM2 KO), and STIM1/2 double KO (STIM DKO) cells from two human parental cell lines, HCT116 and DLD1 using CRISPR-Cas9 system (see methods for details). Sequence-specific guide RNAs for STIM1 and STIM2 were used to disrupt the gene and generate multiple knockout clones (see methods). Western blot analysis of wildtype HCT116, and their knockout clones: STIM1 KO #01, STIM1 KO #02, STIM2 KO #15, STIM2 KO #31, STIM DKO #22, and STIM DKO #34 showed complete loss of STIM1 and STIM2 proteins from their respective knockout clones (**Supplementary Figure 2A-C**). Similarly, western blot analysis of wildtype DLD1, and their knockout clones: STIM1 KO

#03, STIM1 KO #05, STIM2 KO #04, STIM2 KO #09, STIM DKO #01, and STIM DKO #07 demonstrated complete loss of STIM1 and STIM2 proteins from their respective knockout clones (**Supplementary Figure 2D-F**). We did not observe any apparent compensation of STIM1 or STIM2 proteins in HCT116 STIM2 KO and STIM1 KO clones, respectively (**Supplementary Figure 2A-C**). However, a slight but significant reduction in STIM2 protein level was observed in DLD1 STIM1 KO clones (**Supplementary Figure 2D-F**). Fura-2 Ca^{2+} imaging was performed in each HCT116 and DLD1 knockout clone to functionally document STIM protein knockout. SOCE was measured in response to store depletion with 100 µM ATP in nominally Ca^{2+} free bath solution and subsequent addition of 2 mM Ca^{2+}. HCT116 and DLD1 STIM1 KO and STIM DKO clones showed an almost complete abrogation of SOCE. HCT116 and DLD1 STIM2 KO clones exhibited a 50-70% reduction in peak SOCE compared to their respective controls, in line with our previous studies (Emrich *et al.*, 2019), suggesting a significant contribution of STIM2 to SOCE in CRC cells (**Supplementary Figure 2G-J**)

Using these KO cells, we then utilized an intrasplenic xenograft model where luciferase-tagged parental HCT116, STIM1 KO #01, STIM2 KO #15, and STIM DKO #22 cells (5 X 10^5 cells/mouse) were injected into the spleen of NOD-SCID mice (**Figure 2A**). Xenograft experiments were performed in two independent runs with 15 mice/group and mice were monitored weekly before being sacrificed at week 6. However, only the second run included mice injected with STIM DKO cells and therefore this group includes only 15 mice while the other three groups of mice (HCT116, STIM1 KO and STIM2 KO groups) include 30 mice/group. The *in vivo* metastasis and primary tumor growth were monitored through IP injection to mice with 100 µl luciferin and recording the total flux using In Vivo Imaging System (IVIS). We observed a significant increase in total luciferase luminescence flux in mice injected with HCT116 STIM2 KO #15 and STIM DKO #22 cells compared to parental HCT116 or STIM1 KO #01 cells (**Figure 2B, C**), suggesting that the loss of STIM2 enhances tumor growth. Furthermore, consistent with total flux measurement, the primary tumor weight at the time of sacrifice (6 weeks post-injection) was substantially higher in STIM2 KO #15 and STIM DKO #22 compared to HCT116 or STIM1KO #01 xenografted mice (**Figure 2D, E**).

A careful analysis of luciferase luminescence revealed that NOD-SCID mice xenografted with STIM2 KO #15 and STIM DKO #22 clones of HCT116 had luciferase activity other than in the primary tumor site, suggesting metastasis to distant organs (**Figure 2B**). Indeed, we observed a significantly higher luminescence in the liver, lung, and colon of STIM2 KO #15 and STIM DKO #22 compared to parental HCT116 or STIM1 KO #01 injected mice (**Figure 2F-I**). In mice injected with either parental HCT116 cells or STIM1 KO cells, out of the 28 (for HCT116) and 27 (for STIM1 KO) surviving mice at week 6, 16 mice/group showed metastasis to distant organs. For the case of mice injected with either STIM2 KO cells or STIM DKO cells, all surviving mice at week 6 (13 STIM2 KO-injected mice and 10 STIM DKO-injected mice) showed metastasis to distant organs. No significant difference was observed in luciferase luminescence in the kidney and heart of HCT116, STIM1 KO #01, STIM2 KO #15, and STIM DKO #22 cells (**Supplementary Figure 2K-M**). Survival analysis using the Kaplan Meier plot showed that NOD-SCID mice injected with STIM2 KO #15 and STIM DKO #22 cells had significantly reduced survival compared to HCT116 or STIM1 KO #01 injected mice (**Figure 2J**), suggesting that

enhanced metastasis is the primary cause of lethality in STIM2 KO #15, and STIM DKO #22 xenografted mice. Collectively, these results show that loss of STIM2 enhances CRC tumor growth and metastasis.

Deletion of STIM2 enhances spheroid formation, migration, and invasion of CRC cells

To delineate the mechanisms of increased tumor size and enhanced metastasis of STIM2 KO CRC cells, we performed spheroid formation, migration, and invasion assays. Parental cells, STIM1 KO, STIM2 KO, and STIM DKO clones of HCT116 and DLD1 cells were assessed for spheroid formation in ultra-low attachment round bottom 96-well plates. The cell-covered area was measured to determine the spheroid size. Within three days after spheroid formation, we observed a significant increase in spheroid size in STIM2 KO and STIM DKO clones compared to STIM1 KO clones and parental cells for both HCT116 and DLD1 (**Figure 3A-C**). On the other hand, we did not observe any significant difference in spheroid size between HCT116/DLD1 STIM1 KO clones and the parental cells (**Figure 3A-C**). Interestingly, we observed specifically in STIM2 KO and STIM DKO clones that some cells were loosely attached to the primary spheroid and were forming secondary spheroids (marked with red arrows, **Figure 3A**). Recent studies showed that cells that are loosely attached to the main spheroid body have higher migration and invasion potential (Stadler *et al*, 2018). Therefore, we investigated the migration and invasion properties of STIM1 KO, STIM2 KO, and STIM DKO clones of HCT116 and DLD1. We performed the gap closure assay and the Boyden chamber assay as means to quantify contact dependent migration and chemotaxis-dependent migration and invasion, respectively (Decaestecker et al., 2007; Guy et al., 2017). We found a significant increase in gap closure in STIM1 KO, STIM2 KO, and STIM DKO clones of both HCT116 and DLD1 cells at 24 hr compared to controls (**Supplementary Figure 3E-H**). Interestingly, when we performed migration and invasion assays using Boyden chambers (Matrigel-coated for invasion assays) we revealed a significant and selective increase in migration and invasion of STIM2 KO and STIM DKO clones of HCT116 and DLD1 cells compared to their respective controls (**Figure 3D-G**). However, the migration and invasion of STIM1 KO of HCT116 and DLD1 cells were either significantly reduced or unaffected compared to their respective parental cell controls (**Figure 3D, G**), suggesting a specific effect of STIM2 loss on chemotaxis-dependent migration and invasion. Consistent with increased invasion, GSEA analysis showed that hallmark genes of Endothelial Mesenchymal transition (EMT) were significantly enriched in STIM2 KO and STIM DKO cells (**Figure 5**), with matrix metalloproteases 16 (MMP16) transcript being one of the EMT genes significantly upregulated in all clones of HCT116 cells following STIM2 KO and STIM DKO. This was validated in STIM2 KO and STIM DKO of HCT116 and DLD1 cells compared to control cells (**Figure 3 H and J**). However, we observed a significant decrease in MMP14 mRNA levels in STIM1 KO, STIM2 KO, and STIM DKO of HCT116 and DLD1 cells compared to control cells (**Figure 3I and K**), indicating that MMP16 may be one of the regulators of invasion in STIM2 KO and STIM DKO colorectal cancer cells.

When we performed proliferation assays using the CyQUANT dye, we observed a substantial reduction in proliferation of all STIM1 KO, STIM2 KO, and STIM DKO clones of HCT116 and DLD1 cells compared to control at 48 hr and 72 hr in culture (**Supplementary Figure 3A, B**).

Nevertheless, at 72 hr, the proliferation of STIM2 KO and STIM DKO clones was significantly higher than the STIM1 KO clones of HCT116 and DLD1 (**Supplementary Figure 3A, B**). We also performed *in vitro* colony formation assays to determine cell survival. Similar to proliferation assays, there was a significant decrease in the number of colonies formed by STIM1 KO, STIM2 KO, and STIM DKO clones of HCT116 cells compared to control cells. Nevertheless, the number of colonies formed by STIM2 KO and STIM DKO cells was significantly higher than that of STIM1 KO cells (**Supplementary Figure 3C, D**).

Given that the loss of STIM1 and STIM2 expression differentially affect COREAD cell metastatic behavior, suggests that their action is SOCE independent. To unequivocally rule out the involvement of SOCE in the increased CRC migration and invasion triggered by the loss of STIM2, we generated Orai1 KO clones and Orai1, Orai2, and Orai3 triple KO (Orai TKO) clones of HCT116 cells using the CRISPR-Cas9 system. RT-qPCR analysis showed the absence of Orai1 mRNA from Orai1 KO and the absence of Orai1, Orai2, and Orai3 mRNA from Orai TKO clones of HCT116 (**Supplementary Figure 3I-K**). As expected, Fura-2 Ca^{2+} imaging showed almost complete loss of SOCE in HCT116 Orai1 KO and Orai TKO cells (**Supplementary Figure 3L, M**). As compared to control cells, Orai1 KO and Orai TKO clones of HCT116 showed a significant increase in gap closure in wound healing assays in a manner reminiscent of all STIM knockout clones (**Supplementary Figure 3N-P**). However, unlike STIM2 KO and STIM DKO cells, Orai1 KO and Orai TKO cells showed decreased migration and invasion in the Boyden chamber assays (**Figure 3L, M**). These data strongly argue that the effect of STIM2 loss on chemotaxis-mediated CRC migration and invasion is Orai- and SOCE-independent.

Loss of STIM2 leads to CRC mitochondrial remodeling and metabolic reprogramming

Previous studies in primary T cells, B cells, airway smooth muscle cells and astrocytes have shown that STIM1 is required for antigen- and growth factor-mediated induction of glycolysis and mitochondrial metabolism (Emrich *et al*, 2023; Johnson *et al*, 2022; Kaufmann *et al*; Novakovic *et al*, 2023; Vaeth *et al*, 2017). Therefore, we performed whole-cell metabolomics on parental HCT116, STIM1 KO #01, STIM2 KO #15, and STIM DKO #22 clones of HCT116 cells and observed a marked change in polar metabolites between STIM1 KO, STIM2 KO, and STIM DKO clones compared to control HCT116 cells (**Supplementary Figure 4A-C**). Interestingly, the STIM2 KO #15 and STIM DKO #22 clones showed a significant alteration in polar metabolites compared to the STIM1 KO #01 clone of HCT116 cells (**Supplementary Figure 4D, E**). Further analysis of metabolomics data showed that the metabolites of the glycolysis pathway were upregulated in all three replicates of STIM2 KO #15 and STIM DKO #22 clones compared to STIM1 KO #01 and HCT116 control (**Figure 4A**). Since perturbation of STIM2 function led to upregulation of glycolytic metabolites, we used Seahorse XFe24 to measure the extracellular acidification rate (ECAR) of all HCT116 and DLD1 cell variants. Consistent with the metabolomics data, the glycolytic capacity of STIM2 KO and STIM DKO clones was significantly increased. However, glycolysis was significantly decreased in STIM1 KO clones of HCT116 and DLD1 as well as in Orai1 KO and Orai TKO clones of HCT116 compared to their respective controls (**Figure 4B, and Supplementary Figure 5A, B**). Furthermore, we measured glucose and lactate in growth media using the YSI bioanalyzer system and observed a significant increase in

glucose consumption and lactate generation by STIM2 KO and STIM DKO clones of HCT116 cells (**Figure 4C, D**). In contrast, STIM1 KO clones of HCT116 cells showed a significant decrease in glucose consumption and lactate generation compared to control (**Figure 4C, D**), suggesting that STIM2 regulates the metabolic transformation of CRC cells in a SOCE-independent manner. The RNA sequencing analysis from STIM1 KO, STIM2 KO, and STIM DKO clones of HCT116 revealed that Solute carrier family 2 A1 (SLC2A1), also known as glucose transporter member 1 (GLUT1), was significantly upregulated in STIM2 KO and STIM DKO clones compared to STIM1 KO or HCT116 (**Figure 5A-D**). Western blot analysis determined that, indeed, the protein levels of GLUT1 were significantly upregulated in STIM2 KO and STIM DKO clones of HCT116 and DLD1 cells (**Figure 4G, H, and Supplementary Figure 5C, D**). There was no change in GLUT1 protein levels in STIM1 KO clones of HCT116 and DLD1 cells and in Orai1 KO and Orai TKO clones of HCT116 cells compared to their respective controls (**Figure 4G, H, and Supplementary Figure 5E, F**), suggesting that increased GLUT1 levels supports the increased ECAR, glucose consumption, and lactate generation of STIM2 KO cells. These data indicate that STIM2 regulates glycolysis of colorectal cells independently of SOCE.

The metabolic analysis also showed a significant increase in citric acid cycle metabolites in STIM2 KO #15 and STIM DKO #22 compared to STIM1 KO #01 clones and HCT116 cells (**Figure 4F**). Therefore, we determined the oxygen consumption rate (OCR) of all HCT116 and DLD1 cell variants using Seahorse assays. We observed a significant increase in maximal respiratory capacity in STIM2 KO and STIM DKO clones of HCT116 and DLD1 cells compared to control cells (**Figure 4E and Supplementary Figure 5G**). Conversely, the maximal respiratory capacity was significantly reduced in STIM1 KO clones of HCT116 and DLD1 cells and in Orai1 KO and Orai TKO clones of HCT116 cells (**Figure 4E and Supplementary Figure 5G, H**). Further, we assessed the protein levels of mitochondrial respiratory complex I-V to determine whether increased OCR in STIM2 KO and STIM DKO clones was due to increased protein levels of these complexes. Interestingly, we did not observe a significant change in protein levels of NADH dehydrogenase [ubiquinone] 1 β subcomplex subunit 8 (NDUFB8, Complex-I), Succinate dehydrogenase [ubiquinone] iron-sulfur subunit (SDHB, Complex-II), Cytochrome b-c1 complex subunit 2 (UQCRC2, Complex-III), Cytochrome c oxidase subunit 1 (MTCO1, Complex IV), and ATP synthase subunit α (ATP5A, Complex-V) in STIM1 KO, STIM2 KO and STIM DKO clones of HCT116 cells (**Supplementary Figure 5I-N**). We measured the mitochondrial and cytosolic superoxide levels by staining cells with MitoSOX or CellROX respectively. There was no significant change in mitochondrial and cytosolic superoxide levels in STIM1 KO, STIM2 KO and STIM DKO clones of HCT116 cells (**Supplementary Figure 5O, P**). Mitochondrial membrane potential measured by TMRE staining showed no difference in mitochondrial membrane potential between STIM1 KO, STIM2 KO and STIM DKO clones of HCT116 cells (**Supplementary Figure 5Q**). Multiple studies reported that the pentose phosphate pathway (PPP) is required for nucleotide biosynthesis, and plays a major role in metabolism, proliferation, and chemoresistance of colorectal cancer (Gao *et al*, 2019; Jiang *et al*, 2014; Lin *et al*, 2022; Patra & Hay, 2014). Our metabolomic analysis showed a significant increase in PPP metabolites in STIM2 KO #15, STIM DKO #22 clones, compared to STIM1 KO #01 or HCT116 control cells (**Supplementary Figure 5R**), suggesting that the loss of STIM2 enhances PPP to support

colorectal cancer growth. Collectively these data show that loss of STIM2 positively regulates CRC cell metabolic activity.

Because changes in overall cell metabolism are typically associated with changes in either mitochondrial structure, number, or function, we performed transmission electron microscopy (TEM) imaging to assess any changes in mitochondrial number and structure. The single mitochondrion area and perimeter were slightly decreased, and mitochondria were slightly more circular in STIM2 KO #15 and STIM DKO #22 clones compared to STIM1 KO #01 clone of HCT116 (**Figure 4I-L)**. However, we found a significant increase in mitochondrial number in STIM2 KO #15, STIM DKO #22 clones, and a decrease in mitochondrial number in STIM1 KO #01 with longer single mitochondria compared to HCT116 control (**Figure 4I, M**). We stained cells with MitoTracker green to further examine the mitochondrial number with flow cytometry. We found a significant increase in MitoTracker intensity in STIM2 KO and STIM DKO clones of HCT116 and DLD1 cells compared to control cells (**Figure 4 N, O**). The MitoTracker intensity was significantly decreased in STIM1 KO clones of HCT116 and DLD1 compared to control cells (**Figure 4 N, O**). Mitochondrial DNA, as measured by qPCR was markedly increased in STIM2 KO and STIM DKO clones and significantly decreased in STIM1 KO clones of HCT116 and DLD1 cells compared to control (**Figure 4 P, Q**).

Loss of STIM2 promotes transcriptional reprogramming of colorectal cancer cells

We performed transcriptional profiling of parental cells, STIM1 KO, STIM2 KO, and STIM DKO clones of HCT116 using RNA sequencing. Approximately 10,000 genes emerged as common hits, which were differentially expressed between HCT116 cell variants (**Figure 5A-D and Supplementary Figure 6A- D**). Gene set enrichment analysis (GSEA) revealed that the gene set involved in cMyc regulation, Oxidative phosphorylation (OXPHOS), and unfolded protein response (UPR) were upregulated in STIM2 KO and STIM DKO clones of HCT116 versus control. Among the Hallmark gene sets, cMyc target V1, V2, OXPHOS, Endothelial to mesenchymal (EMT), G2M, and E2F targets were positively regulated in STIM2 KO and STIM DKO clones of HCT116 (**Figure 5 E-N Supplementary Figure 7 A-C**). We aligned differentially expressed genes to the Kyoto Encyclopedia of Genes and Genomes (KEGG) pathway analysis and found that ribosome biogenesis, RNA transport, and translation pathways were significantly upregulated in STIM2 KO and STIM DKO clones of HCT116 (**Supplementary Figure 6E-J**), suggesting increased translation and protein accumulation. We did not observe an enrichment of translation pathways in STIM1 KO clones of HCT116 cells (**Supplementary Figure 6E, F**). We also performed gene ontology (GO) enrichment analysis to understand the distribution of differentially expressed genes in biological processes (GO-BP). Like the KEGG analysis, GO-BP analysis also showed significant enrichment of ribosome biogenesis, RNA metabolism, and translation initiation enrichment in STIM2 KO and STIM DKO clones of HCT116 as compared to HCT116 control (**Supplementary Figure 6K-P**). Collectively, these data show that deletion of STIM2 upregulates ribosome biogenesis and translation, suggesting enhanced UPR and increased protein accumulation. Importantly, the loss of STIM2 affects completely different pathways

compared to that of STIM1, lending further support to a SOCE-independent function of STIM2 in CRC progression.

Loss of STIM2 leads to increased SERCA2 and ER Ca^{2+} levels

It is well established that ER Ca^{2+} homeostasis is critical for ER function and protein synthesis and that altered ER Ca^{2+} levels are directly linked to ER stress and initiation of the unfolded protein response (UPR) (Corazzari *et al.*, 2017; Mekahli *et al*, 2011; Preissler *et al.*, 2020). Therefore, we performed direct ER Ca^{2+} measurement using the ER-targeted genetically encoded indicator, R-CEPIA1$_{ER}$ (Suzuki *et al*, 2014). Cells were stimulated with 300 µM ATP in 0 mM Ca^{2+} in Hanks Balanced Salt Solution (HBSS) to cause maximal depletion of ER Ca^{2+}, followed by ATP washout and addition of 2 mM Ca^{2+} to measure ER Ca^{2+} refilling. To standardize these experiments, we first transfected HCT116 and HEK293 cells with R-CEPIA1$_{ER}$ and determined side by side ER Ca^{2+} release and refilling in these cells. Interestingly, the ER-Ca^{2+} depletion rate was significantly faster and refilling rate was slower in HCT116 cells compared the HEK293 cells **(Supplementary Figure 8 A-F)**. We performed similar experiments using STIM1 KO, STIM2 KO, and STIM DKO clones of HCT116 and DLD1 cells and we observed a significantly elevated basal ER Ca^{2+} in STIM2 KO and STIM DKO clones of HCT116 and DLD1 (**Figure 6 A-C and E-G**). The ER Ca^{2+} depletion rate was also increased in STIM2 KO and STIM DKO clones of HCT116 and DLD1 as compared to STIM1 KO clones and parental control cells (**Figure 6 D, H**), suggesting that overall ER Ca^{2+} levels were elevated in STIM2 KO and STIM DKO clones. We also measured ER Ca^{2+} levels in Orai1 KO and Orai TKO clones of HCT116. There was no marked difference observed in basal ER Ca^{2+} or ER Ca^{2+} depletion rate between Orai1 KO, Orai TKO cells compared to HCT116 control **(Supplementary Figure 8G-J)**. The Maximal ER Ca^{2+} refilling and ER Ca^{2+} refilling rate were significantly reduced in Orai1 KO and Orai TKO clones of HCT116 compared to control **(Supplementary Figure 8K, L)**. To determine the cause of increased ER Ca^{2+} in STIM2 KO and STIM DKO cells, we measured mRNA levels of SERCA. There was a significant increase in mRNA levels of SERCA2 in STIM2 KO and STIM DKO clones of HCT116 cells (**Figure 6I-K**). We also observed a marked increase in SERCA2 protein levels in STIM2 KO, and STIM DKO clones of HCT116 and DLD1 cells (**Figure 6L-Q**). SERCA2 protein levels were unaltered or slightly reduced in STIM1 KO clones of HCT116 and DLD1 cells (**Figure 6L-Q**). We measured the protein levels of the three IP_3R subtypes and observed no change in protein levels between STIM1 KO, STIM2 KO, and STIM DKO clones of HCT116 and DLD1 cells **(Supplementary Figure 8M-S)**. Please note that the protein for the IP_3R2 isoform was not detectable in HCT116 cells. Collectively, these data suggest that STIM2 regulates ER Ca^{2+} homeostasis, and loss of STIM2 increases basal ER Ca^{2+} by upregulating SERCA2 levels.

STIM2 deficiency promotes cMyc stabilization and enhances PPARγ levels

The cMyc oncogene is a known target of chromosomal translocation and gene replication in cancer progression. cMyc is a transcription factor that induces proliferation by upregulating expression of genes that regulate the cell cycle, genes required for energy metabolism such as glycolytic genes, and ribosome biogenesis (Gao *et al*, 2009; Hart *et al.*, 2012; Meyer & Penn, 2008). Ribosome biogenesis has been linked to increased protein synthesis regulated by cMyc activity and is required for survival of cancer cells (Arabi *et al*, 2005; Barna *et al*, 2008; Chan *et al*, 2011;

Destefanis *et al.*, 2020; Grandori *et al*, 2005; Iritani & Eisenman, 1999; Popay *et al*, 2021). RNA sequencing analysis of STIM2 KO and STIM DKO clones of HCT116, showed that cMyc targets and ribosome biogenesis genes pathways were enriched (**Figure 5, Supplementary Figure 6**), suggesting that cMyc is active in STIM2 KO and STIM DKO clones. Therefore, we measured cMyc levels in STIM1 KO, STIM2 KO, and STIM DKO clones of HCT116 and DLD1 cells using western blotting. Indeed, cMyc phosphorylation (Ser62) was markedly increased in both STIM2 KO and STIM DKO clones of HCT116 and DLD1 cells (**Figure 7 A, B**). There was no change in cMyc phosphorylation in STIM1 KO clones of HCT116 and DLD1, Orai1 KO, and Orai TKO clones of HCT116 cells as compared to their respective clones (**Figure 7A, B and Supplementary Figure 9A, B**). ERK is known to stabilize cMyc to regulate cancer cell proliferation and growth by regulating cell cycle checkpoint genes (Marampon *et al*, 2006; Sears *et al*, 2000; Tsai *et al*, 2012). STIM2 KO and STIM DKO clones of HCT116 and DLD1 had significantly increased ERK phosphorylation (Thr202/Tyr204) compared to their respective controls (**Figure 7A, C)**. ERK phosphorylation was unaltered in STIM1 KO, Orai1 KO, and Orai TKO clones as compared to control (**Figure 7A, C and Supplementary Figure 9C, D**). Although we did not see any significant changes in cMyc protein levels between wildtype and different STIM knockout clones of HCT116 and DLD1 cells, TCGA analysis using UALCAN showed that cMyc mRNA levels were significantly upregulated in primary tumors of COAD patients (**Supplementary Figure 9E**). The mRNA levels of cMyc were also upregulated in all cancer stages of COAD patients (**Supplementary Figure 9F**). Using cBioPortal, we found that cMyc expression has a stronger negative correlation with the expression of STIM2 than with that of STIM1 in CRC (**Supplementary Figure 9G, H**).

We consistently observed that GLUT1 protein levels were significantly upregulated in STIM2 KO and STIM DKO clones of HCT116 and DLD1 cells (**Figure 4G, H, and Supplementary Figure 5C, D**). Since cMyc is a known molecular driver of glycolysis and tumor metabolic reprogramming (Vyas *et al*, 2016), we determined the role of STIM2 in regulating tumor metabolism through cMyc downstream targets. cMyc is known to regulate cellular energetics by affecting mitochondrial mass through the PGC1α/PPARɣ complex (Bost & Kaminski, 2019; Morrish & Hockenbery, 2014; Vyas *et al.*, 2016). We observed a significant increase in mitochondrial biomass in both STIM2 KO and STIM DKO clones of HCT116 and DLD1 cells (**Figure 4I-Q**). We measured the protein levels of PGC1α and PPARɣ using western blotting. There was no significant change in PGC1α levels between STIM1 KO, STIM2 KO, STIM DKO, Orai1 KO and Orai TKO clones compared to control (**Figure 7D-G, and Supplementary Figure 9I, J**). However, PPARɣ levels were significantly upregulated in STIM2 KO and STIM DKO clones of HCT116 and DLD1 cells (**Figure 7H, I**). There was no apparent change in PPARɣ levels in STIM1 KO, Orai1 KO, and Orai TKO clones (**Figure 7H, I and Supplementary Figure 9K, L**), suggesting that loss of STIM2 leads to cMyc stabilization, increased PPARɣ and enhanced mitochondrial biogenesis to meet the energy demand of growing CRC cells.

STIM2 deficiency promotes ATF4-dependent ER stress

The GSEA, KEGG, and DO analysis of the RNA sequencing data determined that cMyc targets, UPR, E2F targets, and ribosome biogenesis pathways were selectively enriched in STIM2 KO and

STIM DKO clones of HCT116 (**Figure 5, Supplementary Figure 6**). Increased ribosome biogenesis is one of the indicators of increased protein synthesis, which is associated with UPR (Destefanis *et al.*, 2020; Popay *et al.*, 2021). We also observed a marked increase in SERCA2 protein levels and ER Ca^{2+} levels in STIM2 KO and STIM DKO cells (**Figure 6**). The disruption of ER Ca^{2+} homeostasis is known to induce ER stress (Corazzari *et al.*, 2017; Deniaud *et al*, 2008; Mekahli *et al.*, 2011). BiP is an ER chaperone, also known as GRP78/HSPA5, which regulates mammalian ER stress response. BiP levels were significantly and selectively upregulated in STIM2 KO and STIM DKO clones of HCT116 and DLD1 cells (**Figure 8A, B**). No apparent increase was observed in BiP levels in STIM1 KO clones of HCT116 and DLD1, and in Orai1 KO and Orai TKO clones of HCT116 as compared to their respective controls (**Figure 8A, B and Supplementary Figure 10G, H**). To determine which branch of ER stress pathway is triggered by the loss of STIM2, we measured ATF4, IRE1α and ATF6 levels and found that only ATF4 levels were significantly upregulated in STIM2 KO and STIM DKO clones of HCT116 and DLD1 (**Figure 8C, D and Supplementary Figure 10A, B**). There was no change in IRE1α levels in STIM1 KO, STIM2 KO, and STIM DKO clones of HCT116 and DLD1 cells (**Figure 8E, F and Supplementary Figure 10C, D**). Except for DLD1 STIM2 KO #04 cells, we did not observe a change in ATF6 levels in STIM1 KO, STIM2 KO, and STIM DKO clones of HCT116 and DLD1 cells **(Figure 8G, H and Supplementary Figure 10E, F)**. Furthermore, Orai1 KO and Orai TKO clones of HCT116 did not show any changes in ATF4 and IRE1α levels (**Supplementary Figure 10I-L**). Surprisingly, ATF6 levels were significantly upregulated in Orai1 KO clones but not in Orai TKO clones of HCT116 (**Supplementary Figure 10M, N**). We also determined PERK and eIF2α levels and found that the phosphorylation of eIF2α was significantly upregulated in STIM2 KO and STIM DKO clones of HCT116 cells (**Figure 8I, J**). PERK phosphorylation showed strong variability and while PERK phosphorylation trended towards an increase in STIM2 KO and STIM DKO cells, this increase did not reach statistical significance (**Figure 8K, L**). These data show that the BiP/eIF2α/ATF4 pathway is activated in response to ER stress in STIM2 KO and STIM DKO clones of HCT116 and DLD1 cells. This ER stress pathway is not active in STIM1 KO, Orai1 KO, and Orai TKO cells, further supporting that STIM2 regulates ER stress in a SOCE-independent manner.

Discussion

Ca^{2+} ions play a critical role in a myriad of biological functions, including cellular metabolism, bioenergetics, transcription, cellular proliferation, cell death, and cellular stress responses. Recent advances have shown that compartmentalized Ca^{2+} within the ER, mitochondria, endolysosomes and Golgi are interconnectedly and tightly regulated and this regulation is essential for normal cellular function (Stewart *et al*, 2015). Perturbed Ca^{2+} homeostasis within cancer cells alters their transcriptional profile to support requirements for growth and metastasis (Jones & Hazlehurst, 2021; Marchi & Pinton, 2016; Pathak & Trebak, 2018; Zheng *et al*, 2022). Mitochondria and ER are tightly interlinked, and perturbation of Ca^{2+} homeostasis of any of these organelles strongly affects their function (Bustos *et al*, 2017). Changes in mitochondrial Ca^{2+} homeostasis have been implicated in multiple disease conditions, including cancer (Pathak & Trebak, 2018; Vasan *et al*, 2020). ER Ca^{2+} regulates protein synthesis, ER structure, function, and ER stress responses (Moy *et al*, 2022; Papp *et al*, 2012). Multiple cancer types have been linked to ER stress, which regulates cancer progression through transcriptional reprograming and metabolic transformation to meet the needs for cancer growth and dissemination (Chen & Cubillos-Ruiz, 2021; Corazzari *et al.*, 2017).

Even though STIM2 is one of the major components of SOCE, its role in cancer progression has remained obscure. Our TCGA data analysis of colorectal cancer patients showed that STIM2 mRNA levels are unaltered while STIM1 mRNA levels were significantly reduced in all stages of cancer progression. However, survival analysis of these patients showed a strong correlation between low STIM2 mRNA levels and poor prognosis in both COAD and READ patients. Furthermore, we found no correlation between STIM1, Orai1 or Orai2 expression and survival of COAD and READ patients. Interestingly, Orai3 levels were significantly upregulated in primary tumors, and higher Orai3 mRNA level was strongly correlated with poor prognosis of CRC patients. As such, future studies are required to determine the function of Orai3 in CRC progression.

In the past few years, many studies have shown a pro-growth function of STIM1 and Orai1 in various cancer types, including breast cancer, colorectal cancer, glioblastoma, and melanoma (Khan *et al*, 2020; Mo & Yang, 2018; Motiani *et al*, 2010; Motiani *et al*, 2013a; Motiani *et al*, 2013b; Shapovalov *et al*, 2021; Xie *et al*, 2016). In most cancer cell types, blocking or reducing STIM1/Orai1 function led to reduced SOCE and subsequent reduction in proliferation and migration (Faris *et al*, 2022; Motiani *et al.*, 2013a; Moy *et al.*, 2022; Wang *et al*, 2015; Yang *et al*, 2013; Yang *et al*, 2009; Zhang *et al*, 2015). Consistently, we show here that loss of STIM, or Orai proteins leads to reduced proliferation. When we measured colorectal cancer cell migration using the wound healing assay, we saw significantly increased migration of cells lacking STIM or Orai proteins. However, serum-induced migration and invasion in Boyden chamber assays showed reduced migration and invasion of STIM1 KO cells while migration and invasion of STIM2 KO and STIM DKO cells were greatly increased. Cell migration in wound healing assays is mostly driven by cell-cell interactions while migration in Boyden chamber assays is largely contributed by chemotaxis. Consequently, we used spheroid to assess proliferation, migration, and invasion and found that the spheroid size was significantly larger in STIM2 KO and STIM DKO cells. The spheroids of STIM2 KO and STIM DKO cells also had a significant amount of loosely attached

cells, indicating a pro-migratory and pro-metastatic phenotype. Surprisingly, STIM DKO cells showed a phenotype similar to that of STIM2 KO cells rather than STIM1 KO, strongly arguing that the phenotype of STIM2 KO cells is Orai- and SOCE-independent. Our *in vivo* xenograft studies showed enhanced tumor growth and metastasis specifically in STIM2 KO and STIM DKO cells. Interestingly, Aytes et al. reported that STIM2 overexpression in colorectal cancer cells confers a tumor suppressor phenotype (Khan *et al.*, 2020; Wang *et al.*, 2015; Yang *et al.*, 2009). Although these studies did not provide a mechanism by which STIM2 suppresses tumor growth, they agree with our findings.

While reduced SOCE by loss of STIM1 or Orai1 in normal cells reduces mitochondrial metabolism and glycolysis (Emrich *et al.*, 2023; Johnson *et al.*, 2022; Maus *et al*, 2017; Novakovic *et al.*, 2023; Vaeth *et al.*, 2017; Yoast *et al*, 2021), the function of STIM2 in cellular metabolism of either normal or cancerous cells has remained unclear. Here we show that loss of STIM2 results in increased glycolysis, mitochondrial respiration, and mitochondrial biogenesis. Similarly, STIM1/2 double knockout cells showed a similar phenotype. However, Orai1 KO and Orai1/2/3 triple KO cells behaved in a similar fashion to STIM1 KO cells, where glycolysis and mitochondrial respiration were reduced. These findings underscore that STIM2 drives the metabolic transformation of STIM2 KO and STIM DKO cells in a SOCE-independent manner. Further, the activity of cMyc, a known regulator of transcription of genes required for metabolic transformation, proliferation, and metastasis (Li *et al.*, 2005; Morrish & Hockenbery, 2014; Satoh *et al.*, 2017), was significantly enhanced in both STIM2 KO and STIM DKO cells and cMyc expression negatively correlates with STIM2 expression in CRC patients, suggesting that CRC tumors lose STIM2 to support an optimized ER stress response and cMyc-dependent metabolic reprogramming. Indeed, Tameire et al showed that cMyc activity upregulates ATF4 to relieve cMyc-dependent proteotoxic stress and balance between enhanced protein translation and cancer cell survival/tumor progression. (Tameire *et al.*, 2019). The PPARɣ, a nuclear receptor and known regulator of mitochondrial metabolism genes, was also upregulated in STIM2 KO and STIM DKO cells, suggesting that cMyc might be increasing PPARɣ levels to enhance mitochondrial biogenesis. However, further studies are required to understand how STIM2 loss regulates cMyc/ PPARɣ levels in CRC cells.

The canonical CRC subtype called consensus molecular subtype 2 (CMS2) is characterized by the strong upregulation of cMyc downstream signaling while the CMS3 subtype is known for the enrichment of multiple metabolism signatures (Guinney *et al.*, 2015). The loss of STIM2 caused marked changes in the transcriptional profile of CRC cells, and this change in transcriptional profile matches both canonical CRC subtypes, CMS2 and CMS3. This suggests that loss of STIM2 is likely correlated with poor prognosis in both CMS2 and CMS3 CRC subtypes. Subtype probability scoring determined that CMS2 and CMS3 are closely related and hard to disambiguate (Guinney *et al.*, 2015), in further support of the idea that STIM2 regulates both CMS2 and CMS3 CRC subtypes.

STIM1 and Orai1 are the major regulators of SOCE, and their activation has been studied extensively (Lewis, 2020; Yeung *et al*, 2020). Multiple studies show that under basal conditions and upon moderate ER Ca^{2+} depletion, STIM2 activates SOCE (Brandman *et al*, 2007a; Emrich *et*

al., 2021). In HCT116 and DLD1 CRC cells, maximal activation with 300 μM ATP revealed a complete loss of SOCE in STIM1 KO and STIM DKO conditions with ~ 50% loss of SOCE in STIM2 KO cells. However, both *in vivo* and *in vitro* CRC progression phenotypes were the same between STIM2 KO and STIM DKO cells, suggesting that STIM2 functions in a SOCE-independent mechanism to regulate CRC progression. Our direct measurements of ER Ca^{2+} levels using R-CEPIA$_{ER}$ showed that basal ER Ca^{2+} and SERCA2 protein levels were significantly enhanced in STIM2 KO and STIM DKO cells. Perturbation of ER Ca^{2+} is known to alter mitochondrial Ca^{2+} homeostasis and subsequently cause mitochondrial stress and alter metabolism (Bustos *et al.*, 2017; Marchi & Pinton, 2016). Although, it is well established that ER Ca^{2+} depletion activates ER stress responses (Corazzari *et al.*, 2017; Krebs *et al*, 2015; Zheng *et al.*, 2022), our data indicate that increased ER Ca^{2+} is also associated with selective activation of the ATF4 branch of ER stress. Our RNA sequencing analysis showed that ribosome biogenesis is selectively increased in STIM2 KO and STIM DKO CRC cells, which is a hallmark of increased protein synthesis. We showed that the eIF2α and ATF4 levels are upregulated in STIM2 KO and STIM DKO CRC cells, Therefore, our data suggest that loss of STIM2 initiates the activation of the ATF4 branch of ER stress, likely in response to enhanced ER Ca^{2+}. However, how enhanced ER Ca^{2+} contributes to ER stress and the mechanisms involved require further investigations.

In summary, we have identified a SOCE-independent role of STIM2 in colorectal cancer progression, whereby the loss of STIM2 leads to enhanced tumor growth, metastasis, and poor prognosis. Mechanistically, loss of STIM2 causes increased ER Ca^{2+} levels, protein synthesis, and cMyc stabilization, leading to activation of ER stress response in ATF4 dependent manner. The activation of the ATF4 ER stress pathway causes transcriptional reprogramming and metabolic transformation to support increased metastasis of CRC cells. These changes are the markers of CMS2, and CMS3 subtypes of CRC. Therefore, STIM2 could serve in CRC prognosis or in targeted therapies to inhibit CRC tumor growth and metastasis.

Methods

Key resource table:

Reagent or Resources	Source	Identifier
Antibodies		
ATF6	Abcam	Cat# ab122897, RRID:AB_10899171
ATF4	Cell Signaling Technology	Cat# 11815, RRID:AB_2616025
GLUT1	Cell Signaling Technology	Cat# 12939, RRID:AB_2687899

elF2α	Cell Signaling Technology	Cat# 9722, RRID:AB_2230924
p-elF2α	Cell Signaling Technology	Cat# 3398, RRID:AB_2096481)
IRE1α	Cell Signaling Technology	Cat# 3294, RRID:AB_823545
BIP	Cell Signaling Technology	Cat# 3177, RRID:AB_2119845
PERK	Cell Signaling Technology	Cat# 3192, RRID:AB_2095847
pPERK (Thr980)	Cell Signaling Technology	Cat# 3179, RRID:AB_2095853
cMyc	Cell Signaling Technology	Cat# 5605, RRID:AB_1903938
cMyc	Bio-Rad	Cat# VPA00575,
p-cMyc	Cell Signaling Technology	Cat# 13748, RRID:AB_2687518
MFN2	Cell Signaling Technology	Cat# 11925, RRID:AB_2750893
PPARɣ	Cell Signaling Technology	Cat# 2435, RRID:AB_2166051
PGC1α	Cell Signaling Technology	Cat# 2178, RRID:AB_823600
ERK1/2	Cell Signaling Technology	Cat# 9102, RRID:AB_330744
pERK1/2	Cell Signaling Technology	Cat# 9101, RRID:AB_331646
OXPHOS	Abcam	Cat# ab110413, RRID:AB_2629281

STIM1	Cell Signaling Technology	Cat# 4916; RRID:AB_2271287
STIM2	Cell Signaling Technology	Cat# 4917; RRID: AB_2198021
IP3R1	Yule Lab	NA
IP3R2	Yule Lab	NA
IP3R3	BD Biosciences	Cat# 610313; RRID:AB_397705
SERCA2	Cell Signaling Technology	Cat# 4388S; RRID:AB_2227684
GAPDH	Millipore Sigma	Cat# MAB374, RRID:AB_2107445
IRDye 800CW Goat anti-Mouse	Li-Core Biosciences	Cat# 925-32210, RRID:AB_2687825
IRDye 800CW Donkey anti-Rabbit	Li-Core Biosciences	Cat# 925-32213, RRID:AB_2715510
IRDye 680RD Goat anti-Mouse	Li-Core Biosciences	Cat# 925-68070, RRID:AB_2651128
IRDye 680RD Goat anti-Rabbit	Li-Core Biosciences	Cat# 925-68071, RRID:AB_2721181
Chemicals		
Mito Tracker Green FM	Thermo Fisher Scientific	Cat# M7514
Mito SOX	Thermo Fisher Scientific	Cat# M36008
TMRE	Thermo Fisher Scientific	T669
CellROX	Thermo Fisher Scientific	C10492
Fura-2 AM	Thermo Fisher Scientific	Cat# F1221
FBS	VWR	Cat# MISC-LFSCI-STP
Antibiotic and Antimycotic	Thermo Fisher Scientific	Cat# 15240062
McCoy's 5A	Corning	Cat# 10-050CV

RPMI-1640	Corning	Cat# 10-040CV
Lipofectamine 2000	Thermo Fisher Scientific	Cat# 11668019
TrypLE	Thermo Fisher Scientific	Cat# 12605028
Proteinase K	Viagen Biotech	Cat# 501-PK
Direct PCR lysis reagent	Viagen Biotech	Cat# 302-C
Glucose	Sigma-Aldrich	Cat# D9434
Puromycin	MP Biomedical	Cat# 02100552
RIPA buffer	Sigma	Cat# R0278
ATP	Sigma	Cat# A9187
Cyclopiazonic Acid	Alomone Labs	Cat# C-750
Dextrose	Fisher Scientific	Cat# D14
Tris Base	Fisher Scientific	Cat# BP152-5
NaCl	Fisher Scientific	Cat# S671
MOPS SDS running buffer	Thermo Fisher Scientific	Cat# NP0001
Tris Glycine transfer buffer	Bio-rad	Cat#161-0734
KCl	Fisher Scientific	Cat# P217
$MgCl_2$	Fisher Scientific	Cat# M33
$CaCl_2$	Fisher Scientific	Cat# C614
HEPES	Fisher Scientific	Cat# BP310
LDS sample buffer	Thermo Fisher Scientific	Cat# NP0007
NuPAGE Bis-Tris precast gels	Thermo Fisher Scientific	Cat# NP0321
Polyvinylidene difluoride membrane	Li-Core Biosciences	Cat# 88518
Odyssey Blocking Buffer (TBS)	Li-Core Biosciences	Cat# 937-50003
Dextran sulfate sodium	MP Biomedical	Cat# 0216011080
FluoroBlok	Corning	Cat# 351152
BioCoat™ Tumor Invasion Plate	Corning	Cat# 80774380
BCA assay kit	Thermo Fisher Scientific	Cat# A53225
CyQUANT	Thermo Fisher Scientific	Cat# C35006
cDNA Reverse Transcription Kit	Applied biosystems	Cat# 4368814
DNase I	Thermo Fisher Scientific	Cat# 18068-015
TRIzol	Thermo Fisher Scientific	Cat# 15596018
SYBER select master mix	Thermo Fisher Scientific	Cat# 4472920

Seahorse XF DMEM Medium pH 7.4	Agilent Technologies	Cat# 103575-100
Seahorse XF 100 mM pyruvate solution	Agilent Technologies	Cat# 103578-100
Seahorse XF 200 mM glutamine solution	Agilent Technologies	Cat# 103579-100
Seahorse XF 1.0 M glucose solution	Agilent Technologies	Cat# 103577-100
Seahorse XFp Mito Fuel Flex Test Kit	Agilent Technologies	Cat# 103270-100
Seahorse XFp Glycolysis Stress Test Kit	Agilent Technologies	Cat# 103017-100
Seahorse XFp Cell Mito Stress Test Kit	Agilent Technologies	Cat# 103010-100
Tris Glycine SDS Running Buffer (10X)	Thermo Fisher Scientific	Cat# LC2675
Novex™ 10% Zymogram Plus (Gelatin) Protein Gels, 1.0 mm, 10-well	Thermo Fisher Scientific	Cat# ZY00100
SimplyBlue™ Safe Stain	Thermo Fisher Scientific	Cat# LC6060
Tween 20	Fisher Scientific	Cat# BP337
Cell Lines		
Human colon cancer HCT116 cells (male)	ATCC	Cat# CCL-247, RRID:CVCL_0291
Human colon cancer DLD1 cells (male)	ATCC	Cat# CCL-221, RRID:CVCL_0248
Human colon cancer HCT116 STIM1 KO cells	This paper	N/A
Human colon cancer HCT116 STIM2 KO cells	This paper	N/A
Human colon cancer HCT116 DKO cells	This paper	N/A
Human colon cancer DLD1 STIM1 KO cells	This paper	N/A
Human colon cancer DLD1 STIM2 KO cells	This paper	N/A
Human colon cancer DLD1 DKO cells	This paper	N/A
Human colon cancer HCT116 Orai1 KO cells	This paper	N/A
Human colon cancer HCT116 TKO cells	This paper	N/A

Primer Sequences for RT-qPCR		
MMP14- Forward	5'-AAGAGGAGAAGAGCAAACAG-3'	
MMP14- Reverse	5'-CGGTAGGCACTGAACTTG-3'	
MMP16- Forward	5'-AGCACTGGAAGACGGTTGG-3'	
MMP16- Reverse	5'-CTCCGTTCCGCAGACTGTA-3'	
SERCA1- Forward	5'-GTGATCCGCCAGCTAATG-3'	
SERCA1- Reverse	5'-CGAATGTCAGGTCCGTCT-3'	
SERCA2- Forward	5'-CGCTACCTCATCTCGTCCA-3'	
SERCA2- Reverse	5'-TCGGGTATGGGGATTCAA-3'	
SERCA3- Forward	5'-GATGGAGTGAACGACGCA-3'	
SERCA3- Reverse	5'-CCAGGTATCGGAAGAAGAG-3'	
Orai1- Forward	5'-GATGAGCCTCAACGAGCA CT-3'	
Orai1- Reverse	5'-ATTGCCACCATGGCGAAGC-3'	
Orai2- Forward	5'-TGGCGGAAGCTCTACCTGAG-3'	
Orai2- Reverse	5'-CGGGTACTGGTACTGCGTC-3'	
Orai3- Forward	5'- GAGTGACCACGAGTACCCACC -3'	
Orai3- Reverse	5'- GGGTACCATGATGGCTGTGG -3'	
GAPDH- Forward	5'-CCCTTCATTGACCTCAACTACA-3'	
GAPDH- Reverse	5'-ATGACAAGCTTCCCGTTCTC-3'	
Tubulin- Forward	5'-AGTCCAAGCTGGAGTTCTCTAT-3'	
Tubulin- Reverse	5'-CAATCAGAGTGCTCCAGGGT-3'	
mtDNAR1- Forward	5'-CGGGCTACTACAACCCTTCG-3'	
mtDNAR1- Reverse	5'-GATGGTAGATGTGGCGGGTT-3'	
mtDNAR2- Forward	5'-CTATCCTGCCCGCCATCATC-3'	
mtDNAR2- Reverse	5'-AAGGGAGGGATCGTTGACCT-3'	
mtDNAR3- Forward	5'-TCATCCAAACCCCCTGAAGC-3'	
mtDNAR3- Reverse	5'-CGACTGTGAGTGCGTTCGTA-3'	
genomicDNAR1- Forward	5'-GCAACTTAGAGGTGGGGAGC-3'	
genomic DNAR1- Reverse	5'-AACAAGCTTTGAGTGCAAGAGA-3'	
genomicDNAR2- Forward	5'-GGGTGGGGGAGAGATTACCT-3'	
genomic DNAR2- Reverse	5'-CAATCTGCCCAGAGAAGCCA-3'	
Primer sequences for guide RNA		
ORAI1 g1 CRISPR/Cas9 Guide RNA 5′-GTTGCTCACCGCCTCGA TGT-3′	Trebak Lab (Emrich *et al.*, 2021)	N/A
ORAI2 g1 CRISPR/Cas9 Guide RNA 5′-ACGACAGGGCCTGTACC GAG-3′	Trebak Lab (Emrich *et al.*, 2021)	N/A
ORAI2 g3 CRISPR/Cas9 Guide RNA 5′-CTCATGCGGGGACTCGC TGA-3′	Trebak Lab (Emrich *et al.*, 2021)	N/A

ORAI3 g2 CRISPR/Cas9 Guide RNA 5′-GTTCGTGCACCGCGGCTACC-3′	Trebak Lab (Emrich *et al.*, 2021)	N/A
ORAI3 g4 CRISPR/Cas9 Guide RNA 5′-CCAGAGACTGCACCGCTACG-3′	Trebak Lab (Emrich *et al.*, 2021)	N/A
STIM1 g3 CRISPR/Cas9 Guide RNA 5′-TGATGAGCTTATCCTCACCA-3′	Trebak Lab (Emrich *et al.*, 2021)	N/A
STIM2 g1 CRISPR/Cas9 Guide RNA 5′-AGATGGTGGAATTGAAGTAG-3′	Trebak Lab (Emrich *et al.*, 2021)	N/A
Recombinant DNA		
LentiCRISPR v2	Addgene	Cat#52961
pCMV R-CEPIA1er	Addgene	Cat#58216
pSpCas9(BB)-2A-GFP (PX458)	Addgene	Cat#48138
pU6-(Bbs1)-mCherry	Addgene	Cat#64324
Software		
Origin 2019b	Origin labs	https://www.originlab.com/
Image J	NIH	https://imagej.nih.gov/ij/
Image Studio Lite	LI-COR	https://www.licor.com/bio/image-studio-lite/download
LAS X	Leica	https://www.leica-microsystems.com/
Bio render	Bio render	https://www.biorender.com

Mice

NOD SCID (NOD.CB17-*Prkdc*^{scid}/J) were also obtained from the Jackson laboratories. The mice were housed in 12:12 hr light dark cycle (22°C to 25°C) in an aseptic environment at The Pennsylvania State University animal facility. The mice were euthanized at the end of the experiment. The tumors and organs were collected for histopathology, protein, and mRNA

analysis. All the mouse experiments were conducted in accordance with The Pennsylvania State University Institutional Animal Care and Research Advisory Committee.

Cell culture and plasmid transfection

HCT116 and DLD1 cells were cultured in McCoy's 5A and RPMI-1640 media respectively and supplemented with 10% FBS and 1X antibiotic-antimycotic (AA) agent. All the cells were kept at 37°C in 5% CO_2 incubator. For the transfection, the cells were cultured at 60-70% confluency. Next day, the cells were transfected with plasmid using Lipofectamine 2000 reagent, according to manufacturer protocol (Invitrogen).

Plasmids, CRISPR/Cas9, and Lentiviral infection

Briefly, at the time of transfection the cells were seeded at 60-70% confluency. The plasmid, and Lipofectamine 2000 were diluted in Opti-MEM and mixed. The mixture was incubated for 5-10 min at room temperature, and then added to the cells cultured in media without AA. The medium of transfected cells was changed to normal medium media with 10% FBS and 1X AA after 4-6 hr. The expression of plasmid was confirmed 24 to 72 hr after transfection.

We generated several clones of STIM1, STIM2 and STIM1/2 DKO knockout in both HCT116 and DLD1 cells using the CRISPR/Cas9 system as described previously (Emrich *et al.*, 2021; Pathak *et al.*, 2020; Yoast *et al*, 2020b).Briefly, highly sequence specific guide RNAs (gRNA) targeting STIM1 and STIM2 were cloned in either pSpCas9(BB)-2A-GFP or pU6-(BbsI)_CBh-Cas9-T2A-mCherry vector. Single gRNA was used to generate STIM1 or STIM2 KO cells. STIM2 KO cells were transfected with STIM1 gRNA to generate STIM1/2 double knockout cells. The cells transfected with gRNA were individually selected for the mChery/GFP markers by FACS (BD FACS Aria SORP) in 96 well plate. To reduce potential off-target effects of the CRISPR/Cas9 system, we generated several independent clones of each knock out cell line.

Transcriptome sequencing (RNA-seq) and analysis

To perform RNA-seq mRNA was isolated from total RNA (minimum 3 µg) from HCT116, STIM1 KO, STIM2 KO, and DKO HCT116 cells using the RNeasy Mini Kit. Short fragment off mRNA was generated using fragmentation buffer (Ambion). The double-stranded cDNA was generated, end-repaired, and ligated to Illumina adapters. These cDNAs were size selected (~250 bp) and PCR amplified. The cDNA library was fed to the Illumina HiSeq 2500 sequencing platform (Berry Genomics) and the expression level of each transcript of a gene was quantified using read counts with HTseq. The genes with identifiers that has zero read counts were removed from each sample, and the biomaRt R package (Durinck *et al*, 2009) was used to convert Ensemble gene identifiers to gene symbols using the January, 2019 archive (http://jan2019.archive.ensembl.org). Identifiers corresponding to multiple gene symbols were removed, as they were lowly expressed genes.

Exploratory analyses were performed after utilizing the VST (variance stabilizing transformation) function in the DESeq2 R package (Love *et al*, 2014) to apply a variance stabilizing transformation to the read count data. The results strongly suggested the presence of a batch effect. Therefore, the design matrix used in the differential expression analysis included batch as a covariate. After applying the voom transformation (Law *et al*, 2014) to the read counts, the limma R package

(Ritchie *et al*, 2015) was used to identify differentially expressed genes based on a q-value threshold of 0.05. The RNA seq data are publicly available in NCBI with BioProject number PRJNA984240.

Gene set enrichment analysis (GSEA)

The gene set enrichment analysis (GSEA) software (Subramanian *et al*, 2005) was used to perform pathway analyses using the limma output. Briefly, genes in the limma output were ordered according to the t test statistic. Then a GSEA pre-ranked analysis was performed using the Hallmark Gene Sets in the Molecular Signatures Database (http://software.broadinstitute.org/gsea/msigdb/index.jsp).

TCGA analysis

RNA-sequencing (RNA-seq) based gene expression data for both tumor and normal samples and clinical data for the combined TCGA colon adenocarcinoma and rectal adenocarcinoma (COADREAD) cohort was downloaded from the Broad Institute's Firehose GDAC (https://gdac.broadinstitute.org/). Gene expression was quantified as log2 (normalized RSEM+1). Somatic gene mutation data was obtained from (Ellrott *et al*, 2018) after restricting to samples in the RNA-seq cohort. Kruskal-Wallis and Wilcoxon rank sum tests and tests were used to compare expression values across groups defined by the clinical and mutation data.

Quantitative Reverse Transcription-PCR (qPCR)

Briefly the cells were washed with cold PBS and RNA was isolated using RNeasy Mini Kit. High-Capacity cDNA Reverse Transcription Kit (Applied Biosystems, Foster City, CA) was used to make cDNA and the cDNA was further used for quantitative real-time PCR using SYBR select master mix (Thermo Scientific, Wilmington, DE, USA) according to the manufacturer protocol. The reactions were run in technical duplicates using Quant Studio 3 system (Applied Biosystems, Foster City, CA). The expression levels of genes were normalized to at least two housekeeping gens, GAPDH or Tubulin (mentioned in the figure legends) using $2^{-\Delta Ct}$ method.

Western blot

As described previously (Pathak *et al.*, 2020), briefly the cells were cultured and after attaining 80-90% confluency the cells were lysed in 100 µl RIPA buffer (Sigma) containing protease and phosphatase Inhibitor. 30-50 µg of the protein was loaded on an 4-12% gel (NuPAGE Bis-Tris precast gels, Life Technologies) and transferred to an activated polyvinylidene difluoride membrane. The membrane was incubated in the Odyssey blocking buffer for 1 hr at room temperature and then incubated overnight at 4°C in primary antibody (1:1000) diluted in Odyssey blocking buffer. Next day, the membrane was washed with 0.1% TBST for 5 min (three times) at room temperature. The blot was incubation in IRDye for 1 hour at room temperature. The IRDyes used are mentioned in the key resource table and they were diluted in Odyssey blocking buffer (IRDye 680RD Goat anti-Mouse at 1:10,000 dilution and IRDye 800CW Donkey anti-Rabbit at 1:5000). The membrane was washed with 0.1% TBST for 5 minutes (three times) at room temperature and imaged in Odyssey CLx Imaging System (LI-COR, NE, USA). Densiometric analysis of the bands on membrane was performed using ImageJ.

Metabolic profiling

The metabolic profiling of HCT116, STIM1 KO, STIM2 KO, and DKO HCT116 cells was performed using LC/MS. The LC/MS analyses were performed using Q Exactive Hybrid Quadrupole Orbitrap mass spectrometer. Which was equipped with an Ion Max source and a HESI II probe coupled to a Dionex UltiMate 3000 UPLC system (Thermo Fisher Scientific, San Jose, CA). The standard calibration mixture was used for external mass calibration and the calibration was performed every 7 days. The HCT116 and HCT116, STIM1 KO, STIM2 KO, and DKO HCT116 cells were collected by scrapping and cell pellets were washed with chilled PBS. Chilled LC/MS grade methanol (600 µl), water (300µl), and chloroform (400 µl) with 10 ng/ml valine-d8 as an internal standard was added to the cell pellet and vortexed for 10 min. The mixture was centrifuged for 10 min at 4°Cat max speed. Carefully, two layers were collected, upper layer for polar and bottom layer for non-polar metabolites. Both the samples were dried on table-top vacuum centrifuge and stored at -80°C. The dried samples were then resuspended in 100 mL water; 1 mL of each sample was injected onto a ZIC-pHILIC 2.1 3 150 mm (5 mm particle size) column (EMD Millipore). Buffer A was 20 mM ammonium carbonate, 0.1% ammonium hydroxide; buffer B was acetonitrile. The chromatographic gradient was run at a flow rate of 0.150 ml/min as follows: 0–20 min.: linear gradient from 80% to 20% B; 20–20.5 min.: linear gradient from 20% to 80% B; 20.5–28 min.: hold at 80% B. The mass spectrometer was operated in full-scan, polarity switching mode with the spray voltage set to 3.0 kV, the heated capillary held at 275°C, and the HESI probe held at 350°C. The sheath gas flow was set to 40 units, the auxiliary gas flow was set to 15 units, and the sweep gas flow was set to 1 unit. The MS data acquisition was performed in a range of 70–1000 m/z, with the resolution set at 70,000, the AGC target at 106, and the maximum injection time at 80 msec. Relative quantitation of polar metabolites was performed with XCalibur QuanBrowser 2.2 (Thermo Fisher Scientific) using a 5 ppm mass tolerance and referencing an in-house library of chemical standards. Relative abundance of metabolites was calculated by normalizing profiling results to cell number.

Mouse tumor xenograft experiments

Mice were anesthetized using isoflurane and after proper sterile preparation of the abdomen, a small (4-8 mm) incision was made by sharp sterile blade over the left upper quadrant of the abdomen. The peritoneal cavity was carefully exposed, and the spleen was located. Further, the spleen was carefully exteriorized on the sterile field around the incision area and 500,000 cells suspended in 50 ul McCoy's (10 or 20% FBS) were then injected into the spleen via a 1 ml insulin syringe. A small bleb was observed while injecting the cells in the spleen confirming that the cells were successfully injected. The injection area was wiped with sterile cotton swab. The spleen was carefully placed back into the peritoneal cavity. Both peritoneal cavity and skin were closed with sterile absorbable suture.

Intracellular Ca^{2+} measurements

Intracellular Ca^{2+} imaging was performed as described previously (Emrich *et al.*, 2021; Yoast *et al.*, 2021). Briefly, the cells were cultured on glass coverslips with 50-60% confluency. Next day the cells were washed with fresh media and incubated at 37°C for 45 min in culture media containing 4 µM Fura-2/acetoxymethyl ester (Molecular Probes, Eugene, OR, USA). Then the

cells were washed and kept in HEPES-buffered saline solution (140 mM NaCl, 1.13 mM $MgCl_2$, 4.7 mM KCl, 2 mM $CaCl_2$, 10 mM D-glucose, and 10 mM HEPES, adjusted to pH 7.4 with NaOH) for at least 10 min before Ca^{2+} measurements were made. Time laps imaging was performed using Leica DMI8 microscope equipped with 40X oil objective. The change in fluorescence of Fura-2 was recorded and analyzed with Leica analysis software X. An ROI was drawn around each cell and 340/380 ratio of each cell was calculated.

Endoplasmic reticulum Ca^{2+} measurements

Previously described method was used to measure endoplasmic reticular Ca^{2+} (ER Ca^{2+}) (Emrich *et al.*, 2021). Briefly, the cells were cultured at 50-60% confluency and transfected with 2-3 µg R-CEPIA$_{ER}$. After 24-48 hrs, the cells were washed with HBSS (HEPES-buffered saline solution (140 mM NaCl, 1.13 mM $MgCl_2$, 4.7 mM KCl, 2 mM $CaCl_2$, 10 mM D-glucose, and 10 mM HEPES, adjusted to pH 7.4 with NaOH)) containing 2 mM $CaCl_2$. The cells were stimulated with 300 µM ATP with no Ca^{2+}. After complete release of ER Ca^{2+} the cells were stimulated with 2 mM Ca^{2+}. The time laps images were acquired using Leica DMI8 microscope equipped with X 20 objective. The images were acquired every 40 sec intervals for 15-20 min. The fluorescent intensity was quantified using LAS X (Leica microsystems) software.

Transmission Electron Microscopy (TEM)

As described previously (Pathak *et al.*, 2020), briefly, the HCT116, STIM1KO, STIM2KO, and DKO HCT116 cells were cultured at 80-90% confluency. The cells were fixed with 1% glutaraldehyde in 0.1 M sodium phosphate buffer (pH 7.3). Then the fixed cells were washed with 100 mM Tris (pH 7.2) and 160 mM sucrose for 30 min. The cells were washed again twice with phosphate buffer (150 mM NaCl, 5 mM KCl, 10 mM Na_3PO_4, pH 7.3) for 30 min, followed by treatment with 1% OsO_4 in 140 mM Na_3PO_4 (pH 7.3) for 1 hr. The cells were washed twice with water and stained with saturated uranyl acetate ($C_4H_6O_6U$) for 1 hr, followed by dehydration in ethanol, and embedded in Epon (Electron Microscopy Sciences, Hatfield, PA). The embedded samples were cut in roughly 60 nm sections and stained with uranyl acetate and lead nitrate. The stained grids were imaged and analyzed using a Philips CM-12 electron microscope (FEI; Eindhoven, The Netherlands) and photographed with a Gatan Erlangshen ES1000W digital camera (Model 785, 4 k 3 2.7 k; Gatan, Pleasanton, CA). Mitochondrial morphology, and mitophagy was analyzed by double-blinded independent observers in at least 10 different micrographs per condition.

Cell proliferation assays

As described previously (Pathak *et al.*, 2020), briefly, the cells were harvested and 3000-5000 cells per well were plated in 96 well plate and kept at 37°C in 5% CO_2 for 4 hr for proper adhesion. The CyQUANT-NF dye was diluted according to the manufacturer protocol and 100 µl/per well was added. After incubating the cells at 37 °C in 5% CO_2 for 1 hr, fluorescence intensity (~485 nm/~530 nm) was measured using FlexStation 3 Multimode Plate Reader (VWR).

Normalized intensity= $(I_t-I_b)\backslash(I_0-I_b)$, I_t= intensity at given time, I_b= background intensity,I_0= intensity at time zero

Spheroid assays

Around 1000 cells were seeded in round bottom untreated 96 well plate with 200 µl media in each well (Nunclon Sphera 96U Well Round Bottom Plate). The plate was spin at 400 rpm for 2 min and kept at 37 °C, 5% CO_2 incubator. Next day the cells were imaged under Leica DMI8 microscope equipped with 10X objective. It was considered as zero time point. Afterward the cells were imaged every 24 hr till the cells form large tight spheroid. The culture media of the spheroid was changed every 2 days. The images were analyzed with Image J.

Colony formation assays

The cells were harvested, and 100 cells were cultured in each well of six well plates. The cells were incubated in 37 °C, 5% CO_2 incubator for 6-7 days. The culture media was changed every two days. Finally, the colonies were stained with Colony fixation-staining solution, glutaraldehyde 6.0% (vol/vol), crystal violet 0.5% (wt/vol) in water. The colonies were imaged under FluorChem M gel imaging system. The number of colonies were counted using image J.

In vitro migration and invasion assays

The migration and invasion were performed as described previously (Pathak *et al.*, 2020). For the gap closure assay, the cell cycle was synchronized by starving the cells for 24 hr. Then 50,000 cells were cultured in ibidi-silicone insert with a defined cell-free gap. After 24 hr the inserts were lifted and the gap between two migrating fronts were measured at 0 hr, 12 hr, and 24 hr using Leica DMi8 equipped with 10X air objective. The area between the two migrating fronts was measured using ImageJ (NIH, Bethesda, USA).

% Gap closure= $(A_0-A_t/A_0)/100$, A_0= aria of gap measured immediately after lifting the insert, A_t= aria of gap measured after indicated time of migration

For the transwell migration assay using, Briefly the cells were starved for 24 hr and 10,000 cells were plated on the FluoroBlok chamber in 200 µl media without FBS. The lower chamber was filled with 200 µl media with 10% FBS, which stimulated the cells to migrate towards the lower chamber. After 8 hr migration the upper face of the membrane was cleaned with cotton swab and lower part was stained with DAPI. The intensity of DAPI was measured using FlexStation 3 Multimode Plate Reader (VWR).

Invasion was measured using the BioCoat™ Tumor Invasion Plate with 8 µm pore size inserts. The upper face of the membrane was coated with growth factor reduced Matrigel. The cells were starved for 24 hr to synchronize the cell cycle and a total of 10,000 cells were plated on the chamber in 200 µl media without FBS. The cells were stimulated to invade towards preconditioned media with 10% FBS. After 24 hr invasion, the upper part of the membrane was cleaned with cotton swab and lower part was stained with DAPI and the intensity of DAPI was measured using FlexStation 3 Multimode Plate Reader (VWR).

%invasion= (Fluorescence of invading cells - Fluorescence of blank chamber)/ Fluorescence of migrating cells - Fluorescence of blank chamber) X100

Extracellular acidification rate (ECAR) and Oxygen consumption rate (OCR)

Seahorse XFp Extracellular Flux Analyzer (Seahorse Bioscience) was used to measure ECAR, and OCR. Briefly, the cells were harvested, and 80,000-90,000 cells per well were cultured in a Seahorse XFp cell culture microplate with complete growth media and incubated in 37 °C, 5% CO_2 incubator for 10-12 hr. The cells were washed with seahorse XF DMEM media (pH 7.4) and incubated in at 37 °C for 30 minutes. Further, the plate with cultured cells was placed in the Seahorse XFp Extracellular Flux Analyzer to record OCR and ECAR. For OCR measurements, oligomycin (1 µM), FCCP (p-trifluoromethoxy carbonyl cyanide phenylhydrazone- 1 µM), and a mixture of Rotenone and antimycin A (Rote/AA- 0.5 µM) were sequentially injected. Similarly, for the ECAR measurements, glucose (10 mM), oligomycin (1 µM), and 2-Deoxy Glucose (50 mM) were sequentially injected into each well at the indicated time points. The final values obtained for ECAR, and OCR, were normalized to protein amount. The data was analyzed by Seahorse XFp Wave software. The results for OCR are reported in pmols/minute/protein, and ECAR in mpH/minute/protein.

Glucose and Lactate measurements

To measure glucose and lactate in media, briefly the cells were harvested, and 100,000 cells were plated in each well of 6 well plate with 2 ml of complete growth media. After 24 hr, 400 µl of the media was taken from one well of 6 well plate and divided into 4 wells of 96 well plate (quadruplicate for each STIM KO clone and respective control). Then the plate was kept in YSI 7100 multichannel biochemistry analyzer (YSI Life Sciences), to measure glucose and lactate levels in the media. Fresh media was used to measure basal level of glucose and lactate. After the measurement, the cells were harvested and number of cells was counted in each well of 6 well plate to make sure that the number of cells is same in each well. This experiment was performed independently at least thrice. Following formula was used to calculate glucose consumption and lactate generation-

Glucose consumption= (Glucose in fresh media-Glucose in the media with cells)/ total protein content

Lactate generation= (Lactate in the media with cells-Lactate in fresh media)/ total protein content

Mitochondrial DNA Measurements

The mitochondrial DNS level was determined as described previously (Johnson *et al.*, 2022). Briefly, the cells were washed, collected, and resuspended in DirectPCR Lysis Reagent (Viagen Biotech) and Proteinase K in 4:1 ratio. Total DNA was isolated using isopropanol and precipitated with 70% ethanol precipitation method and washed three times. A RT- qPCR (50 °C 2-min activation step, a 95 °C 2-min melt step, and 40 cycles of 95°C for 15 s followed by 56 °C for 15 s and 72 °C for 30 s), was performed. Three sets of specific primers for mitochondrial DNA and

two sets for genomic DNA were used. The comparative Ct method was used to quantify mitochondrial DNA copy number.

Mitochondrial burden, Mitochondrial ROS, Cellular ROS, and Mitochondrial membrane potential measurements

To determine mitochondrial burden in the CRC cells, 1,000,000 cells were stained with 100 nM Mito tracker green. The cells were incubated in the complete growth media and kept at 37°C in 5% CO2 for 15 min, and the intensity of staining was measured using LSRII flow cytometer using FACSDiva software (BD Biosciences) and analyzed with FlowJo software (Tree Star).

As previously described (Pathak *et al.*, 2020) the cells were cultured in 6-well plates at 50–60% confluency. To measure cellular ROS and mitochondrial ROS, 1,000,000 cells were stained with CellRox (according to manufacturer protocol) and MitoSOX (2.5 µM in HBSS at 37°C for 45 min in absence of CO_2) respectively. Antimycin (50 µM) was used as a positive control. The cells were washed with warm HBSS before the intensity measurement.

For mitochondrial membrane potential measurement, 1,000,000 cells were harvested and loaded with Tetramethyl rhodamine (TMRM) dye. The cells were stained with 100 nM TMRM dye in complete growth media and kept at 37°C in 5% CO2 for 30 min. Carbonyl cyanide m-chlorophenyl hydrazone (CCCP- 50 µM) was used as a positive control. The cells were washed with warm complete growth media before intensity measurement. The intensity of staining was measured using LSRII flow cytometer using FACSDiva software (BD Biosciences) and analyzed with FlowJo software (Tree Star).

Quantification and statistical analysis

The data are represented as mean ±SEM and analyzed using Origin pro 2019b 64 bit (Origin lab). In the box plot, the box represents 25^{th} to 75^{th} interquartile range, midline in the box represents median and solid square box represents mean data points. To test single variables between two groups Student's t test, paired t-test or Kruskal-Wallis ANOVA was performed (mentioned in the figure legend). One-way ANOVA followed by post hoc Tukey's test was used for comparison between multiple groups versus the control group. A paired t- test was used to compare between two groups. The p value < 0.05 was considered to be significant and is presented as * $p < 0.05$, ** $p < 0.01$, or *** $p < 0.001$.

Contact for Reagent and Resource sharing

All the request and queries about reagents and resources should be directed to and fulfilled by lead contact Dr. Mohamed Trebak (trebakm@pitt.edu).

Acknowledgments

The authors acknowledge Dr. Han Chen from The Pennsylvania State University College of Medicine EM facility for assistance with TEM imaging and Dr. Katherine Aird for generously sharing the YSI analyzer. This study was supported by the National Heart, Lung, and Blood Institute (R01-HL123364, R01-HL097111, and R35-HL150778 to MT), National Institute on Aging (R21-AG050072 to MT), and National Heart, Lung, and Blood Institute (K99 HL163403-01 to TP). GSY and WAK are supported by the Peter and Marshia Carlino Fund for IBD research. We also acknowledge the Flow Cytometry and Cell Sorting, Imaging, Informatics and Data Analysis Core facility (The Pennsylvania State University, College of Medicine and The University of Pittsburgh).

Author contributions

T.P.- Conceptualization, Data curation, Formal analysis, Investigation, Visualization, Methodology, Writing - original draft, Writing - review and editing

J.C.B.- Data curation, Formal analysis, Writing - review and editing

M.T.J.- Data curation, Formal analysis

P.X.- Data curation, Formal analysis,

V.W.- Resources, Software, Formal analysis

W.K.- Resources

G.Y.- Resources, Writing - review and editing

N.H.- Resources, Writing - review and editing

M.T.- Conceptualization, Supervision, Funding acquisition, Methodology, Project administration, Writing - review and editing

Legends to figures

Figure 1. Low STIM2 expression in colorectal cancer is associated with poor patient prognosis

(A, B) TCGA data showing (A) STIM1 and (B) STIM2 mRNA levels in the unmatched tumor and adjacent normal tissue.

(C) Analysis of STIM1 and STIM2 mRNA levels in matched tumor (n=20) and adjacent normal tissue (n=20) of CRC patients by RT-qPCR. The patient samples were obtained from Pennsylvania State University Hershey Medical Center.

(D, E) TCGA data analysis of (D) STIM1 and (E) STIM2 mRNA levels in early (stage I/II) and late (III/IV) stages of CRC progression.

(F, G) Kaplan plot of STIM2 showing survival of (F) colon adenocarcinoma (COAD) and (G) rectal adenocarcinoma (READ) patients.

(H, I) Kaplan plot for STIM1 showing survival of (H) COAD and (I) READ patient.

Kruskal-Wallis ANOVA was performed to test single variables between the two groups. *$p<0.05$, **$p<0.01$, and ***$p<0.001$.

Figure 2. STIM2 loss enhances tumor growth and metastasis in mice

(A) Schematic representation of intrasplenic injection of luciferase tagged HCT116, STIM1 KO #01, STIM2 KO #15, and DKO #22 clones of HCT116 cells. The cells were injected at 5 $X10^5$ cells/mice into the spleen of male NOD-SCID mice.

(B, C) Male NOD-SCID mice injected with luciferase tagged HCT116, STIM1 KO #01, STIM2 KO #15, and DKO #22 clones of HCT116 cells (B) representative image with three mice per group, and (C) quantification of whole-body luminance (Scale bar 2.0 in).

(D, E) Six weeks after intrasplenic injection of HCT116, STIM1 KO #01, STIM2 KO #15, and DKO #22 clones of HCT116 cells, the mice were sacrificed, and the primary tumor at the injection site was imaged, (D) representative image of primary tumors, and (E) quantification of primary tumor weight. (Scale bar 0.5 cm).

(F-I) Post intrasplenic injection of HCT116, STIM1 KO #01, STIM2 KO #15, and DKO #22 clones of HCT116 cells, organs of intrasplenic injected mice were harvested, and luminance was measured (F) representative image of liver, lung, and colon showing metastasis, and quantification of total luminance in (G) liver (Scale bar 1 cm), (H) lung (Scale bar 0.5 cm), and (I) colon (Scale bar 0.5 cm).

(J) Survival of NOD-SCID mice injected with HCT116, STIM1 KO #01, STIM2 KO #15, and STIM DKO #22 clones of HCT116 cells ($p < 0.0003$). ANOVA followed with a post hoc Tukey test to compare between groups. *$p<0.05$, **$p<0.01$ and ***$p<0.001$

Figure 3. Loss of STIM2 enhances CRC proliferation and metastasis

(A, B) Spheroid formation assay showing (A) representative image of spheroid formed by HCT116, and clones of STIM1 KO, STIM2 KO, and DKO in HCT116 cells, (B) quantification of the spheroid area at 0 and 72 hr. (Scale bar 300 μm)

(C) Quantification of the spheroid area of DLD1 and clones of STIM1 KO, STIM2 KO, and DKO in DLD1 cells.

(D, E) Quantification of (D) normalized migration and (E) percent invasion of HCT116 and clones of STIM1 KO, STIM2 KO, and DKO in HCT116 cells using Boyden chamber assay.

(F, G) Quantification of (F) normalized migration and (G) percent invasion of DLD1 and clones of STIM1 KO, STIM2 KO, and DKO in DLD1cells using Boyden chamber assay.

(H, I) RT-qPCR analysis of mRNA levels of (H) MMP16 and (I) MMP14 in HCT116, STIM1 KO, STIM2 KO, and DKO clones of HCT116 cells.

(J, K) RT-qPCR analysis of mRNA levels of (J) MMP16 and (K) MMP14 in DLD1 and clones of STIM1 KO, STIM2 KO, and DKO clones of DLD1 cells.

(L, M) Quantification of (L) normalized migration and (M) percent invasion of HCT116 and clones of Orai1 KO, and Orai TKO in HCT116 cells using Boyden chamber assay.

ANOVA followed with a post hoc Tukey test except for F-M where the paired t-test was used to compare between groups. *$p<0.05$, **$p<0.01$ and ***$p<0.001$

Figure 4. STIM2 regulates mitochondrial biogenesis and metabolism in CRC cells

(A) Heatmap showing significantly increased levels of glycolysis pathway metabolites in HCT116 STIM2 KO #15 and HCT116 DKO #22 compared to HCT116, and HCT116 STIM1 KO #01STIM1 KO #01 cells.

(B) Extracellular acidification rate (ECAR) of HCT116 and clones of STIM1 KO, STIM2 KO, and DKO in HCT116 cells.

(C, D) Measurement of (C) glucose consumption and (D) lactate generation in HCT116 and clones of STIM1 KO, STIM2 KO, and DKO in HCT116 cells.

(E) Oxygen consumption rate (OCR) in HCT116 and STIM1 KO #01, STIM2 KO #15, and DKO #22 clones of HCT116 cells.

(F) Heatmap showing significantly increased levels of citric acid cycle metabolites in HCT116 STIM2 KO #15 and HCT116 DKO #22 compared to HCT116, and HCT116 STIM1 KO #01 cells.

(G, H) Measurement of GLUT1 protein level (G) representative western blot probed with anti-GLUT1 and GAPDH antibody and (H) densitometric analysis of GLUT1 normalized to GAPDH in HCT116 and clones of STIM1 KO, STIM2 KO, and DKO in HCT116 cells.

(I-M) Ultrastructure of mitochondria analyzed by electron microscopy, (I) representative electron micrograph showing mitochondrial structure, measurement of (J) area, (K) circularity, (L) perimeter, and (M) mitochondrial number in HCT116 and STIM1 KO #01, STIM2 KO #15, and DKO #22 colons of HCT116 cells.

(N, O) Flow cytometric analysis of MitoTracker intensity in (N) HCT116 and clones of HCT116 STIM1 KO, HCT116 STIM2 KO, and HCT116 DKO, and (O) DLD1, and clones of DLD1 STIM1 KO, DLD1 STIM2 KO, and DLD1 DKO cells.

(P, Q) RT-qPCR analysis of mitochondrial DNA (mtDNA) in (P) HCT116 and clones of HCT116 STIM1 KO, HCT116 STIM2 KO, and HCT116 DKO, and (Q) DLD1, and clones of DLD1 STIM1 KO, DLD1 STIM2 KO, and DLD1 DKO cells.

Statistical significance was calculated using ANOVA followed by a post hoc Tukey test to compare multiple groups except for C, D, H, P and Q, where the paired t-test was used to compare between groups. *$p<0.05$, **$p<0.01$ and ***$p<0.001$

Figure 5. Loss of STIM2 leads to transcriptional reprogramming of CRC cells

(A-D) Volcano plot showing a comparison of differentially expressed genes between (A) STIM2 KO #15 and HCT116, (B) STIM2 KO #31 and HCT116, (C) DKO #22 and HCT116, and (D) DKO #34 and HCT116. The X-axis represents $\log_2$ fold change and Y axis $-\log_{10}$ (P-value). The threshold in the plot corresponds to P- value <0.05 and log 2-fold change <-1.0 or > 1.0. The significantly downregulated genes are represented in black and upregulated in blue or green.

(E, F) The pathway analysis showing plot between normalized enrichment score and nominal p-value. The positive enrichment score represents upregulated pathway, and negative enrichment shows downregulated pathways in (E) STIM2KO #15 vs. HCT116 and (F) DKO #22 vs. HCT116.

(G, H) GSEA analysis between (G) HCT116 and STIM2 KO #15 and (H) HCT116 and DKO #22 show a positive correlation in the enrichment of hallmark of Myc target version 1 genes.

(I, J) GSEA analysis between (I) HCT116 and STIM2 KO #15 and (J) HCT116 and DKO #22 show a positive correlation in the enrichment of hallmark of Myc target version 2 genes.

(K, L) GSEA analysis between (K) HCT116 and STIM2 KO #15 and (L) HCT116 and DKO #22 show a positive correlation in the enrichment of hallmark of unfolded protein response (UPR) genes.

(M, N) GSEA analysis between (M) HCT116 and STIM2 KO #15 and (N) HCT116 and DKO #22 shows a positive correlation in the enrichment of hallmark of epithelial to mesenchymal transition (EMT) genes.

Figure 6. Loss of STIM2 leads to increased basal ER Ca^{2+}

(A, B) ER Ca^{2+} measurement using genetically encoded R-CEPIA1$_{ER}$. The ER Ca^{2+} depletion was stimulated with 300 µM ATP in 0 mM Ca^{2+} for 10 minutes. The graph represents the mean ± S.E.M. of (A) HCT116, STIM1 KO #01, STIM2 KO #15, and DKO #22 clone of HCT116, and (B) HCT116, STIM1 KO #02, STIM2 KO #31, DKO #34 clones of HCT116 cells.

(C, D) Quantification of (C) Basal ER Ca^{2+}, (D) ER Ca^{2+} depletion rate 3 min post stimulation in 0 Ca^{2+}, HCT116 (n=350), STIM1 KO #01 (n=342), STIM1 KO#02 (n=210), STIM2 KO #15 (n=150), STIM2 KO #31 (n=170). DKO #22 (n=250), and DKO #34 (n=150) clones of HCT116.

(E, F) ER Ca^{2+} measurement using genetically encoded R-CEPIA$_{ER}$. The ER Ca^{2+} depletion was stimulated cells were stimulated with 300 µM ATP in 0 mM Ca^{2+} for 10 minutes. The graph represents the mean ± S.E.M. of (E) DLD1, STIM1 KO #03, STIM2 KO #04, and DKO #01 clone of DLD1, and (F) DLD1, STIM1 KO #05, STIM2 KO #09, DKO #07 clones of DLD1 cells.

(G, H) Quantification of (G) Basal ER Ca^{2+}, (H) ER Ca^{2+} depletion rate 3 min post stimulation in 0 Ca^{2+}, in DLD1 (n=140), STIM1 KO #03 (n=54), STIM1 KO#05 (n=85), STIM2 KO #04 (n=50), STIM2 KO #09 (n=40). DKO #01 (n=35), and DKO #07 (n=40) clones of DLD1.

(I-K) RT-qPCR analysis of mRNA levels of (I) SERCA1, (J) SERCA2, and (K) SERCA3 in HCT116, STIM1 KO, STIM2 KO, and DKO in HCT116 cells.

(L-O) Measurement of SERCA2 protein level by probing the western blots with anti-SERCA2 and GAPDH antibody (L and N) representative blot probed and (M, and O) densitometric analysis of SERCA2 normalized to GAPDH in HCT116 and clones of STIM1 KO, STIM2 KO, and DKO in HCT116 cells.

(P, Q) Measurement of SERCA2 protein level by probing the western blots with anti-SERCA2 and GAPDH antibody (P) representative blot, and (Q) densitometric analysis of SERCA2 normalized to GAPDH in DLD1 and clones of STIM1 KO, STIM2 KO, and DKO in DLD1 cells.

All experiments were performed ≥three times with similar results. Statistical significance was calculated using one-way ANOVA followed by a post hoc Tukey test except for I-Q, where the paired t-test was used to compare between groups. *$p<0.05$, **$p<0.01$, ***$p<0.001$

Figure 7. STIM2 deletion promotes cMyc stabilization and increases PPARɣ levels

(A) Representative western blot probed with anti- phospho-cMyc, cMyc, phospho-ERK, ERK, and GAPDH.

(B, C) Densitometric analysis of (B) phospho-cMyc and (C) phospho-ERK in HCT116, STIM1 KO #01, STIM2 KO #15, DKO #22 clone in HCT116 and DLD1, STIM1 KO #03, STIM2 KO #04, DKO #01 clones in DLD1 cells.

(D-G) PGC1α levels determined by western blot (D, F) blot probed with anti- PGC1α and GAPDH antibody and (E, G) densitometric analysis of PGC1α levels in HCT116, DLD1, STIM1 KO, STIM2 KO, and DKO clones of HCT116 and DLD1 cells.

(H, I) PPARɣ levels quantified using (H) western blot probed with anti-PPARɣ and GAPDH antibody, and (I) densitometric analysis of PPARɣ levels in HCT116, DLD1, STIM1 KO, STIM2 KO, and DKO clones of HCT116 and DLD1 cells.

All experiments were performed ≥three times with similar results. Statistical significance was calculated using paired t-test. *p<0.05, **p<0.01, ***p<0.001

Figure 8. Loss of STIM2 activates the ATF4-dependent ER stress pathway

(A, B) Quantification of BiP protein levels using (A) western blot probed with anti-Bip and GAPDH antibody, and (B) densitometric analysis in HCT116, DLD1, STIM1 KO, STIM2 KO, and DKO clones of HCT116 and DLD1cells.

(C, D) Quantification of ATF4 protein levels using (C) western blot probed with anti-ATF4 and GAPDH antibody, and (D) densitometric analysis in HCT116, STIM1 KO, STIM2 KO, and DKO clones of HCT116.

(E, F) Quantification of IRE1α protein levels using (E) western blot probed with anti- IRE1α and GAPDH antibody, and (F) densitometric analysis in HCT116, STIM1 KO, STIM2 KO, and DKO clones of HCT116.

(G, H) Quantification of ATF6 protein levels using (G) western blot probed with anti- ATF6 and GAPDH antibody, and (H) densitometric analysis in HCT116, STIM1 KO, STIM2 KO, and DKO clones of HCT116.

(I, J) Quantification of phospho-eIF2α protein levels using (I) western blot probed with anti-phospho-eIF2α, eIF2α, and GAPDH antibody, and (J) densitometric analysis in HCT116, STIM1 KO, STIM2 KO, and DKO clones of HCT116.

(K, L) Quantification of phospho-PERK protein levels using (K) western blot probed with anti-phospho-PERK, PERK, and GAPDH antibody, and (L) densitometric analysis in HCT116, STIM1 KO, STIM2 KO, and DKO clones of HCT116.

All experiments were performed ≥three times with similar results. Statistical significance was calculated using paired t-test . *p<0.05, **p<0.01, ***p<0.001

Legends to supplementary figures

Supplementary Figure 1. Loss of STIM2 is associated with poor prognosis of CRC patients

(A, B) TCGA data showing (A) STIM1 and (B) STIM2 mRNA levels in normal and TP53 mutated conditions.

(C, D) TCGA data showing (C) STIM1 and (D) STIM2 mRNA levels in normal and PI3KCA mutated conditions.

(E, F) TCGA data showing (E) STIM1 and (F) STIM2 mRNA levels in normal and KRAS mutated conditions.

(G, H) TCGA data showing (G) STIM1 and (H) STIM2 mRNA levels in normal and BRAF and NRAS mutated conditions.

(I-K) TCGA data showing (I) Orai1, (J) Orai2, and (K) Orai3 mRNA levels in the tumor and adjacent normal tissue.

(L-N) Kaplan plot for (L) Orai1, (M) Orai2, and (N) Orai3 showing survival of colon adenocarcinoma (COAD) patient.

Kruskal-Wallis ANOVA was performed to test single variables between the two groups. *$p<0.05$, **$p<0.01$, and ***$p<0.001$.

Supplementary Figure 2. Loss of STIM2 leads to a partial reduction in SOCE in CRC cells

(A-C) Measurement of STIM1 and STIM2 protein level (A) representative western blot probed with anti-STIM1, STIM2, and GAPDH antibody, and densitometric analysis of (B) STIM1, and (C) STIM2 normalized to GAPDH in HCT116 and STIM1 KO, STIM2 KO, and DKO clones of HCT116 cells.

(D-F) Measurement of STIM1 and STIM2 protein level (D) representative western blot probed with anti-STIM1, STIM2, and GAPDH antibody, and densitometric analysis of (E) STIM1, and (F) STIM2 normalized to GAPDH in DLD1 and STIM1 KO, STIM2 KO, and DKO clones of DLD1 cells.

(G) Cytosolic Ca^{2+} measurements with Fura-2 in response to 100 µM ATP applied first in nominally Ca^{2+}-free external solution and subsequently with 2 mM external Ca^{2+}. The traces are represented as mean ± S.E.M

(H) Quantification of peak SOCE after addition of 2 mM Ca^{2+} in HCT116 (n = 82) and STIM1 KO #01 (n=34), STIM1 KO #02 (n=43), STIM2 KO #15 (n=23), STIM2 KO #31 (n=24), DKO #22 (n=20) and DKO #34 (n=30) clones of HCT116 cells.

(I) Fura-2 Ca^{2+} measurements upon store depletion with 100 µM ATP in 0 mM Ca^{2+} and subsequent addition of 2 mM Ca^{2+}.

(J) Quantification of peak SOCE after addition of 2 mM Ca^{2+} in DLD1(n = 90) and STIM1 KO #03 (n=90), STIM1 KO #05 (n=90), STIM2 KO #04 (n=90), STIM2 KO #09 (n=90), DKO #01 (n=90) and DKO #07 (n=90) clones of DLD1 cells.

(K-M) Post intrasplenic injection of HCT116, STIM1 KO #01, STIM2 KO #15, and DKO #22 cells into the NOD SCID mice, the organs were harvested, and luminance was measured (K) representative image of kidney and heart, and quantification of total luminance in (L) kidney, and (M) heart. (Scale bar 0.5 cm)

All experiments were performed ≥three times with similar results. Statistical significance was calculated using paired t-test. *p<0.05, **p<0.01, ***p<0.001

Supplementary Figure 3. Loss of STIM2 promotes migration of CRC cells

(A, B) The proliferation assay was performed by staining (A) HCT116 and STIM1 KO, STIM2 KO, and DKO clones of HCT116 cells, and (B) DLD1 and STIM1 KO, STIM2 KO, and DKO clones of DLD1 cells using CyQUANT dye.

(C, D) Representative bright field image of (C) colony formation assay and (D) quantification of the number of colonies formed by HCT116 and STIM1 KO, STIM2 KO, and DKO clones of HCT116 cells.

(E, F) In vitro migration assay performed using HCT116 and STIM1 KO, STIM2 KO, and DKO clones of HCT116 cells. (E) The image showing gap closure at 0 and 24 hr post culture, and (F) quantification of percent gap closure. Scale bar 1 mm.

(G, H) In vitro migration assay performed using DLD1 and STIM1 KO, STIM2 KO, and DKO clones of DLD1 cells. (G) The image showing gap closure at 0 and 24 hr post culture, and (H) quantification of percent gap closure. Scale bar 1 mm.

(I-K) RT-qPCR analysis of mRNA levels of (I) Orai1, (J) Orai2, and (K) Orai3 in HCT116 and Orai1 KO and Orai TKO clones of HCT116.

(L, M) Fura-2 Ca^{2+} measurements upon store depletion with 100 µM ATP in 0 mM Ca^{2+} and subsequent addition of 2 mM Ca^{2+}. (L) The trace represents mean± S.E.M. (M) Quantification of peak SOCE after addition of 2 mM Ca^{2+} in HCT116 (n = 41) and Orai1 KO #05 (n=58), Orai1 KO #15 (n=68), TKO #01 (n=30), and TKO #10 (n=71) clones of HCT116 cells.

(N) Representative image of in vitro migration assay performed using HCT116 and Orai1 KO, and Orai TKO clones of HCT116 cells. (Scale bar 1 mm)

(O, P) The quantification of percent gap closure by (O) HCT116 and Orai1 clones of HCT116 and (P) HCT116 and TKO clones of HCT116.

All experiments were performed ≥three times with similar results. Statistical significance was calculated using paired t-Test was used to compare between groups. *p<0.05, **p<0.01, ***p<0.001

Supplementary Figure 4. Loss of STIM2 causes metabolic rewiring of CRC cells

(A-E) The levels of polar metabolites were measured using whole-cell metabolomics. Heatmap represents comparison of polar metabolites levels between (A) HCT116 and STIM1 KO #01 clone, (B) HCT116 and STIM2 KO #15 clone (C) HCT116 and DKO #22 clone, (D) STIM2 KO #15 and STIM1 KO #01 clone of HCT116, and (E) DKO #22 and STIM1 KO #01 clone of HCT116.

Supplementary Figure 5. STIM2 regulates metabolism of CRC cells

(A) Measurement of ECAR in DLD1, STIM1KO #03, STIM2KO #04, and DKO #01 clones of HCT116.

(B) ECAR measurement in HCT116, and Orai1 KO and TKO clones of HCT116.

(C, D) GLUT1 protein level measurement using western blot. (C) Representative western blot probed with anti- GLUT1 and GAPDH antibody, and (D) densitometric quantification of GLUT1 levels in DLD1, STIM1 KO, STIM2 KO, and DKO clones of DLD1.

(E, F) The measurement of GLUT1 protein levels using (E) western blot and (F) densitometric analysis in HCT116 and Orai1 KO and TKO clones of HCT116.

(G, H) OCR measurement in (G) DLD1 and STIM1 KO, STIM2 KO and DKO, clones of DLD1cells, and (H) HCT116 and Orai1 KO, and TKO clones of HCT116.

(I) Quantification of components of electron chain complex components. The representative western blot probed with a cocktail of antibodies against NADH dehydrogenase [ubiquinone] 1 b subcomplex subunit 8 (NDUFB8, Complex-I), Succinate dehydrogenase [ubiquinone] iron-sulfur subunit (SDHB, Complex-II), Cytochrome b-c1 complex subunit 2 (UQCRC2, Complex-III), Cytochrome c oxidase subunit 1 (MTCO1, Complex IV), and ATP synthase subunit an (ATP5A, Complex-V).

(J-N) Densitometric analysis of protein levels of (J) NDUFB8, (K) SDHB, (L) UQCRC2, (M) MTCO1, and (N) ATP5A in HCT116 and STIM1 KO, STIM2 KO, and DKO clones of HCT116.

(O) Measurement of mitochondrial ROS in HCT116 and STIM1 KO, STIM2 KO, and DKO clones of HCT116 using flow cytometry. The cells were stained with MitoSOX and MitoTracker. The graph represents MitoSOX intensity normalized to MitoTracker.

(P) Cytosolic ROS measurement in HCT116 and STIM1 KO, STIM2 KO, and DKO clones of HCT116 using flow cytometry. The cells were stained with CellROX and the graph represents CellROX intensity.

(Q) Mitochondrial membrane potential measurement in HCT116 and STIM1 KO, STIM2 KO, and DKO clones of HCT116 using flow cytometry. The cells were stained with TMRE and MitoTracker. The graph represents TMRE intensity normalized to MitoTracker.

(R) Heatmap showing levels of pentose phosphate pathway metabolites in HCT116 and STIM1 KO, STIM2 KO, and DKO clones of HCT116.

All the experiments were performed ≥three times with similar results. The statistical significance was calculated using paired t-Test. *p<0.05, **p<0.01, ***p<0.001

Supplementary Figure 6. Loss of STIM2 induces ribosome biogenesis

(A, B) Venn diagram showing common and uniquely expressed genes between (A) HCT116, and STIM1 KO #01, STIM2 KO#15, DKO #22 clones of HCT116, and (B) HCT116 and STIM1 KO #02, STIM2 KO #31, and DKO #34 clones of HCT116.

(C, D) Volcano plot showing differentially expressed genes between (C) HCT116 and STIM1 KO #01 clone of HCT116 and (D) HCT116 and STIM1 KO #02 clone of HCT116.

(E-J) The Kyoto Encyclopedia of Genes and Genomes (KEGG) analysis showing enrichment of pathways based on molecular interactions. The plot shows the top 20 pathways that are significantly enriched in (E) STIM1 KO #01, (F) STIM1 KO #02, (G) STIM2 KO #15, (H) STIM2 KO #31, (I) DKO #22, and (J) DKO #34 clones of HCT116 compared to wildtype HCT116 cells.

(K-P) The Gene ontology (GO) analysis showing enrichment based on biological process (BP). The plot showing the top 20 pathways that are significantly enriched in (K) STIM1 KO #01, (L) STIM1 KO #02, (M) STIM2 KO #15, (N) STIM2 KO #31, (O) DKO #22, and (P) DKO #34 clones of HCT116 compared to wildtype HCT116 cells.

Supplementary Figure 7. Loss of STIM2 induces expression of EMT and UPR hallmark genes

(A, C) Heatmap showing differential expression of genes of hallmark (A) EMT, (B) Myc target version 2, and (C) unfolded protein response (UPR) between HCT116 and STIM2 KO #15 clones of HCT116 cells.

Supplementary Figure 8. Loss of Orai does not affect ER Ca^{2+} levels in HCT116 cells

(A, B) ER Ca^{2+} measurement using genetically encoded R-CEPIA$_{ER}$. The ER Ca^{2+} depletion was stimulated with 300 μM ATP in 0 mM Ca^{2+} for 10 minutes, followed by the addition of 2 mM Ca^{2+}. (A) The graph represents the mean ± S.E.M. of R-CEPIA$_{ER}$ fluorescence in HCT116 and, HEK293 cells and (B) Percentage of normalized F/F_0 value of R-CEPIA$_{ER}$ in HCT116 and HEK293 cells. The traces are represented as mean ± S.E.M

(C-F) Quantification of (C) Basal ER Ca^{2+}, (D) ER Ca^{2+} depletion rate 3 min post stimulation in 0 Ca^{2+}, (E) maximal ER Ca^{2+} at 15 min in 2 mM Ca^{2+}, and (F) ER Ca^{2+} refilling rate at 12.5 min in 2 mM Ca^{2+} in HCT116 (n=150), and HEK293 (n=152).

(G, H) ER Ca^{2+} measurement using genetically encoded R-CEPIA$_{ER}$. The ER Ca^{2+} depletion was stimulated with 300 µM ATP in 0 mM Ca^{2+} for 10 minutes, followed by the addition of 2 mM Ca^{2+}. The graph represents the mean ± S.E.M. of (G) HCT116, Orai1 KO #05, Orai1 KO #15, TKO #01, and TKO #10 clone of HCT116, and (H) Percentage of normalized F/F_0 value of R-CEPIA$_{ER}$ in HCT116, Orai1 KO #05, Orai1 KO #15, TKO #01, and TKO #10 clone of HCT116 cells. The traces are represented as mean ± S.E.M

(I-L) Quantification of (I) Basal ER Ca^{2+}, (J) ER Ca^{2+} depletion rate 3 min post stimulation in 0 Ca^{2+}, (K) ER Ca^{2+} refilling rate at 12.5 min in 2 mM Ca^{2+}, and (L) maximal ER Ca^{2+} at 15 min in 2 mM Ca^{2+} in in HCT116 (n=150), Orai1 KO #05 (n=124), Orai1 KO #15 (n=95), TKO #01 (n=80), TKO #10 (n=93).

(M-O) Measurement of IP3R1 and IP3R3 protein level by probing the western blots with anti-IP3R1, anti-IP3R3 and GAPDH antibody (M) representative blot, (N) densitometric analysis of IP3R1 normalized to GAPDH and (O) densitometric analysis of IP3R3 normalized to GAPDH in HCT116 and clones of STIM1 KO, STIM2 KO, and DKO in HCT116 cells.

(P-S) Measurement of IP3R1, IP3R2 and IP3R3 protein level by probing the western blots with anti-IP3R1, anti-IP3R2, anti-IP3R3 and GAPDH antibody (P) representative blot, (Q) densitometric analysis of IP3R1, (R) IP3R2, and (S) IP3R3 normalized to GAPDH in DLD1 and clones of STIM1 KO, STIM2 KO, and DKO in DLD1 cells.

ER Ca^{2+} measurements from HCT116, HEK293, Orai1 KO, and Orai TKO were performed together. All the experiments were performed ≥three times with similar results. The statistical significance was calculated using paired t-test. *$p<0.05$, **$p<0.01$, ***$p<0.001$

Supplementary figure 9. Deletion of Orai did not affect cMyc, ERK, and PPARɣ levels

(A, B) Quantification cMyc levels using (A) western blot probed with anti- phospho-cMyc, cMyc, and GAPDH and (B) densitometric analysis of phospho-cMyc in HCT116, Orai1 KO, and TKO clones of HCT116.

(C, D) Quantification of phospho-ERK levels using (C) western blot probed with anti- phospho-ERK, ERK, and GAPDH and (D) densitometric analysis of phospho-ERK in HCT116, Orai1 KO, and TKO clones of HCT116.

(E-F) TCGA analysis using ULCAN showing cMyc mRNA levels in (E) normal and primary tumors, (F) normal and individual stages of CRC growth.

(G, H) Correlation of cMyc mRNA expression with STIM1 and STIM2 mRNA expression in Colorectal Adenocarcinoma samples from TCGA (n=524, Pan Cancer Atlas). Data obtained using cBioPortal and expressed as z-scores relative to all samples (log RNA Seq V2 RSEM).

(I-L) PGC1α and PPARɣ levels quantified using western blot probed with (I) anti- PGC1α, (K) anti-PPARɣ and GAPDH antibody, and densitometric analysis of (J) PGC1α, and (L) PPARɣ levels in HCT116, Orai1 KO, and TKO clones of HCT116.

All experiments were performed ≥three times with similar results. Statistical significance was calculated using paired t-test. *p<0.05, **p<0.01, ***p<0.001

Supplementary figure 10. Loss of Orai did not activate the ER stress response in CRC cells

(A, B) Quantification of ATF4 levels using (A) western blot probed with anti-ATF4 and GAPDH antibody, and (B) densitometric analysis in DLD1, STIM1 KO, STIM2 KO, and DKO clones of DLD1.

(C, D) Quantification of IRE1α levels using (C) western blot probed with anti-IRE1α and GAPDH antibody, and (D) densitometric analysis in DLD1, STIM1 KO, STIM2 KO, and DKO clones of DLD1.

(E, F) Quantification of ATF6 levels using (E) western blot probed with anti-ATF6 and GAPDH antibody, and (F) densitometric analysis in DLD1, STIM1 KO, STIM2 KO, and DKO clones of DLD1.

(G, H) Quantification of BiP levels using (G) western blot probed with anti-Bip and GAPDH antibody, and (H) densitometric analysis in HCT116, Orai1 KO, and TKO clones of HCT116.

(I, J) Quantification of ATF4 levels using (I) western blot probed with anti-ATF4 and GAPDH antibody, and (J) densitometric analysis in HCT116, Orai1 KO, and TKO clones of HCT116.

(K, L) Quantification of IRE1α levels using (K) western blot probed with anti- IRE1α and GAPDH antibody, and (L) densitometric analysis in HCT116, Orai1 KO, and TKO clones of HCT116.

(M, N) Quantification of ATF6 levels using (M) western blot probed with anti- ATF6 and GAPDH antibody, and (N) densitometric analysis in HCT116, Orai1 KO, and TKO clones of HCT116.

All experiments were performed ≥three times with similar results. Statistical significance was calculated using paired t-test. *p<0.05, **p<0.01, ***p<0.001

References

Arabi A, Wu S, Ridderstråle K, Bierhoff H, Shiue C, Fatyol K, Fahlén S, Hydbring P, Söderberg O, Grummt I *et al* (2005) c-Myc associates with ribosomal DNA and activates RNA polymerase I transcription. *Nat Cell Biol* 7: 303-310

Barna M, Pusic A, Zollo O, Costa M, Kondrashov N, Rego E, Rao PH, Ruggero D (2008) Suppression of Myc oncogenic activity by ribosomal protein haploinsufficiency. *Nature* 456: 971-975

Ben-Kasus Nissim T, Zhang X, Elazar A, Roy S, Stolwijk JA, Zhou Y, Motiani RK, Gueguinou M, Hempel N, Hershfinkel M *et al* (2017) Mitochondria control store-operated Ca(2+) entry through Na(+) and redox signals. *The EMBO journal* 36: 797-815

Blancafort P, Chen EI, Gonzalez B, Bergquist S, Zijlstra A, Guthy D, Brachat A, Brakenhoff RH, Quigley JP, Erdmann D *et al* (2005) Genetic reprogramming of tumor cells by zinc finger transcription factors. *Proceedings of the National Academy of Sciences* 102: 11716-11721

Bost F, Kaminski L (2019) The metabolic modulator PGC-1α in cancer. *Am J Cancer Res* 9: 198-211

Brandman O, Liou J, Park WS, Meyer T (2007a) STIM2 is a feedback regulator that stabilizes basal cytosolic and endoplasmic reticulum Ca2+ levels. *Cell* 131: 1327-1339

Brandman O, Liou J, Park WS, Meyer T (2007b) STIM2 is a feedback regulator that stabilizes basal cytosolic and endoplasmic reticulum Ca2+ levels. *Cell* 131: 1327-1339

Bustos G, Cruz P, Lovy A, Cárdenas C (2017) Endoplasmic Reticulum-Mitochondria Calcium Communication and the Regulation of Mitochondrial Metabolism in Cancer: A Novel Potential Target. *Front Oncol* 7: 199

Chan JC, Hannan KM, Riddell K, Ng PY, Peck A, Lee RS, Hung S, Astle MV, Bywater M, Wall M *et al* (2011) AKT Promotes rRNA Synthesis and Cooperates with c-MYC to Stimulate Ribosome Biogenesis in Cancer. *Science Signaling* 4: ra56-ra56

Chandrashekar DS, Bashel B, Balasubramanya SAH, Creighton CJ, Ponce-Rodriguez I, Chakravarthi BVSK, Varambally S (2017) UALCAN: A Portal for Facilitating Tumor Subgroup Gene Expression and Survival Analyses. *Neoplasia* 19: 649-658

Chen X, Cubillos-Ruiz JR (2021) Endoplasmic reticulum stress signals in the tumour and its microenvironment. *Nature Reviews Cancer* 21: 71-88

Collins SR, Meyer T (2011) Evolutionary origins of STIM1 and STIM2 within ancient Ca2+ signaling systems. *Trends Cell Biol* 21: 202-211

Corazzari M, Gagliardi M, Fimia GM, Piacentini M (2017) Endoplasmic Reticulum Stress, Unfolded Protein Response, and Cancer Cell Fate. *Frontiers in Oncology* 7

Costa-Mattioli M, Walter P (2020) The integrated stress response: From mechanism to disease. *Science* 368: eaat5314

Deniaud A, Sharaf el dein O, Maillier E, Poncet D, Kroemer G, Lemaire C, Brenner C (2008) Endoplasmic reticulum stress induces calcium-dependent permeability transition, mitochondrial outer membrane permeabilization and apoptosis. *Oncogene* 27: 285-299

Destefanis F, Manara V, Bellosta P (2020) Myc as a Regulator of Ribosome Biogenesis and Cell Competition: A Link to Cancer. *Int J Mol Sci* 21

Dunne PD, Alderdice M, O'Reilly PG, Roddy AC, McCorry AMB, Richman S, Maughan T, McDade SS, Johnston PG, Longley DB *et al* (2017) Cancer-cell intrinsic gene expression signatures overcome intratumoural heterogeneity bias in colorectal cancer patient classification. *Nat Commun* 8: 15657-15657

Durinck S, Spellman PT, Birney E, Huber W (2009) Mapping identifiers for the integration of genomic datasets with the R/Bioconductor package biomaRt. *Nat Protoc* 4: 1184-1191

Ellrott K, Bailey MH, Saksena G, Covington KR, Kandoth C, Stewart C, Hess J, Ma S, Chiotti KE, McLellan M *et al* (2018) Scalable Open Science Approach for Mutation Calling of Tumor Exomes Using Multiple Genomic Pipelines. *Cell Systems* 6: 271-281.e277

Emrich SM, Yoast RE, Trebak M (2022) Physiological Functions of CRAC Channels. *Annu Rev Physiol* 84: 355-379

Emrich SM, Yoast RE, Xin P, Arige V, Wagner LE, Hempel N, Gill DL, Sneyd J, Yule DI, Trebak M (2021) Omnitemporal choreographies of all five STIM/Orai and IP(3)Rs underlie the complexity of mammalian Ca(2+) signaling. *Cell Rep* 34: 108760

Emrich SM, Yoast RE, Xin P, Zhang X, Pathak T, Nwokonko R, Gueguinou MF, Subedi KP, Zhou Y, Ambudkar IS *et al* (2019) Cross-talk between N-terminal and C-terminal domains in stromal interaction molecule 2 (STIM2) determines enhanced STIM2 sensitivity. *J Biol Chem* 294: 6318-6332

Emrich SM, Yoast RE, Zhang X, Fike AJ, Wang YH, Bricker KN, Tao AY, Xin P, Walter V, Johnson MT *et al* (2023) Orai3 and Orai1 mediate CRAC channel function and metabolic reprogramming in B cells. *Elife* 12

Faris P, Rumolo A, Tapella L, Tanzi M, Metallo A, Conca F, Negri S, Lefkimmiatis K, Pedrazzoli P, Lim D *et al* (2022) Store-Operated Ca2+ Entry Is Up-Regulated in Tumour-Infiltrating Lymphocytes from Metastatic Colorectal Cancer Patients. *Cancers* 14: 3312

Gao P, Tchernyshyov I, Chang T-C, Lee Y-S, Kita K, Ochi T, Zeller KI, De Marzo AM, Van Eyk JE, Mendell JT *et al* (2009) c-Myc suppression of miR-23a/b enhances mitochondrial glutaminase expression and glutamine metabolism. *Nature* 458: 762-765

Gao W, Xu Y, Chen T, Du Z, Liu X, Hu Z, Wei D, Gao C, Zhang W, Li Q (2019) Targeting oxidative pentose phosphate pathway prevents recurrence in mutant Kras colorectal carcinomas. *PLOS Biology* 17: e3000425

Gonzalez-Cobos JC, Zhang X, Zhang W, Ruhle B, Motiani RK, Schindl R, Muik M, Spinelli AM, Bisaillon JM, Shinde AV *et al* (2013) Store-independent Orai1/3 channels activated by intracrine leukotriene C4: role in neointimal hyperplasia. *Circulation research* 112: 1013-1025

Grandori C, Gomez-Roman N, Felton-Edkins ZA, Ngouenet C, Galloway DA, Eisenman RN, White RJ (2005) c-Myc binds to human ribosomal DNA and stimulates transcription of rRNA genes by RNA polymerase I. *Nat Cell Biol* 7: 311-318

Guinney J, Dienstmann R, Wang X, de Reyniès A, Schlicker A, Soneson C, Marisa L, Roepman P, Nyamundanda G, Angelino P *et al* (2015) The consensus molecular subtypes of colorectal cancer. *Nat Med* 21: 1350-1356

Hart LS, Cunningham JT, Datta T, Dey S, Tameire F, Lehman SL, Qiu B, Zhang H, Cerniglia G, Bi M *et al* (2012) ER stress-mediated autophagy promotes Myc-dependent transformation and tumor growth. *J Clin Invest* 122: 4621-4634

Hetz C (2012) The unfolded protein response: controlling cell fate decisions under ER stress and beyond. *Nature Reviews Molecular Cell Biology* 13: 89-102

Iritani BM, Eisenman RN (1999) c-Myc enhances protein synthesis and cell size during B lymphocyte development. *Proceedings of the National Academy of Sciences* 96: 13180-13185

Isella C, Brundu F, Bellomo SE, Galimi F, Zanella E, Porporato R, Petti C, Fiori A, Orzan F, Senetta R *et al* (2017) Selective analysis of cancer-cell intrinsic transcriptional traits defines novel clinically relevant subtypes of colorectal cancer. *Nat Commun* 8: 15107-15107

Jiang P, Du W, Wu M (2014) Regulation of the pentose phosphate pathway in cancer. *Protein & Cell* 5: 592-602

Johnson MT, Xin P, Benson JC, Pathak T, Walter V, Emrich SM, Yoast RE, Zhang X, Cao G, Panettieri RA *et al* (2022) STIM1 is a core trigger of airway smooth muscle remodeling and hyperresponsiveness in asthma. *Proceedings of the National Academy of Sciences* 119: e2114557118

Jones CA, Hazlehurst LA (2021) Role of Calcium Homeostasis in Modulating EMT in Cancer. *Biomedicines* 9

Kaufmann U, Kahlfuss S, Yang J, Ivanova E, Koralov SB, Feske S Calcium Signaling Controls Pathogenic Th17 Cell-Mediated Inflammation by Regulating Mitochondrial Function. *Cell Metabolism*

Khan HY, Mpilla GB, Sexton R, Viswanadha S, Penmetsa KV, Aboukameel A, Diab M, Kamgar M, Al-Hallak MN, Szlaczky M *et al* (2020) Calcium Release-Activated Calcium (CRAC) Channel Inhibition Suppresses Pancreatic Ductal Adenocarcinoma Cell Proliferation and Patient-Derived Tumor Growth. *Cancers (Basel)* 12

Krebs J, Agellon LB, Michalak M (2015) Ca2+ homeostasis and endoplasmic reticulum (ER) stress: An integrated view of calcium signaling. *Biochemical and Biophysical Research Communications* 460: 114-121

Krishnan V, Ali S, Gonzales AL, Thakore P, Griffin CS, Yamasaki E, Alvarado MG, Johnson MT, Trebak M, Earley S (2022) STIM1-dependent peripheral coupling governs the contractility of vascular smooth muscle cells. *Elife* 11

Law CW, Chen Y, Shi W, Smyth GK (2014) voom: precision weights unlock linear model analysis tools for RNA-seq read counts. *Genome Biology* 15: R29

Lewis RS (2020) Store-Operated Calcium Channels: From Function to Structure and Back Again. *Cold Spring Harb Perspect Biol* 12

Li F, Wang Y, Zeller KI, Potter JJ, Wonsey DR, O'Donnell KA, Kim J-w, Yustein JT, Lee LA, Dang CV (2005) Myc Stimulates Nuclearly Encoded Mitochondrial Genes and Mitochondrial Biogenesis. *Molecular and Cellular Biology* 25: 6225-6234

Lin J, Xia L, Oyang L, Liang J, Tan S, Wu N, Yi P, Pan Q, Rao S, Han Y *et al* (2022) The POU2F1-ALDOA axis promotes the proliferation and chemoresistance of colon cancer cells by enhancing glycolysis and the pentose phosphate pathway activity. *Oncogene* 41: 1024-1039

Liou J, Kim ML, Heo WD, Jones JT, Myers JW, Ferrell JE, Meyer T (2005) STIM is a Ca2+ sensor essential for Ca2+-store-depletion-triggered Ca2+ influx. *Curr Biol* 15: 1235-1241

Love MI, Huber W, Anders S (2014) Moderated estimation of fold change and dispersion for RNA-seq data with DESeq2. *Genome Biol* 15: 550

Marampon F, Ciccarelli C, Zani BM (2006) Down-regulation of c-Myc following MEK/ERK inhibition halts the expression of malignant phenotype in rhabdomyosarcoma and in non muscle-derived human tumors. *Molecular Cancer* 5: 31

Marchi S, Pinton P (2016) Alterations of calcium homeostasis in cancer cells. *Current Opinion in Pharmacology* 29: 1-6

Maus M, Cuk M, Patel B, Lian J, Ouimet M, Kaufmann U, Yang J, Horvath R, Hornig-Do HT, Chrzanowska-Lightowlers ZM *et al* (2017) Store-Operated Ca(2+) Entry Controls Induction of Lipolysis and the Transcriptional Reprogramming to Lipid Metabolism. *Cell Metab* 25: 698-712

Mekahli D, Bultynck G, Parys JB, De Smedt H, Missiaen L (2011) Endoplasmic-reticulum calcium depletion and disease. *Cold Spring Harb Perspect Biol* 3

Meyer N, Penn LZ (2008) Reflecting on 25 years with MYC. *Nature Reviews Cancer* 8: 976-990

Mo P, Yang S (2018) The store-operated calcium channels in cancer metastasis: from cell migration, invasion to metastatic colonization. *FBL* 23: 1241-1256

Morrish F, Hockenbery D (2014) MYC and mitochondrial biogenesis. *Cold Spring Harb Perspect Med* 4

Motiani RK, Abdullaev IF, Trebak M (2010) A novel native store-operated calcium channel encoded by Orai3: selective requirement of Orai3 versus Orai1 in estrogen receptor-positive versus estrogen receptor-negative breast cancer cells. *J Biol Chem* 285: 19173-19183

Motiani RK, Hyzinski-Garcia MC, Zhang X, Henkel MM, Abdullaev IF, Kuo YH, Matrougui K, Mongin AA, Trebak M (2013a) STIM1 and Orai1 mediate CRAC channel activity and are essential for human glioblastoma invasion. *Pflugers Arch* 465: 1249-1260

Motiani RK, Tanwar J, Raja DA, Vashisht A, Khanna S, Sharma S, Srivastava S, Sivasubbu S, Natarajan VT, Gokhale RS (2018) STIM1 activation of adenylyl cyclase 6 connects Ca(2+) and cAMP signaling during melanogenesis. *The EMBO journal* 37

Motiani RK, Zhang X, Harmon KE, Keller RS, Matrougui K, Bennett JA, Trebak M (2013b) Orai3 is an estrogen receptor alpha-regulated Ca(2)(+) channel that promotes tumorigenesis. *FASEB J* 27: 63-75

Moy RH, Nguyen A, Loo JM, Yamaguchi N, Kajba CM, Santhanam B, Ostendorf BN, Wu YG, Tavazoie S, Tavazoie SF (2022) Functional genetic screen identifies ITPR3/calcium/RELB axis as a driver of colorectal cancer metastatic liver colonization. *Dev Cell* 57: 1146-1159.e1147

Novakovic MM, Korshunov KS, Grant RA, Martin ME, Valencia HA, Budinger GRS, Radulovic J, Prakriya M (2023) Astrocyte reactivity and inflammation-induced depression-like behaviors are regulated by Orai1 calcium channels. *Nat Commun* 14: 5500

Pakos-Zebrucka K, Koryga I, Mnich K, Ljujic M, Samali A, Gorman AM (2016) The integrated stress response. *EMBO Rep* 17: 1374-1395

Papp B, Brouland JP, Arbabian A, Gélébart P, Kovács T, Bobe R, Enouf J, Varin-Blank N, Apáti A (2012) Endoplasmic reticulum calcium pumps and cancer cell differentiation. *Biomolecules* 2: 165-186

Pathak T, Gueguinou M, Walter V, Delierneux C, Johnson MT, Zhang X, Xin P, Yoast RE, Emrich SM, Yochum GS *et al* (2020) Dichotomous role of the human mitochondrial Na(+)/Ca2(+)/Li(+) exchanger NCLX in colorectal cancer growth and metastasis. *Elife* 9

Pathak T, Trebak M (2018) Mitochondrial Ca(2+) signaling. *Pharmacol Ther* 192: 112-123

Patra KC, Hay N (2014) The pentose phosphate pathway and cancer. *Trends Biochem Sci* 39: 347-354

Popay TM, Wang J, Adams CM, Howard GC, Codreanu SG, Sherrod SD, McLean JA, Thomas LR, Lorey SL, Machida YJ *et al* (2021) MYC regulates ribosome biogenesis and mitochondrial gene expression programs through its interaction with host cell factor–1. *eLife* 10: e60191

Prakriya M, Lewis RS (2015) Store-Operated Calcium Channels. *Physiol Rev* 95: 1383-1436

Preissler S, Rato C, Yan Y, Perera LA, Czako A, Ron D (2020) Calcium depletion challenges endoplasmic reticulum proteostasis by destabilising BiP-substrate complexes. *eLife* 9: e62601

Ritchie ME, Phipson B, Wu D, Hu Y, Law CW, Shi W, Smyth GK (2015) limma powers differential expression analyses for RNA-sequencing and microarray studies. *Nucleic Acids Res* 43: e47

Ritchie MF, Samakai E, Soboloff J (2012) STIM1 is required for attenuation of PMCA-mediated Ca2+ clearance during T-cell activation. *The EMBO journal* 31: 1123-1133

Roos J, DiGregorio PJ, Yeromin AV, Ohlsen K, Lioudyno M, Zhang SY, Safrina O, Kozak JA, Wagner SL, Cahalan MD *et al* (2005) STIM1, an essential and conserved component of store-operated Ca2+ channel function. *J Cell Biol* 169: 435-445

Satoh K, Yachida S, Sugimoto M, Oshima M, Nakagawa T, Akamoto S, Tabata S, Saitoh K, Kato K, Sato S *et al* (2017) Global metabolic reprogramming of colorectal cancer occurs at adenoma stage and is induced by MYC. *Proc Natl Acad Sci U S A* 114: E7697-E7706

Sears R, Nuckolls F, Haura E, Taya Y, Tamai K, Nevins JR (2000) Multiple Ras-dependent phosphorylation pathways regulate Myc protein stability. *Genes Dev* 14: 2501-2514

Shapovalov G, Gordienko D, Prevarskaya N (2021) Store operated calcium channels in cancer progression. *Int Rev Cell Mol Biol* 363: 123-168

Shinde AV, Motiani RK, Zhang X, Abdullaev IF, Adam AP, Gonzalez-Cobos JC, Zhang W, Matrougui K, Vincent PA, Trebak M (2013) STIM1 controls endothelial barrier function independently of Orai1 and Ca2+ entry. *Sci Signal* 6: ra18

Shuttleworth TJ, Thompson JL, Mignen O (2007) STIM1 and the noncapacitative ARC channels. *Cell Calcium* 42: 183-191

Siegel RL, Miller KD, Jemal A (2020) Cancer statistics, 2020. *CA: A Cancer Journal for Clinicians* 70: 7-30

Siegel RL, Wagle NS, Cercek A, Smith RA, Jemal A (2023) Colorectal cancer statistics, 2023. *CA: A Cancer Journal for Clinicians* 73: 233-254

Stadler M, Scherzer M, Walter S, Holzner S, Pudelko K, Riedl A, Unger C, Kramer N, Weil B, Neesen J *et al* (2018) Exclusion from spheroid formation identifies loss of essential cell-cell adhesion molecules in colon cancer cells. *Scientific Reports* 8: 1151

Stewart TA, Yapa KTDS, Monteith GR (2015) Altered calcium signaling in cancer cells. *Biochimica et Biophysica Acta (BBA) - Biomembranes* 1848: 2502-2511

Subramanian A, Tamayo P, Mootha VK, Mukherjee S, Ebert BL, Gillette MA, Paulovich A, Pomeroy SL, Golub TR, Lander ES *et al* (2005) Gene set enrichment analysis: a knowledge-based approach for interpreting genome-wide expression profiles. *Proc Natl Acad Sci U S A* 102: 15545-15550

Suzuki J, Kanemaru K, Ishii K, Ohkura M, Okubo Y, Iino M (2014) Imaging intraorganellar Ca2+ at subcellular resolution using CEPIA. *Nat Commun* 5: 4153

Tameire F, Verginadis, II, Leli NM, Polte C, Conn CS, Ojha R, Salas Salinas C, Chinga F, Monroy AM, Fu W *et al* (2019) ATF4 couples MYC-dependent translational activity to bioenergetic demands during tumour progression. *Nat Cell Biol* 21: 889-899

Teng S, Li YE, Yang M, Qi R, Huang Y, Wang Q, Zhang Y, Chen S, Li S, Lin K *et al* (2020) Tissue-specific transcription reprogramming promotes liver metastasis of colorectal cancer. *Cell Research* 30: 34-49

Trebak M, Kinet JP (2019) Calcium signalling in T cells. *Nat Rev Immunol* 19: 154-169

Trebak M, Putney JW, Jr. (2017) ORAI Calcium Channels. *Physiology (Bethesda)* 32: 332-342

Tsai WB, Aiba I, Long Y, Lin HK, Feun L, Savaraj N, Kuo MT (2012) Activation of Ras/PI3K/ERK pathway induces c-Myc stabilization to upregulate argininosuccinate synthetase, leading to arginine deiminase resistance in melanoma cells. *Cancer Res* 72: 2622-2633

Vaeth M, Maus M, Klein-Hessling S, Freinkman E, Yang J, Eckstein M, Cameron S, Turvey SE, Serfling E, Berberich-Siebelt F *et al* (2017) Store-Operated Ca(2+) Entry Controls Clonal Expansion of T Cells through Metabolic Reprogramming. *Immunity* 47: 664-679 e666

Vasan K, Werner M, Chandel NS (2020) Mitochondrial Metabolism as a Target for Cancer Therapy. *Cell Metabolism*

Vyas S, Zaganjor E, Haigis MC (2016) Mitochondria and Cancer. *Cell* 166: 555-566

Walter P, Ron D (2011) The Unfolded Protein Response: From Stress Pathway to Homeostatic Regulation. *Science* 334: 1081-1086

Wang JY, Sun J, Huang MY, Wang YS, Hou MF, Sun Y, He H, Krishna N, Chiu SJ, Lin S *et al* (2015) STIM1 overexpression promotes colorectal cancer progression, cell motility and COX-2 expression. *Oncogene* 34: 4358-4367

Wedel B, Boyles RR, Putney J, Bird GS (2007) Role of the store-operated calcium entry proteins Stim1 and Orai1 in muscarinic cholinergic receptor-stimulated calcium oscillations in human embryonic kidney cells. *J Physiol-London* 579: 679-689

Worley PF, Zeng W, Huang GN, Yuan JP, Kim JY, Lee MG, Muallem S (2007) TRPC channels as STIM1-regulated store-operated channels. *Cell Calcium* 42: 205-211

Xie J, Pan H, Yao J, Zhou Y, Han W (2016) SOCE and cancer: Recent progress and new perspectives. *Int J Cancer* 138: 2067-2077

Yang N, Tang Y, Wang F, Zhang H, Xu D, Shen Y, Sun S, Yang G (2013) Blockade of store-operated Ca(2+) entry inhibits hepatocarcinoma cell migration and invasion by regulating focal adhesion turnover. *Cancer Lett* 330: 163-169

Yang S, Zhang JJ, Huang X-Y (2009) Orai1 and STIM1 Are Critical for Breast Tumor Cell Migration and Metastasis. *Cancer Cell* 15: 124-134

Yeung PS, Yamashita M, Prakriya M (2020) Molecular basis of allosteric Orai1 channel activation by STIM1. *J Physiol* 598: 1707-1723

Yoast RE, Emrich SM, Trebak M (2020a) The anatomy of native CRAC channel(s). *Curr Opin Physiol* 17: 89-95

Yoast RE, Emrich SM, Zhang X, Xin P, Arige V, Pathak T, Benson JC, Johnson MT, Abdelnaby AE, Lakomski N *et al* (2021) The Mitochondrial Ca(2+) uniporter is a central regulator of interorganellar Ca(2+) transfer and NFAT activation. *J Biol Chem* 297: 101174

Yoast RE, Emrich SM, Zhang X, Xin P, Johnson MT, Fike AJ, Walter V, Hempel N, Yule DI, Sneyd J *et al* (2020b) The native ORAI channel trio underlies the diversity of Ca2+ signaling events. *Nature Communications* 11: 2444

Yoast RE, Emrich SM, Zhang X, Xin P, Johnson MT, Fike AJ, Walter V, Hempel N, Yule DI, Sneyd J *et al* (2020c) The native ORAI channel trio underlies the diversity of Ca(2+) signaling events. *Nat Commun* 11: 2444

Zhang X, Gonzalez-Cobos JC, Schindl R, Muik M, Ruhle B, Motiani RK, Bisaillon JM, Zhang W, Fahrner M, Barroso M *et al* (2013) Mechanisms of STIM1 activation of store-independent leukotriene C4-regulated Ca2+ channels. *Mol Cell Biol* 33: 3715-3723

Zhang Z, Liu X, Feng B, Liu N, Wu Q, Han Y, Nie Y, Wu K, Shi Y, Fan D (2015) STIM1, a direct target of microRNA-185, promotes tumor metastasis and is associated with poor prognosis in colorectal cancer. *Oncogene* 34: 4808-4820

Zhao G, Li T, Brochet DX, Rosenberg PB, Lederer WJ (2015) STIM1 enhances SR Ca2+ content through binding phospholamban in rat ventricular myocytes. *Proc Natl Acad Sci U S A* 112: E4792-4801

Zheng S, Wang X, Zhao D, Liu H, Hu Y (2022) Calcium homeostasis and cancer: insights from endoplasmic reticulum-centered organelle communications. *Trends in Cell Biology*

Figure 1

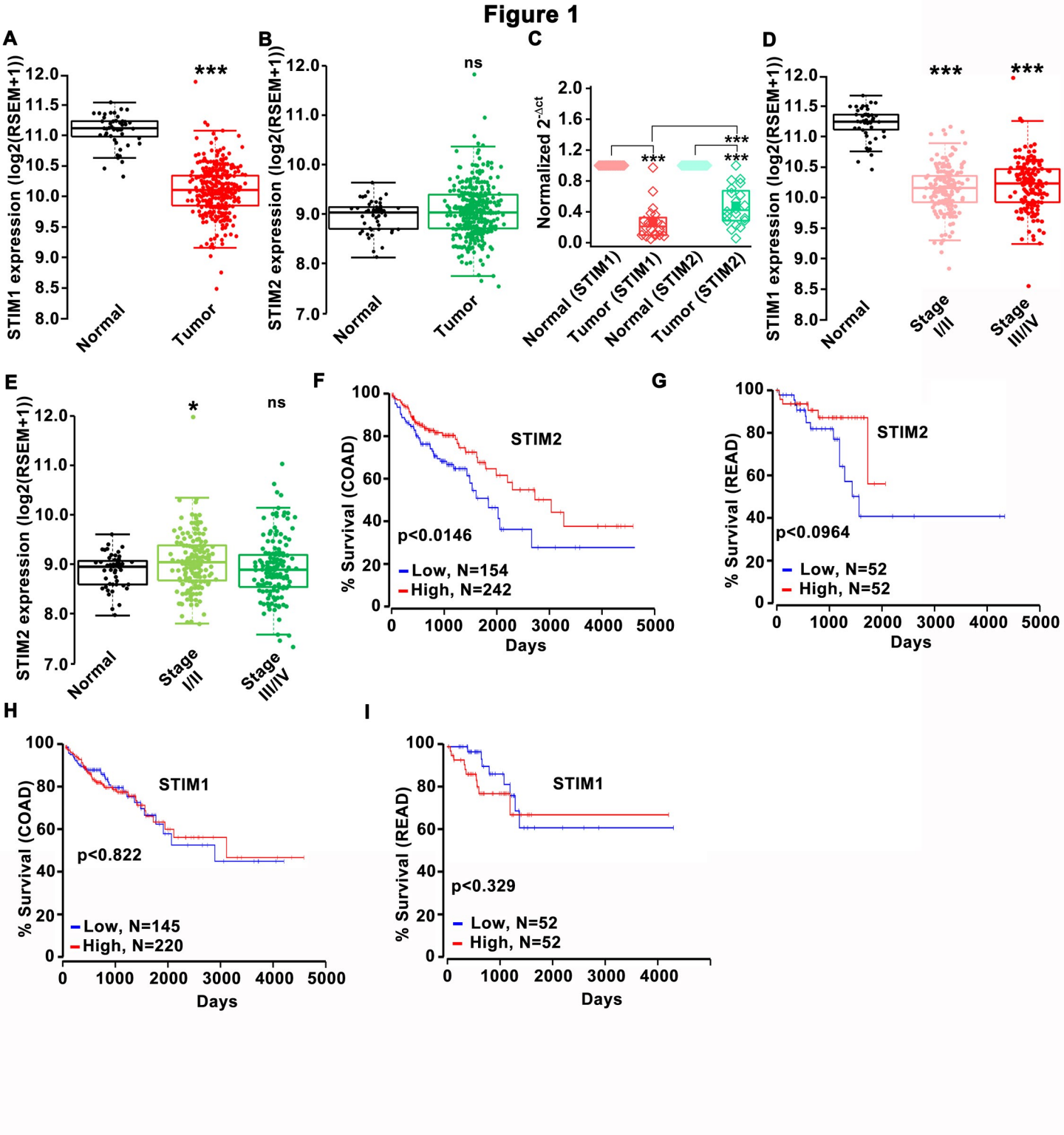
A
STIM1 expression (log2(RSEM+1))
***
Normal
Tumor
B
STIM2 expression (log2(RSEM+1))
ns
Normal
Tumor
C
Normalized 2^-Δct
***
***
***
Normal (STIM1)
Tumor (STIM1)
Normal (STIM2)
Tumor (STIM2)
D
STIM1 expression (log2(RSEM+1))
***
***
Normal
Stage I/II
Stage III/IV
E
STIM2 expression (log2(RSEM+1))
*
ns
Normal
Stage I/II
Stage III/IV
F
% Survival (COAD)
STIM2
p<0.0146
Low, N=154
High, N=242
Days
G
% Survival (READ)
STIM2
p<0.0964
Low, N=52
High, N=52
Days
H
% Survival (COAD)
STIM1
p<0.822
Low, N=145
High, N=220
Days
I
% Survival (READ)
STIM1
p<0.329
Low, N=52
High, N=52
Days

Figure 2

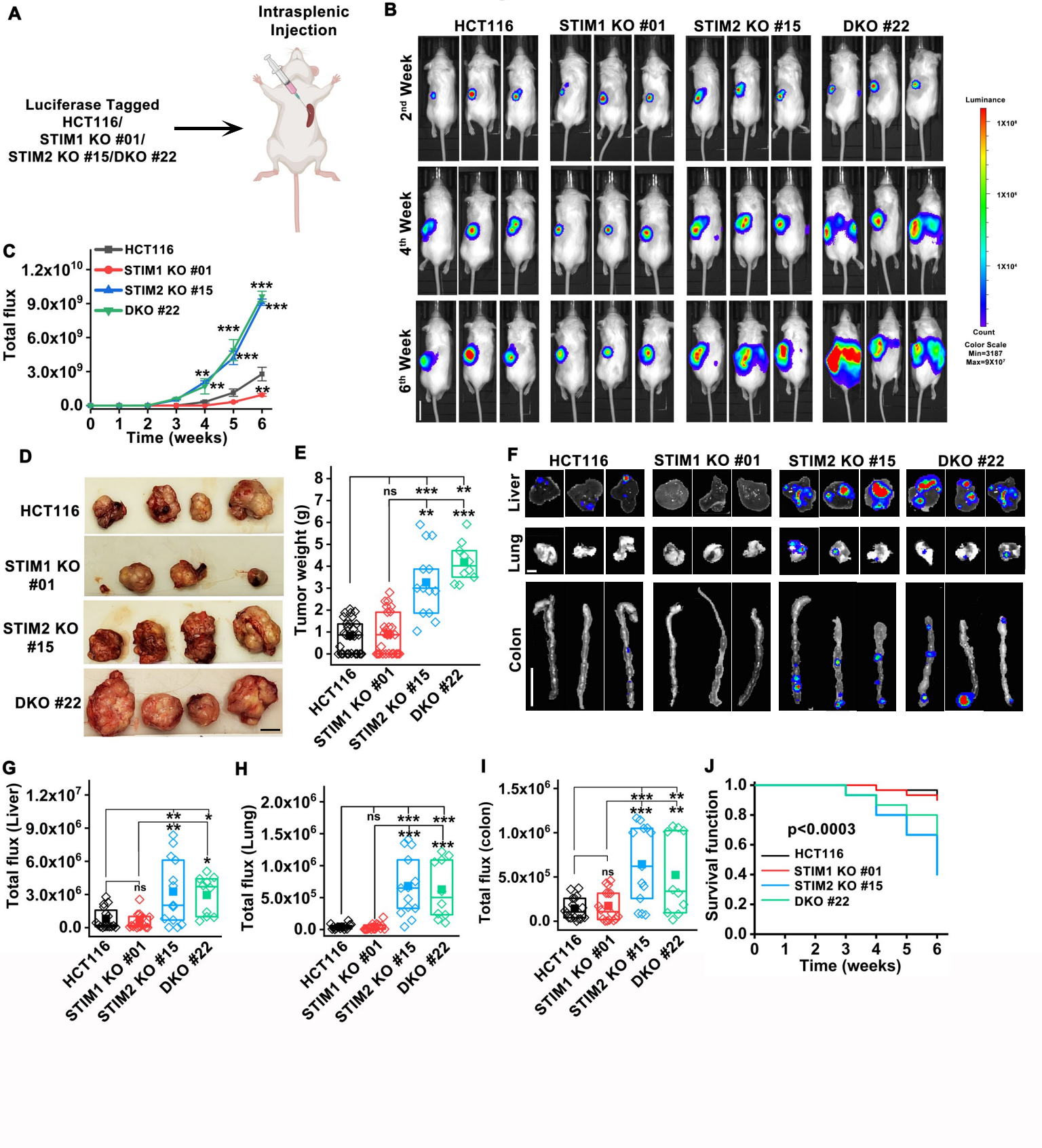
A
Intrasplenic Injection
Luciferase Tagged HCT116/ STIM1 KO #01/ STIM2 KO #15/DKO #22
B
HCT116
STIM1 KO #01
STIM2 KO #15
DKO #22
2nd Week
4th Week
6th Week
Luminance
1X10⁶
1X10⁵
1X10⁴
Count
Color Scale Min=3187 Max=9X10⁷
C
HCT116
STIM1 KO #01
STIM2 KO #15
DKO #22
Total flux
1.2x10¹⁰
9.0x10⁹
6.0x10⁹
3.0x10⁹
0.0
0 1 2 3 4 5 6
Time (weeks)
D
HCT116
STIM1 KO #01
STIM2 KO #15
DKO #22
E
Tumor weight (g)
ns
HCT116
STIM1 KO #01
STIM2 KO #15
DKO #22
F
HCT116
STIM1 KO #01
STIM2 KO #15
DKO #22
Liver
Lung
Colon
G
Total flux (Liver)
1.2x10⁷
9.0x10⁶
6.0x10⁶
3.0x10⁶
0.0
ns
HCT116
STIM1 KO #01
STIM2 KO #15
DKO #22
H
Total flux (Lung)
2.0x10⁶
1.5x10⁶
1.0x10⁶
5.0x10⁵
0.0
ns
HCT116
STIM1 KO #01
STIM2 KO #15
DKO #22
I
Total flux (colon)
1.5x10⁶
1.0x10⁶
5.0x10⁵
0.0
ns
HCT116
STIM1 KO #01
STIM2 KO #15
DKO #22
J
Survival function
1.0
0.8
0.6
0.4
0.2
0.0
p<0.0003
HCT116
STIM1 KO #01
STIM2 KO #15
DKO #22
0 1 2 3 4 5 6
Time (weeks)

Figure 3

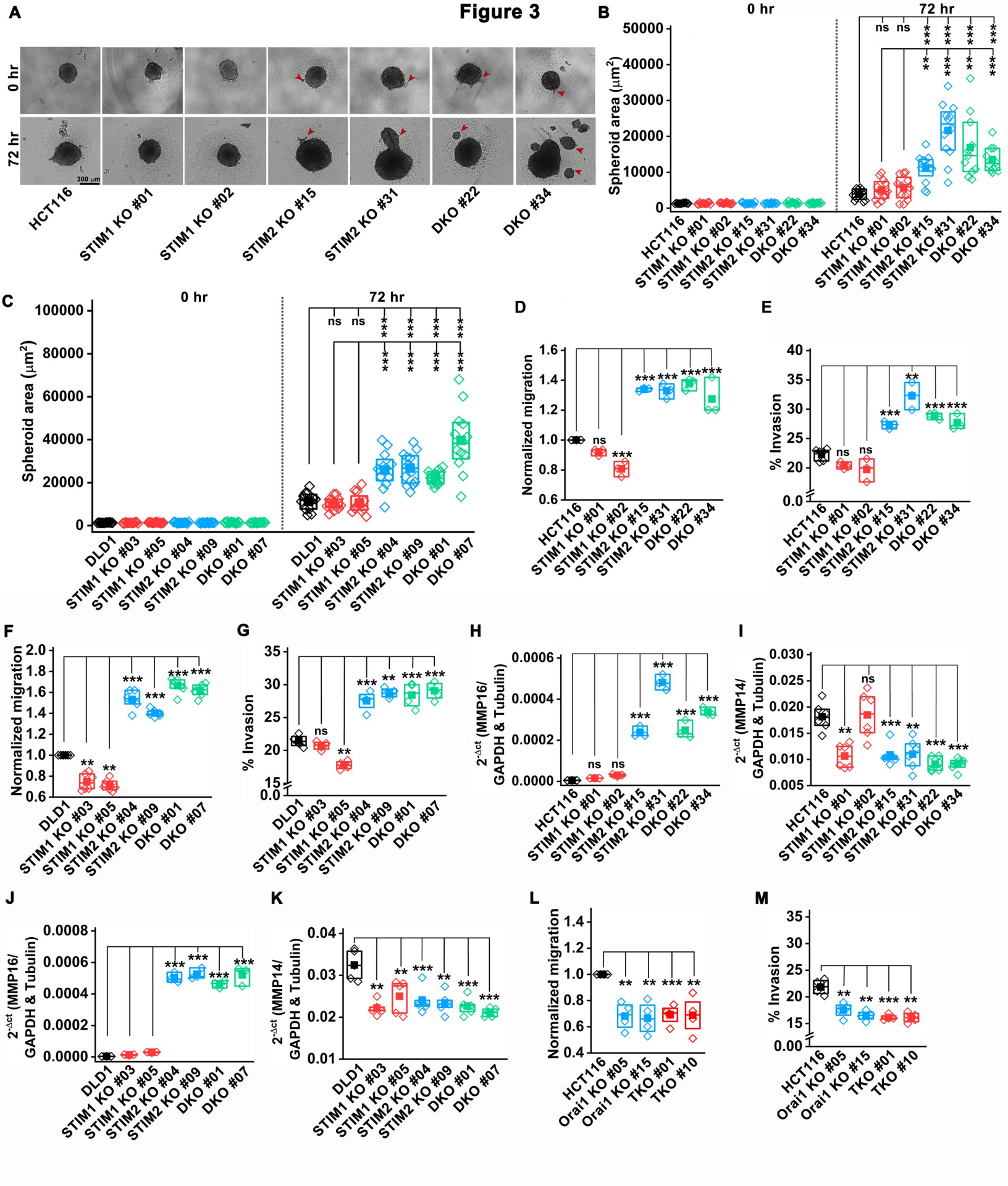
A
0 hr
72 hr
300 μm
HCT116
STIM1 KO #01
STIM1 KO #02
STIM2 KO #15
STIM2 KO #31
DKO #22
DKO #34
B
0 hr
72 hr
Spheroid area (μm²)
ns
C
Spheroid area (μm²)
DLD1
STIM1 KO #03
STIM1 KO #05
STIM2 KO #04
STIM2 KO #09
DKO #01
DKO #07
D
Normalized migration
E
% Invasion
F
Normalized migration
G
% Invasion
H
2^-Δct (MMP16/ GAPDH & Tubulin)
I
2^-Δct (MMP14/ GAPDH & Tubulin)
J
2^-Δct (MMP16/ GAPDH & Tubulin)
K
2^-Δct (MMP14/ GAPDH & Tubulin)
L
Normalized migration
Orai1 KO #05
Orai1 KO #15
TKO #01
TKO #10
M
% Invasion

Figure 4

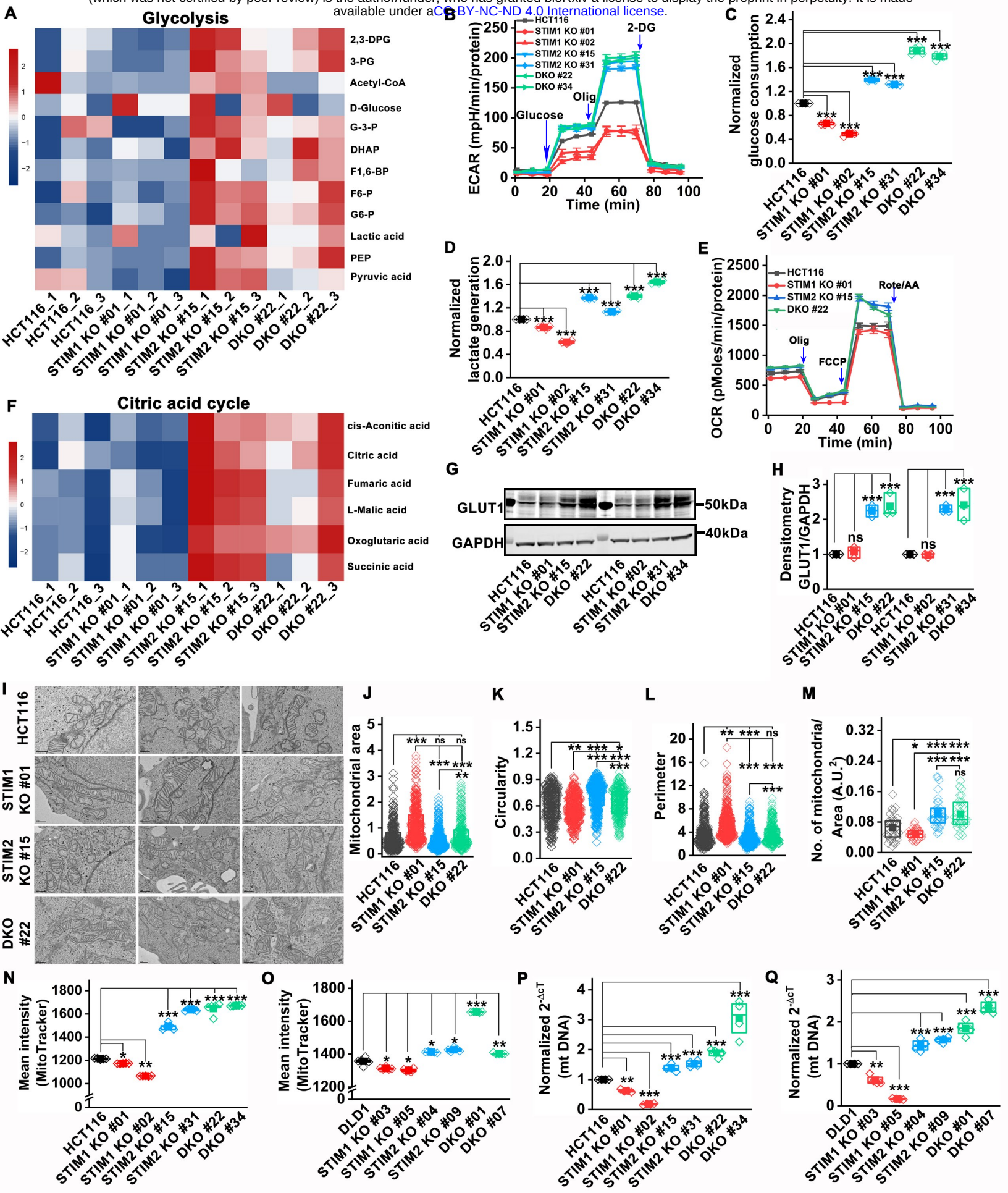

Figure 5

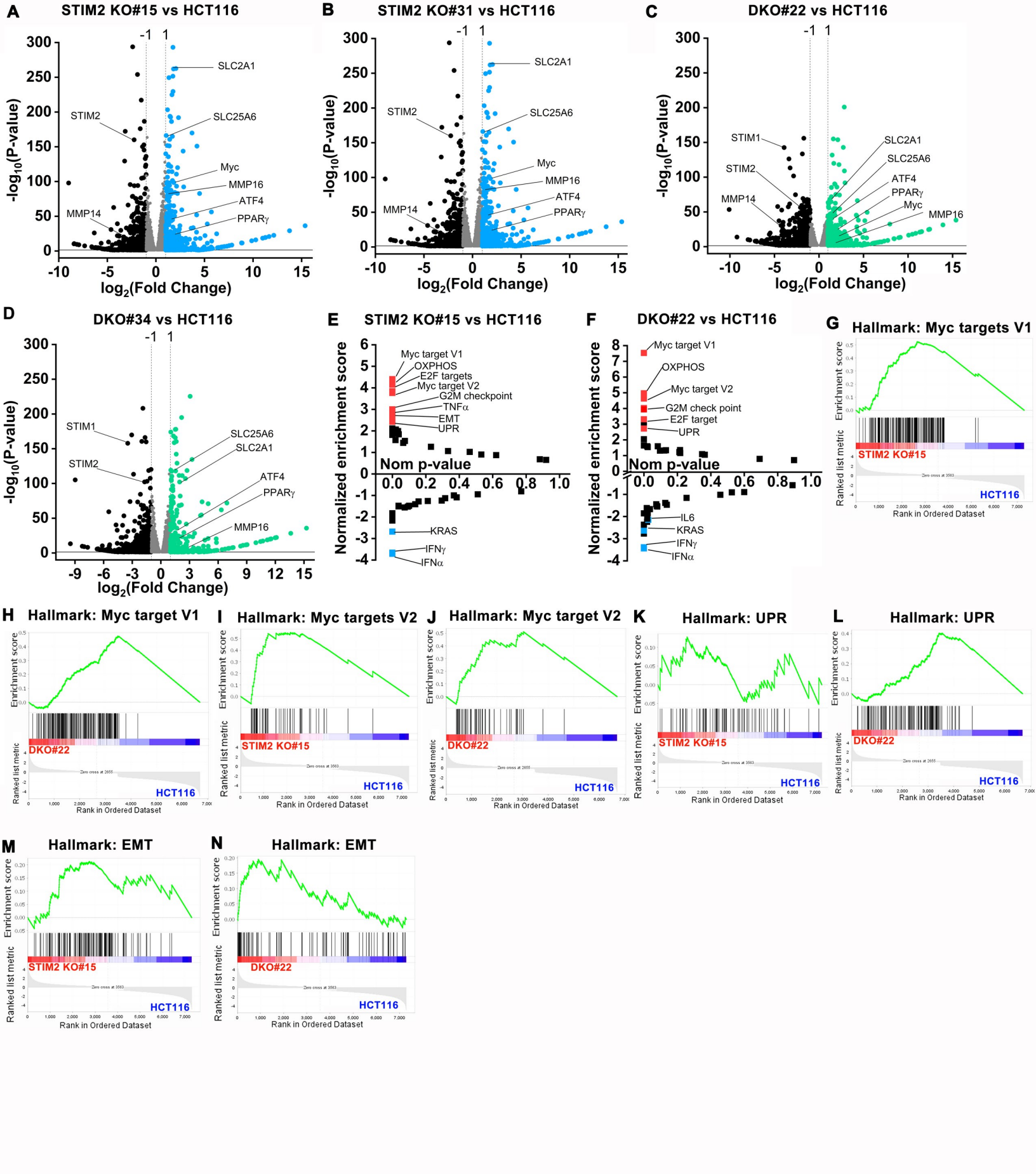
A
STIM2 KO#15 vs HCT116
B
STIM2 KO#31 vs HCT116
C
DKO#22 vs HCT116
D
DKO#34 vs HCT116
E
STIM2 KO#15 vs HCT116
F
DKO#22 vs HCT116
G
Hallmark: Myc targets V1
H
Hallmark: Myc target V1
I
Hallmark: Myc targets V2
J
Hallmark: Myc target V2
K
Hallmark: UPR
L
Hallmark: UPR
M
Hallmark: EMT
N
Hallmark: EMT
-log10(P-value)
log2(Fold Change)
Normalized enrichment score
Nom p-value
Enrichment score
Ranked list metric
Rank in Ordered Dataset
SLC2A1
SLC25A6
STIM2
STIM1
Myc
MMP16
ATF4
PPARγ
MMP14
Myc target V1
OXPHOS
E2F targets
Myc target V2
G2M checkpoint
TNFα
EMT
UPR
KRAS
IFNγ
IFNα
IL6
G2M check point
E2F target
STIM2 KO#15
DKO#22
HCT116

Figure 6

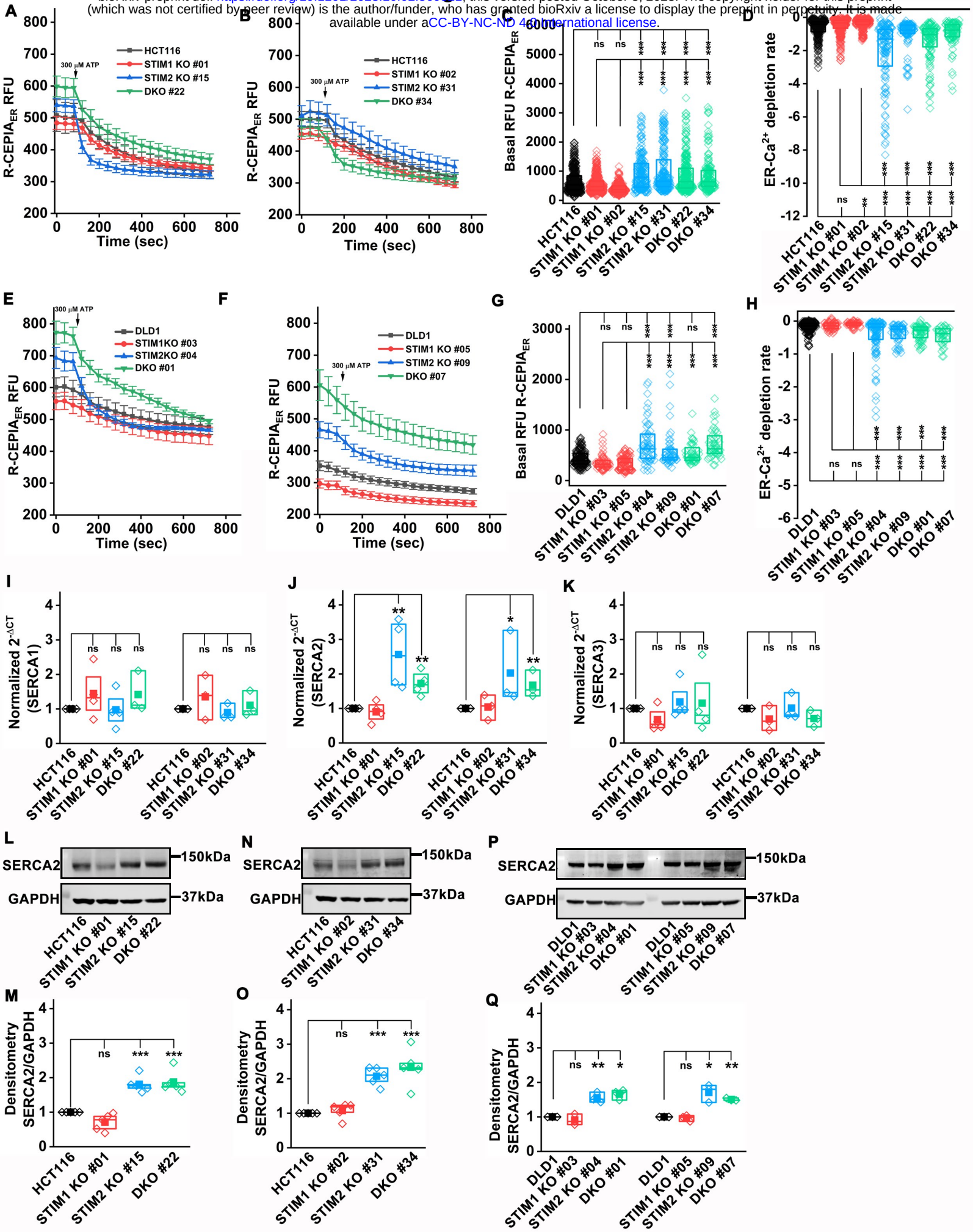

Figure 7

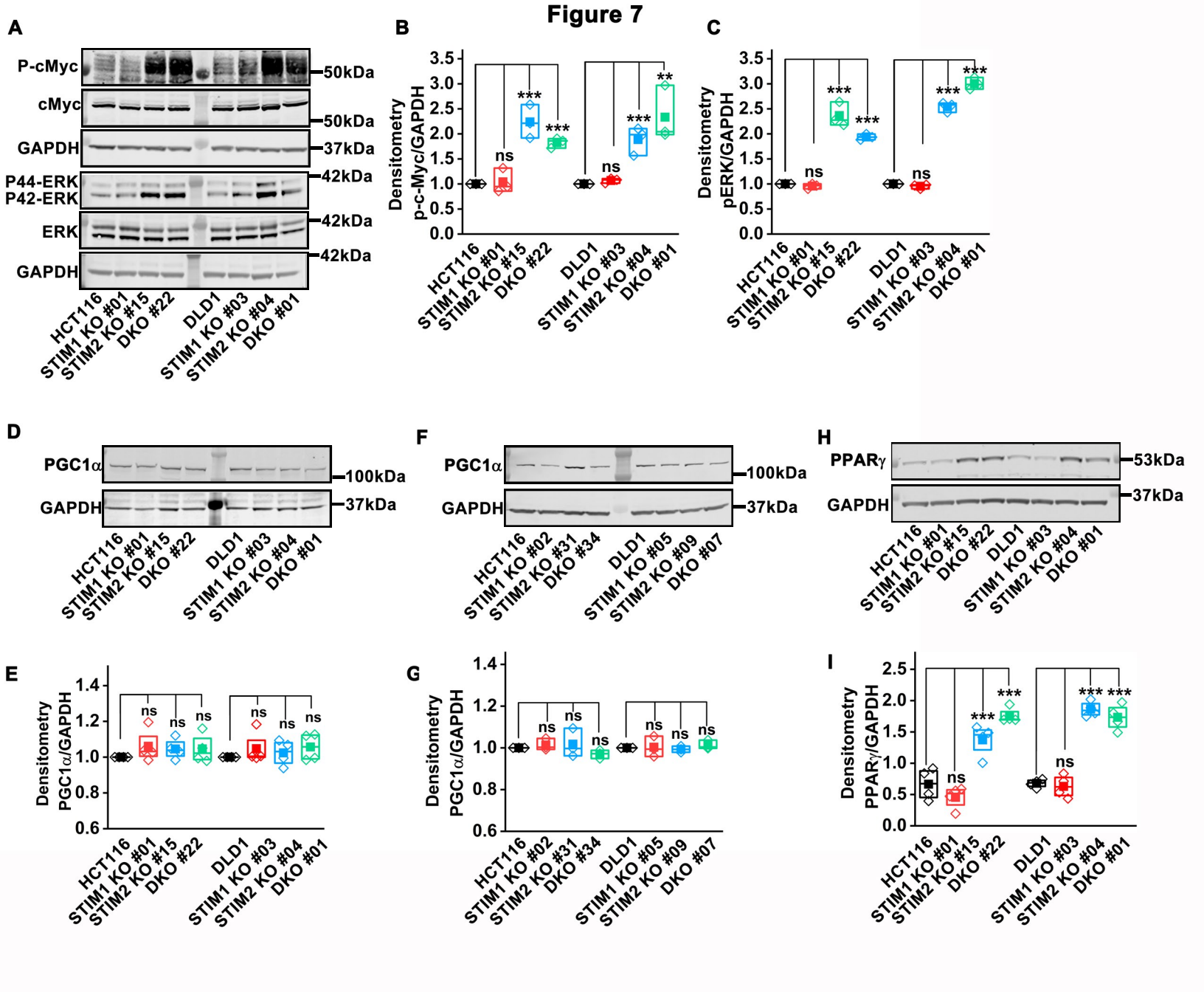
A
P-cMyc
cMyc
GAPDH
P44-ERK
P42-ERK
ERK
GAPDH
50kDa
50kDa
37kDa
42kDa
42kDa
42kDa
HCT116
STIM1 KO #01
STIM2 KO #15
DKO #22
DLD1
STIM1 KO #03
STIM2 KO #04
DKO #01
B
Densitometry
p-c-Myc/GAPDH
C
Densitometry
pERK/GAPDH
ns
***
**
D
PGC1α
GAPDH
100kDa
37kDa
F
PGC1α
GAPDH
100kDa
37kDa
HCT116
STIM1 KO #02
STIM2 KO #31
DKO #34
DLD1
STIM1 KO #05
STIM2 KO #09
DKO #07
H
PPARγ
GAPDH
53kDa
37kDa
E
Densitometry
PGC1α/GAPDH
G
Densitometry
PGC1α/GAPDH
I
Densitometry
PPARγ/GAPDH

Figure 8

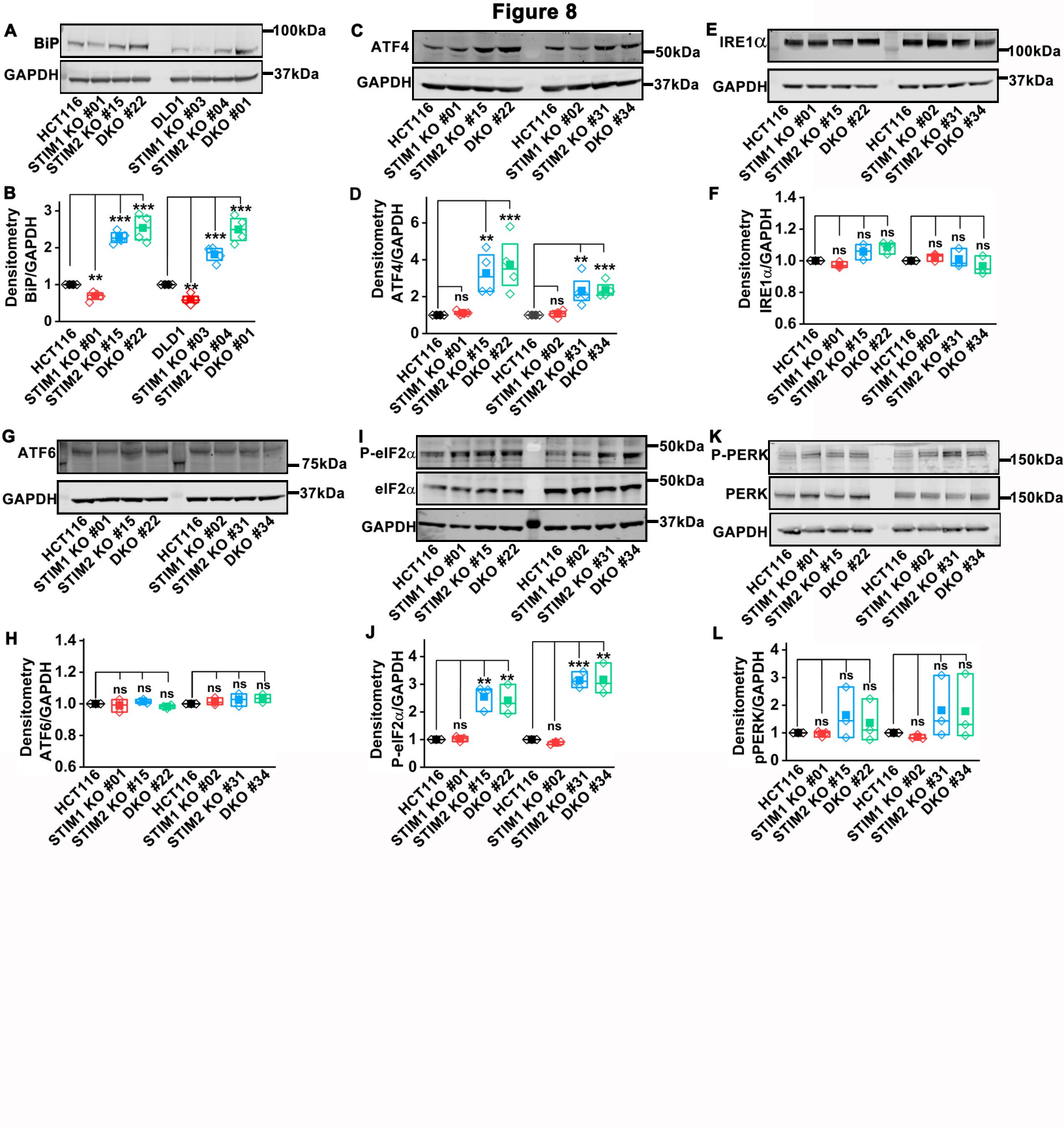
A
BiP
GAPDH
100kDa
37kDa
HCT116
STIM1 KO #01
STIM2 KO #15
DKO #22
DLD1
STIM1 KO #03
STIM2 KO #04
DKO #01
B
Densitometry BiP/GAPDH
C
ATF4
50kDa
STIM1 KO #02
STIM2 KO #31
DKO #34
D
Densitometry ATF4/GAPDH
E
IRE1α
F
Densitometry IRE1α/GAPDH
G
ATF6
75kDa
H
Densitometry ATF6/GAPDH
I
P-eIF2α
eIF2α
J
Densitometry P-eIF2α/GAPDH
K
P-PERK
PERK
150kDa
L
Densitometry pPERK/GAPDH
ns

Supplementary Figure 1

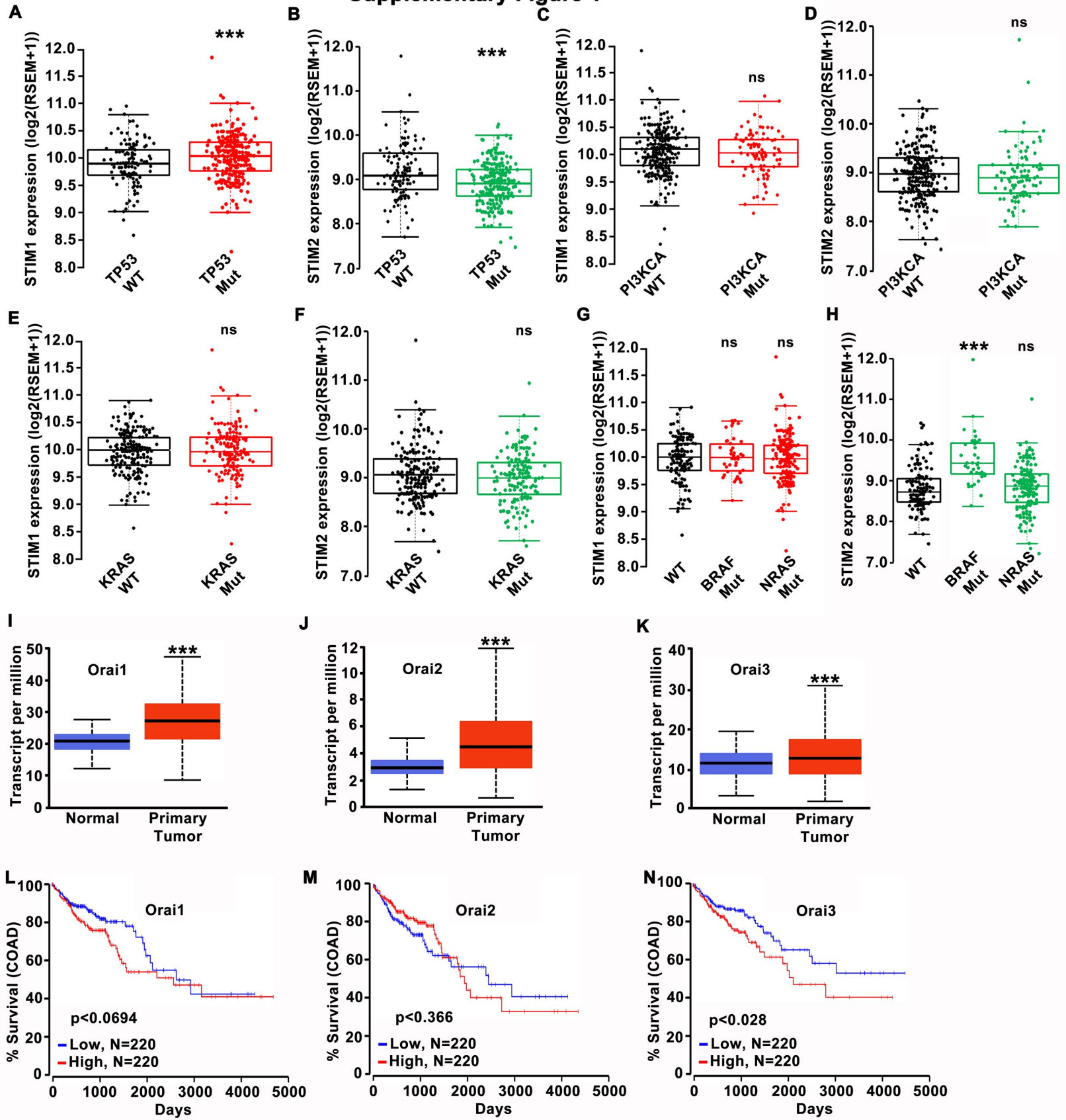

Supplementary Figure 2

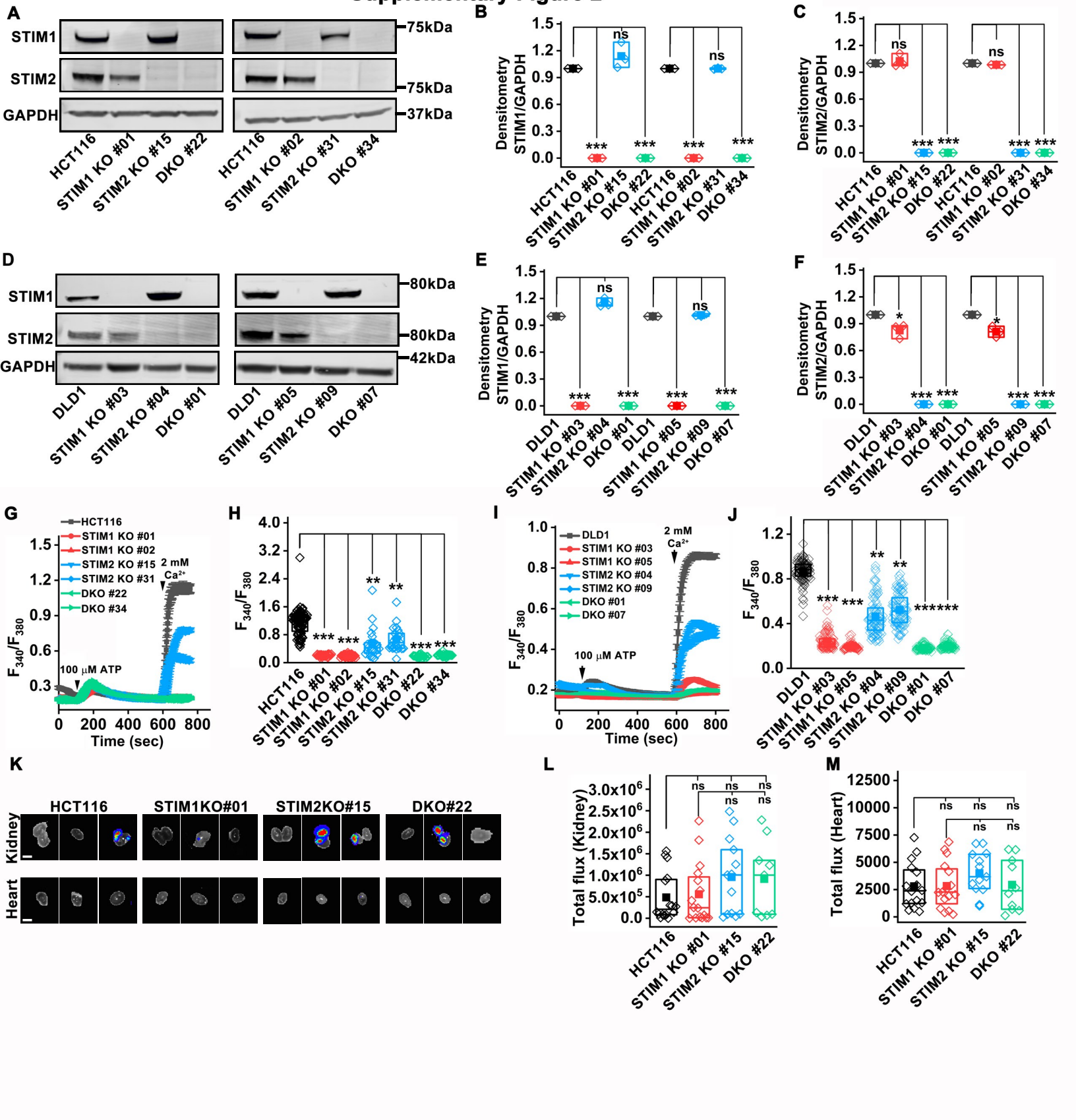

Supplementary Figure 3

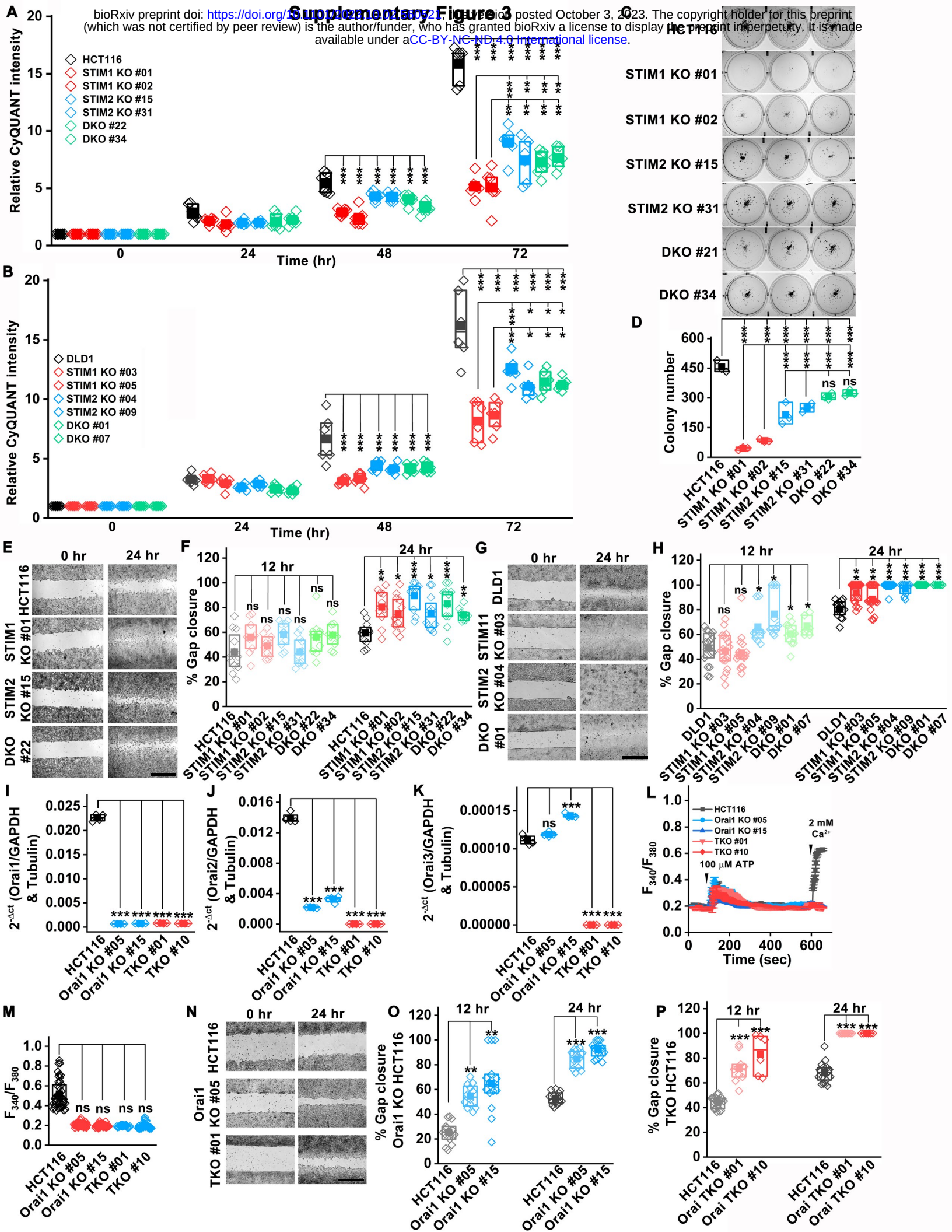

Supplementary Figure 4

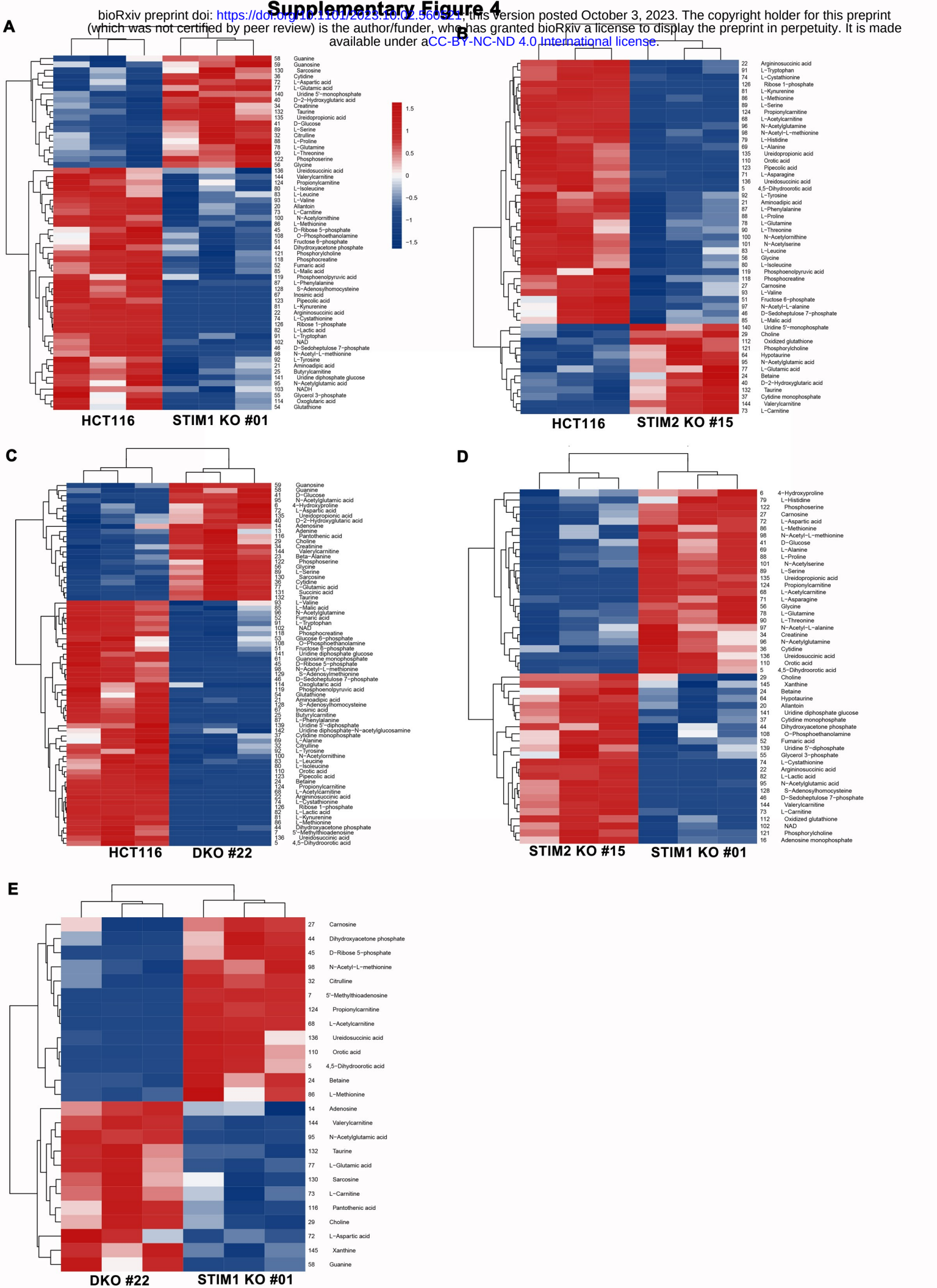

Supplementary Figure 5

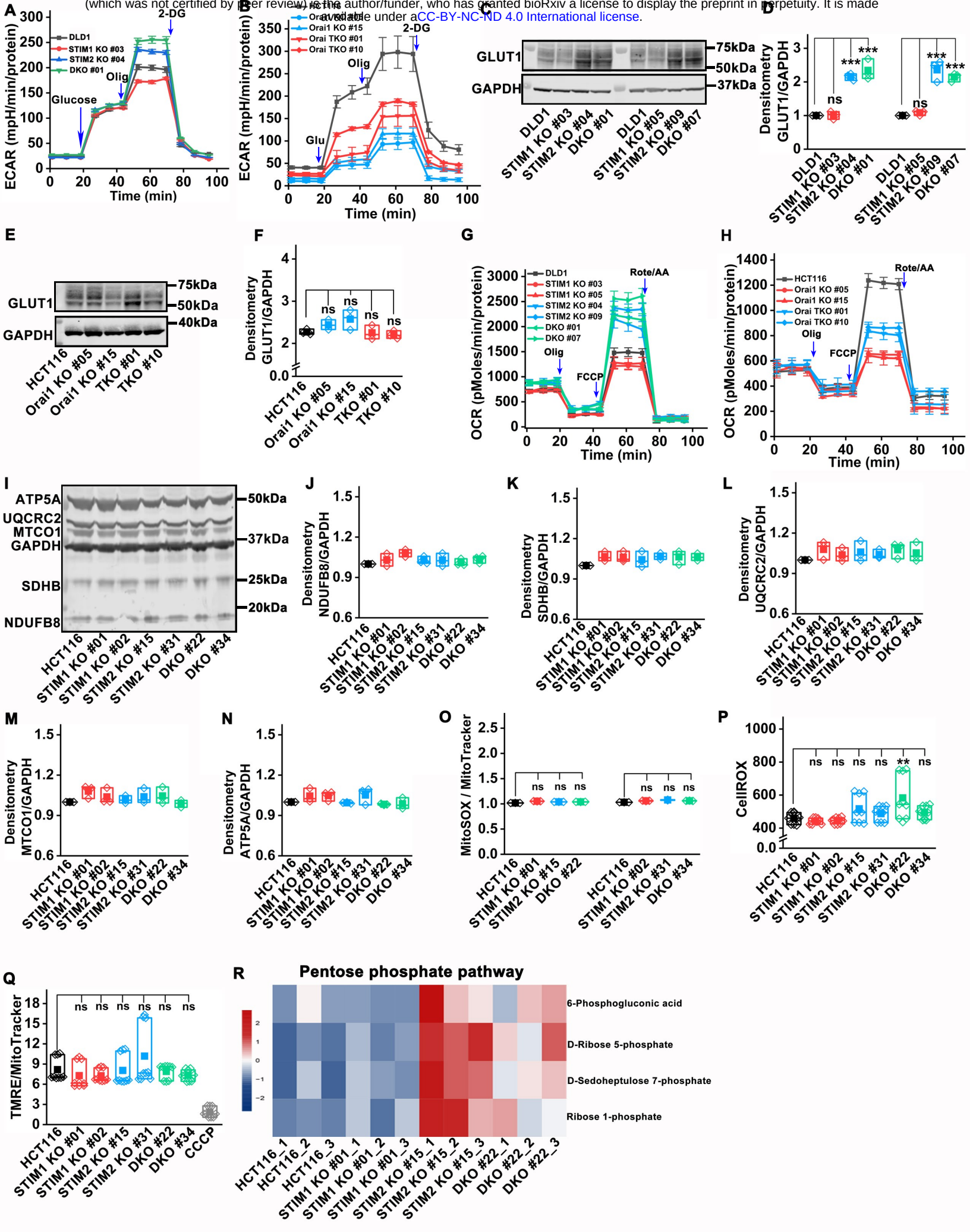

Supplementary Figure 6

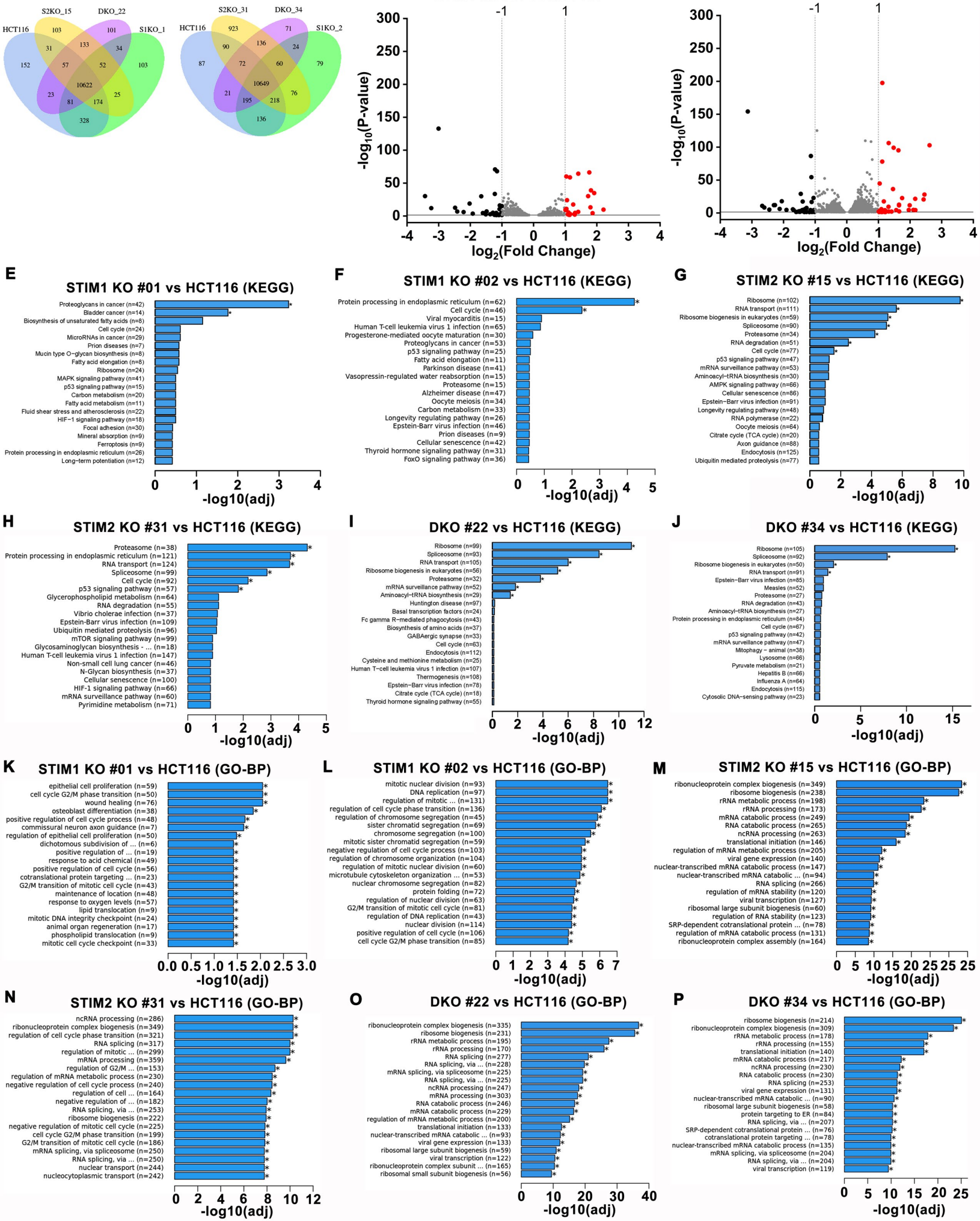

Supplementary Figure 7

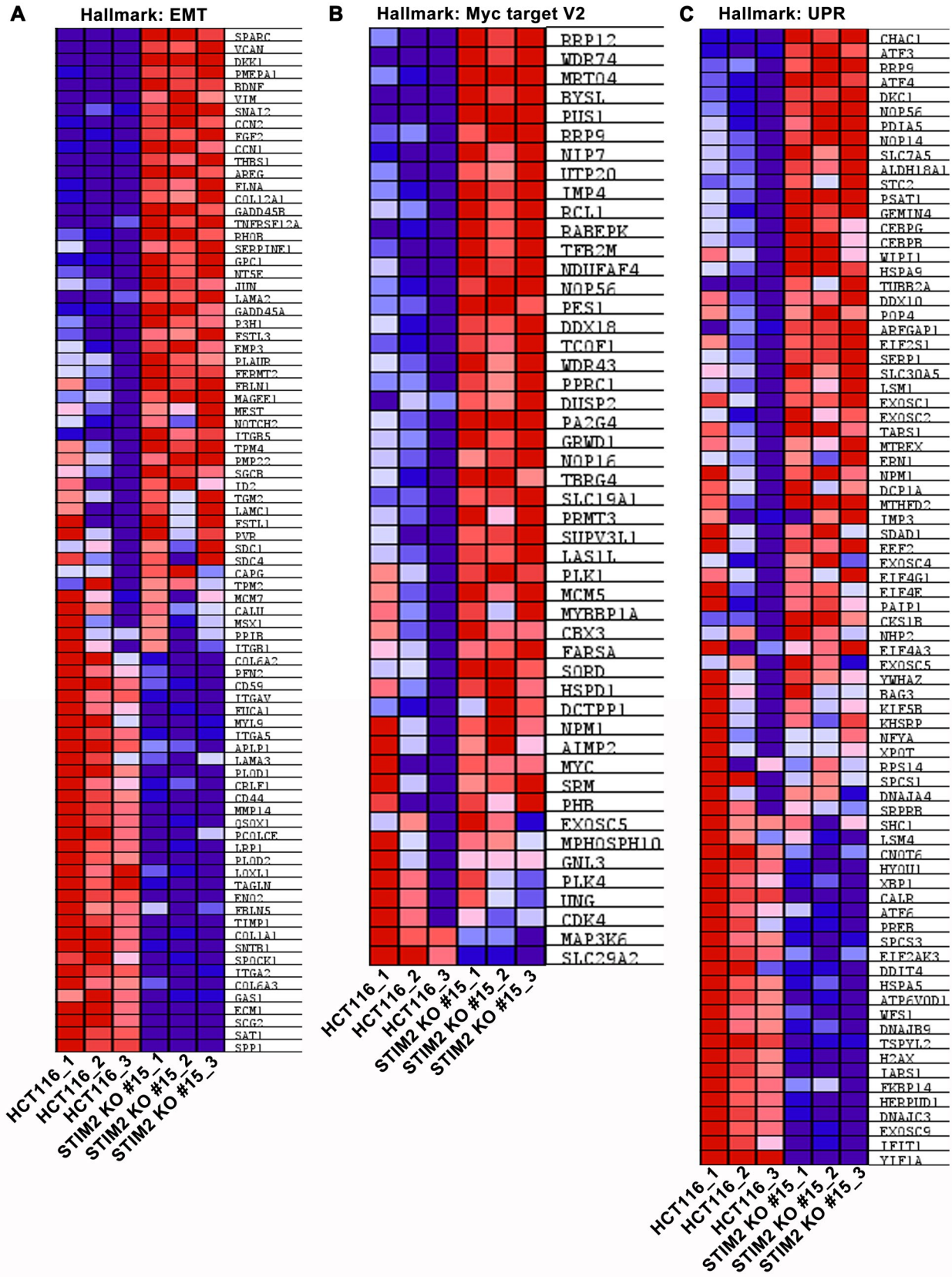

Supplementary Figure 8

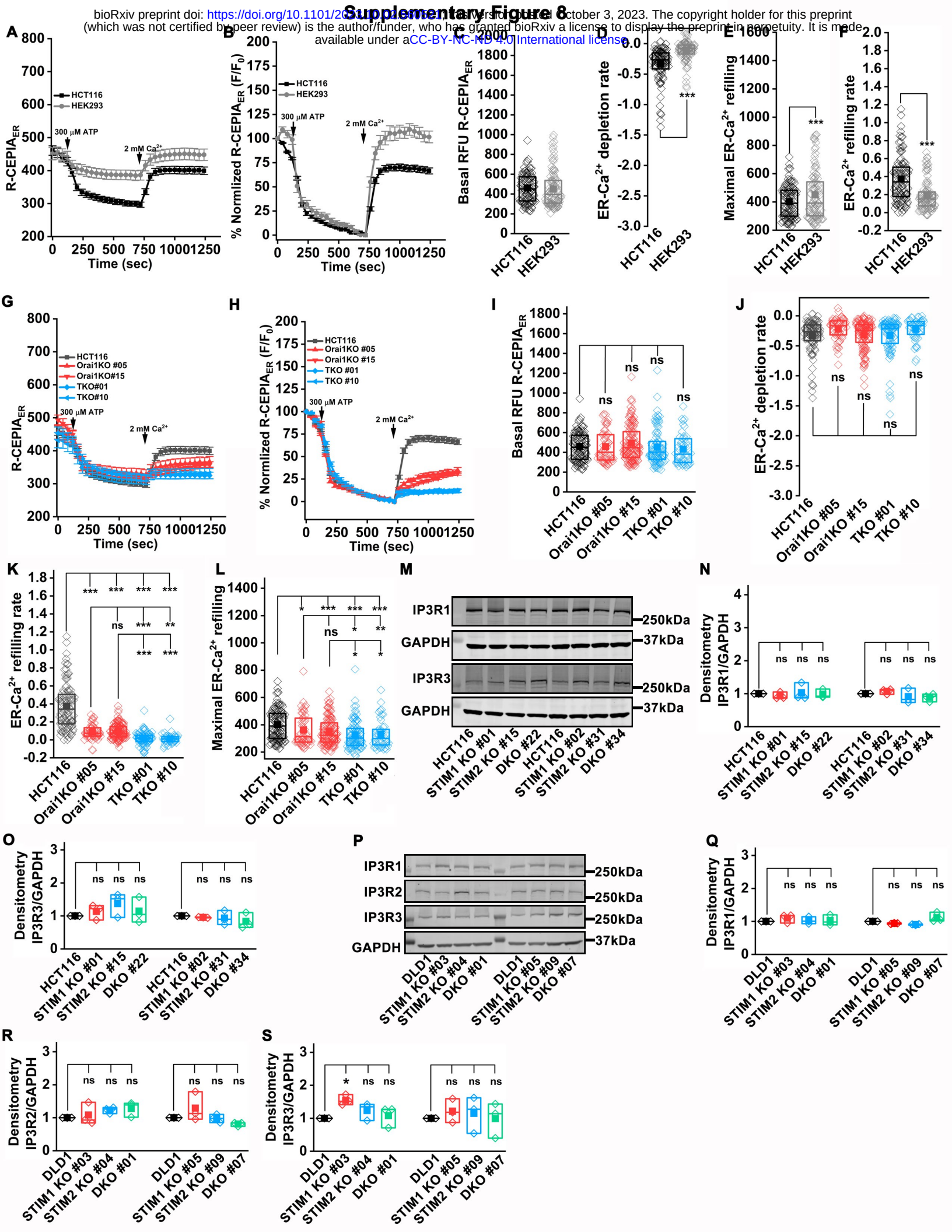

Supplementary Figure 9

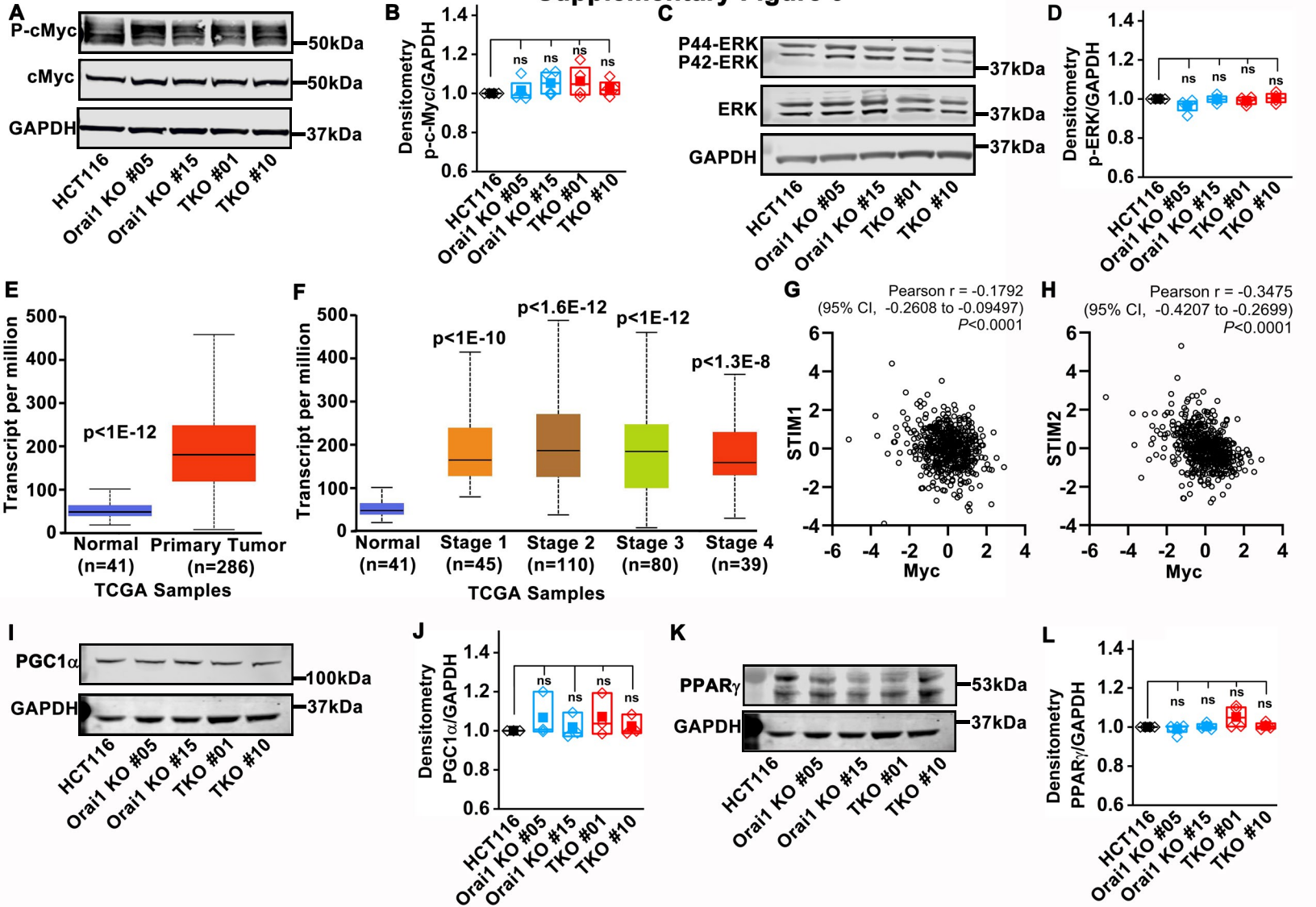

Supplementary Figure 10